

UNIVERSITY OF CALIFORNIA,
IRVINE

Effect of Environmental Conditions on Composition and Photochemistry of Secondary
Organic Aerosols

DISSERTATION

submitted in partial satisfaction of the requirements
for the degree of

DOCTOR OF PHILOSOPHY

in Chemistry

by

Mallory Lynn Hinks

Dissertation Committee:
Professor Sergey Nizkorodov, Chair
Professor Barbara Finlayson-Pitts
Assistant Professor Craig Murray

2017

DEDICATION

To my little sister, Katie. For always being my best friend.

TABLE OF CONTENTS

	Page
LIST OF FIGURES	vi
LIST OF TABLES	xi
ACKNOWLEDGMENTS	xii
CURRICULUM VITAE	xv
ABSTRACT OF THE DISSERTATION	xvii
Chapter 1	1
INTRODUCTION.....	1
1.1: General Background on Atmospheric Aerosols	2
1.2: Atmospheric Aging of SOA	5
1.3: Effects of Aerosol Phase	7
1.4: Effects of Water on SOA	9
1.5: Effects of Ammonia on SOA	10
Chapter 2.....	13
EFFECT OF VISCOSITY ON PHOTODEGRADATION RATES INSIDE COMPLEX SECONDARY ORGANIC AEROSOL MATERIAL	13
2.1: Introduction	14
2.2: Experimental	18
2.3: Results and Discussion	27
2.4: Conclusions	38
Chapter 3.....	40
EFFECT OF SOA COMPOSITION ON VISCOSITY AND PHOTOCHEMISTRY	40
3.1: Introduction	41
3.2: Aerosol Generation – MAGIC	42
3.3: Experimental	49
3.4: Results and Discussion	52
3.5: Conclusions and Future Work	54
Chapter 4.....	56
EFFECT OF RELATIVE HUMIDITY ON THE FORMATION AND COMPOSITION OF TOLUENE SOA	56
4.1: Introduction	57
4.2: Experimental	62

4.3: Results and Discussion	64
4.4: Conclusions	77
Chapter 5	79
CHEMICAL UPTAKE OF AMMONIA BY SOA PARTICLES	79
5.1: Introduction	80
5.2: Experimental	83
5.3: Results and Discussion	87
5.4: Conclusions	96
Chapter 6	99
SUMMARY	99
APPENDIX	102
References	119

LIST OF FIGURES

	Page
Figure 1.1. Structures of common biogenic and anthropogenic VOCs.	5
Figure 2.1. Diagram of the flow tube.....	19
Figure 2.2. SOA after impaction of A) α -pinene SOA and B) limonene SOA made in the aerosol flow tube.....	20
Figure 2.3. Photos of α -pinene SOM made in the flow tube. A) Fresh SOM collected in an X pattern. B) Sandwich technique for making SOM films. C) The bubbles produced within the film during long experiments between two (damaged) CaF ₂ windows.	21
Figure 2.4. A) Freshly collected limonene SOM from the flow tube and B) open-faced sandwich film of limonene SOM embedded with 2,4-DNP.	21
Figure 2.5. A) Freshly collected limonene SOM from the flow tube and B) limonene SOM after exposure to NH ₃ and drying (“Brown” limonene SOM)	22
Figure 2.6. A schematic diagram of the SSSS used to irradiate each sample at a range of RHs and temperatures.	23
Figure 2.7. Optical microscope images of an SOM particle A) before poking, B) immediately after being poked, and C) after recovering ½ of the initial hole diameter.	25
Figure 2.8. Representative absorption spectra recorded during the photodegradation of A) 2,4-DNP in LSOM and B) brown LSOM. The insets show the decay of A) the 290 nm peak of 2,4-DNP and B) the 510 nm peak characteristic of the brown LSOM chromophore where the red trace is the experimental decay and the black trace is the fit to Equation 2.2. The arrows indicate the wavelength at which spectra were fit to Equation 2.2 to get the rate constants.	29
Figure 2.9. Products tentatively identified by LC-PDA-MS after 2,4-DNP photolysis in isopropanol. Details leading to the assignments are provided in the supporting information section.	31
Figure 2.10. Arrhenius plots of the photodegradation rate of 2,4-DNP in PSOM (red), 2,4-DNP in LSOM (blue), and brown LSOM (green) under dry conditions. The slopes correspond to activation energies of 48, 24, and 16 kJ/mol, respectively. Markers with no error bars represent experiments that were performed once. All other markers are the average of 2-6 data points obtained at each temperature.	32
Figure 2.11. A) Average experimental flow time from the poke-flow experiments as a function of relative humidity. The markers correspond to the average of 4-11 individual poke flow measurements. The error bars represent one standard deviation for the repeated measurements. B) Simulated ranges of viscosities as determined by upper and lower limits.	

The error bars are dominated by uncertainties in the fitting parameters listed in Table 2.1. 33

Figure 2.12. A) The rate constants as a function of relative humidity for the photodegradation of 2,4-DNP in PSOM 2,4-DNP in LSOM, and brown LSOM. Each marker with error bars represents the average of all the data points at each RH. These experiments were repeated 2-6 times. The slopes of the fit were $(4.7 \pm 0.1) \times 10^{-6}$, $(2.9 \pm 0.9) \times 10^{-6}$, and $(8 \pm 2) \times 10^{-6} \text{ s}^{-1}/\%RH$ for 2,4-DNP in PSOM 2,4-DNP in LSOM, and brown LSOM respectively. Plot B) demonstrates the effect of drying speed..... 35

Figure 3.1. Diagram of MAGIC. 43

Figure 3.2. Emission spectrum of MAGIC’s UV lamps. 45

Figure 3.3. Abundance of fragments at m/z 44 as a function of abundance of fragments at m/z 43 (so called “triangular plot”) for benzene, toluene, and p-xylene SOA made by MAGIC. AMS measurements from both batch 1 and batch 2 conditions are shown. The darker colored dots for toluene and p-xylene refer to batch 2..... 46

Figure 3.4. A) FT-ICR-MS spectra and B) van Krevelen diagram for benzene SOA (top), toluene SOA (middle) and p-xylene SOA (bottom). Red indicates peaks that were unique to the sample..... 48

Figure 3.5. SOM after impaction of a) 100% toluene/0% limonene SOA, b) 80% toluene/20% limonene SOA, c) 50% toluene/50% limonene SOA, d) 20% toluene/80% limonene SOA, and e) 0% toluene/100% limonene SOA. 50

Figure 3.6. Absorption spectra of toluene SOM as a function of irradiation time 51

Figure 3.7. Calculated effective rate constants for each sample. 52

Figure 4.1. Examples of particle mass concentration measurements by SMPS (corrected for wall-loss) as a function of photooxidation time under low-NO_x (top) and high-NO_x (bottom) conditions. 66

Figure 4.2. Y_{RH}/Y_{dry} for the Low NO_x – high toluene system and the high NO_x – high toluene system. Error bars for each data point reflect the standard deviation of the low NO_x – high toluene system at 0% RH..... 68

Figure 4.3. High-resolution mass spectra obtained in negative ion mode (top) and positive ion mode (bottom). The red upward-pointing mass spectra represent the samples made under low RH (LN-HT-0712) and the blue inverted mass spectra represent the samples made under high RH (LN-HT-0711)..... 71

Figure 4.4. Combined abundance of all peaks as a function of number of carbon atoms in negative mode (top) and positive mode (bottom). The data for the low RH sample (LN-HT-

0712) are shown in red and the data for the high RH sample (LN-HT-0711) are shown in blue. 73

Figure 4.5. Estimated volatility distribution for the compounds observed in the positive (a) and negative (b) ion mode at high (red bars) and low (blue bars) RH. The height of each bar is proportional to the total ESI abundance of compounds falling within the volatility bin.. 75

Figure 5.1. Mechanism of formation of nitrogen-containing organic compounds. 81

Figure 5.2. Diagram of the Nizkorodov Lab Smog Chamber. The inlet flows are not continuous but rather applied for a short period of time to inject a given reactant. 84

Figure 5.3. SMPS data for A) toluene/OH (black) SOA low NO_x B) n-hexadecane/OH (blue) SOA low NO_x C) limonene/OH SOA (red) low NO_x D) toluene/OH (black) SOA high NO_x E) n-hexadecane/OH (blue) SOA high NO_x F) limonene/OH SOA (red) high NO_x. The yellow section indicates the time during which the lamps were on. The purple section indicates the time during which ammonia is introduced to the chamber (5 minutes, 50 ppb)..... 88

Figure 5.4. ToF-AMS data for toluene/OH SOA under low NO_x (left) and high NO_x (right) conditions. The yellow region indicates the time during which the light was on for photooxidation. The purple region indicates the time during which ammonia was added to the chamber. The CHN family of ToF-AMS fragments is plotted in black in the top panels. The NH family of fragments is plotted in green in the middle panels. The NO family of fragments is plotted in red in the bottom panels. 93

Figure 5.5. ToF-AMS data for limonene/O₃ SOA under low NO_x (left) and limonene/OH SOA under high NO_x (right) conditions. The yellow region indicates the time during which the light was on for photooxidation. The purple region indicates the time during which ammonia was added to the chamber. The CHN family of ToF-AMS fragments is plotted in black in the top panels. The NH family of fragments is plotted in green in the middle panels. The NO family of fragments is plotted in red in the bottom panels. 94

Figure 5.6. Difference from base case in 24-hour average of PM_{2.5} when including ammonia uptake onto SOA using an uptake coefficient of 1×10^{-2} 97

Figure A.1. Summary of known photolysis products of 2-nitrophenol (2-NP) reported by Alif *et al.* (1991) 103

Figure A.2. Summary of known photolysis products of nitrobenzene (NB) by Barltrop *et al.* (1967, 1968) Solvents serving as good H-atom donors (isopropanol) promoted reduction of -NO₂ all the way to -NH₂..... 103

Figure A.3. Summary of expected and possibly observed monomeric products of photolysis of 2,4-DNP. These products could be expected in the photolysis of 2,4-DNP. Species with the expected m/z values appeared in the LC-MS spectra, which suggest (but does not prove) that they were present..... 104

Figure A.4. Summary of expected and possibly observed monomeric products of photolysis of 2,4-DNP. These products could also be expected in photolysis of 2,4-DNP but we saw no evidence of these products in the mass spectrum. 105

Figure A.5. Summary of expected and Possibly observed dimeric products of photolysis of 2,4-DNP. These dimeric products could also be expected in photolysis of 2,4-DNP. However, only the structure boxed in red is a possible match to the observed m/z of the eluting ions. 106

Figure A.6. PDA chromatogram of the observed photolysis products. This is a sample chromatogram corresponding to 350-500 nm integrated PDA absorbance. There are clear peaks growing at 11.8, 14.9, 16.3, 18.0, 20.7 and 32.6 min in the chromatogram during photolysis. The 11.8, 18.0 and 20.7 min peaks have the correct absorption spectrum characteristics (the corresponding spectra given below) for the expected products, which absorb to the red of 2,4-DNP. The 16.3 min peak is very weak. 107

Figure A.7. MS chromatograms at different photolysis times. In the MS chromatograms integrated over the 150-170 m/z range, where the majority of products are expected, there is a clear growth of several peaks during photolysis. 108

Figure A.8. PDA vs. MS Chromatogram for the 60 min photolyzed sample. The correlation between the MS and PDA chromatograms are shown by the red arrows. The MS chromatogram corresponds to an integration over the 150-170 m/z range. These peaks are also discernible in the TIC spectrum but they are easier to observe in this integration range. The peaks in the MS chromatogram are delayed relative to the corresponding peaks in the PDA chromatogram by about 0.4 min (the time needed for the slow to migrate form the PDA cell into the ESI source). 109

Figure A.9. Chromatograms, mass spectrum, and absorption spectrum for the 11.8 min peak. The 11.8 min peak in the PDA chromatogram correlates with the 12.3 min peak in the MS chromatogram. 110

Figure A.10. Chromatograms, mass spectrum, and absorption spectrum for the 14.9 min peak. The 14.9 min peak in the PDA chromatogram correlates with the 15.3 min peak in the MS chromatogram. 111

Figure A.11. Chromatograms, mass spectrum, and absorption spectrum for the 16.3 min peak. The 16.3 min peak in the PDA chromatogram correlates with the 16.7 min peak in the MS chromatogram. 112

Figure A.12. Chromatograms, mass spectrum, and absorption spectrum for the 18.0 min peak. The 18.0 min peak in the PDA chromatogram correlates with the 18.4 min peak in the MS chromatogram. 113

Figure A.13. Chromatograms, mass spectrum, and absorption spectrum for the 20.7 min peak. The 20.7 min peak in the PDA chromatogram correlates with the 21.2 min peak in the MS chromatogram. 114

Figure A.14. Chromatograms, mass spectrum, and absorption spectrum for 2,4-DNP.....115

Figure A.15. Chromatograms, mass spectrum, and absorption spectrum for the 27.9 min peak. The 27.9 min peak in the PDA chromatogram correlates to the 28.2 min peak in the MS chromatogram.116

Figure A.16. Chromatograms, mass spectrum, and absorption spectrum for the 31.6 min peak. The 31.6 min peak in the PDA chromatogram correlates to the 32.1 min peak in the MS chromatogram.117

LIST OF TABLES

	Page
Table 2.1. Physical parameters used in the simulations to determine viscosities of α -pinene-derived SOM (PSOM) and limonene-derived SOM (LSOM). R and r indicate the radius of the tube and the radius of the inner hole, respectively, for a half-torus geometry.	26
Table 3.1. Summary of MAGIC oxygen to carbon ratio characterization.....	49
Table 3.2. Estimated viscosities of the 20% toluene sample and the 80% toluene sample at 30% RH and 50% RH.....	54
Table 4.1. Examples of previous studies of the effect of RH on SOA yield.	58
Table 4.2. Summary of experiments. ^a	65
Table 4.3. Most abundant compounds observed in the low and high RH samples. ^a	72
Table 5.1. Summary of experiments. A green X represents experiments that have been completed and a red O represents experiments that will need to be done in the future.	86
Table 5.2: Nitrogen fraction in each type of sample exposed to ammonia.....	90
Table A.1. Summary of the compounds detected in LC-PDA-MS experiments.....	118

ACKNOWLEDGMENTS

There are many people that have, over the last five years, given me the support and encouragement I needed to accomplish my goal of earning a Ph.D. First and foremost, I would like to thank my advisor, Professor Sergey Nizkorodov, for welcoming me into the group and setting me up with interesting projects and great research partners. He has been there to help guide my research when I needed it and he has given me the freedom to work independently when I didn't. As a mentor, he always makes sure his students are taken care of and are doing well. Somehow, he always remembers what each student is working on, despite having ten different projects going on in the group at once. But, most importantly, he has given me a lot of support to pursue my interests and has provided me with a lot of opportunities for personal and professional development.

I would also like to thank my committee members, Professor Barbara Finlayson-Pitts and Professor Craig Murray. Professor Finlayson-Pitts has taught me a lot about atmospheric chemistry and gave me my first opportunity to do atmospheric chemistry research. She has remained an encouraging mentor for me throughout my time at UCI. Professor Craig Murray gave me great advice to help me advance to Ph.D candidacy as the chair of my advancement committee.

Another thank you goes to Professor Donald Dabdub, for all of his help. Working with him and his group for the last year has been really great. He has always been a source of support and overall positivity. He always make you feel like you are important and impressive. I am really glad I got to have him as a second P.I for the ammonia project.

In my first year at UCI, Sergey partnered me with Hanna Lignell, a senior graduate student in the lab. I want to thank Hanna for getting me started in the lab on the right foot. She was incredibly supportive and taught me a lot about the things I didn't know much about, like photochemistry, actinometry, and how to get out of being safety officer. We were a great team and often tag-teamed long experiments. I couldn't have asked for a better grad student mentor. I am so glad I was able to carry on our research after she graduated.

As I entered my fifth year at UCI, history kind of repeated itself, and Sergey partnered me with Julia Montoya, a second-year graduate student. I want to thank her for being a great research partner and being so meticulous with our experiments while I was distracted by writing and teaching. I always trusted the experiments that she did more than I trusted my own. Her organizational skills are amazing! I think we made a great team and I hope I was able to help her in the same way that Hanna helped me when I was just starting out, but I hope she knows how much her help meant to me in this last year.

Without going into too much detail, I would also like to thank all of the people in the Nizkorodov Group and AirUCI. I love how close-knit the atmospheric chemistry program is at UCI. The third floor of Rowland Hall has felt like a second home for the last five years because of all of the people supporting each other there. And thank you for Melissa Sweet for organizing such wonderful events for us all to get to know each other and always picking the best catering.

I especially want to thank my undergraduate and Master's research advisor at SDSU, Professor David Pullman. He gave me my first opportunity to work in a lab and taught me so much about research. He encouraged me to pursue a graduate career before I really even

knew what graduate school was. If he had not given me that opportunity I would not be where I am today or where I'm going in the future.

I also want to take a few sentences to thank Bri McWhorter for teaching me how to communicate effectively to a general audience. Her guidance has changed my perspective on science and sparked a passion for science communication. Working with her has given me a lot of confidence in myself. Not to mention she helped me win \$6000.

And thank you to my family! Thank you to my mom and dad for always encouraging me, even when that meant me moving farther away. Thank you for your support in all of the things I have done over the last 30 years. I would not be where I am today without everything you have done for me. Thank you to my sister Katie for always believing in me. She has always been my best friend and my biggest supporter. And last, but not least, I want to thank my boyfriend, Jeremy Eaton, for giving me so much support throughout graduate school. He has always believed in me, even when I did not. I couldn't ask for a better partner to move across the country with.

Finally, I need to thank the AirUCI NSF grant and the EPA grant for the funding they have provided. I would also like to thank the Chancellor's Club Fellowship for the support in the last year. Without all of this funding, this dissertation would not have been possible. Last, but not least, thank you to the journals, Physical Chemistry, Chemical Physics, and Environmental Science and Technology, for allowing me to republish my work in this dissertation.

CURRICULUM VITAE

Education

- 2012 – 2017 Ph.D. in Chemistry, University of California, Irvine
2008 – 2011 M.S. in Chemistry, San Diego State University
2004 – 2008 B.S. in Chemistry, San Diego State University

Research

- 2012 – 2017 Graduate Student Researcher, Aerosol Photochemistry Group,
Advisor: Professor Sergey Nizkorodov, University of California, Irvine
2012 Junior Specialist, AirUCI, Advisor: Professor Finlayson-Pitts,
University of California, Irvine
2008 – 2011 Graduate Student Researcher, Surface Chemistry Research Group,
Advisor: Professor David Pullman, San Diego State University
2007 – 2008 Undergraduate Student Researcher, Surface Chemistry Research
Group, Advisor: Professor David Pullman, San Diego State University

Awards and Honors

- 2017 UCI Chancellor's Club Fellowship
2016 1st Place – American Chemical Society ChemChamps Competition
2016 2nd Place – UC system-wide Grad Slam Competition
2016 1st Place – UCI Grad Slam Competition
2015 1st Place – UCI AGS Symposium

Publications

Montoya, J., Horne, J., **Hinks, M. L.**, Nizkorodov, S. A., Perraud, V., Lin, P., Laskin, A., Laskin, J., Dabdub, D. Secondary organic aerosol from oxidation of indole. *Submitted Atmospheric Chemistry and Physics* doi:10.5194/acp-2017-270

Hinks, M. L., Montoya, J., Ellison, L., Lin, P., Laskin, A., Laskin, J., Horne, J., Dabdub, D., Nizkorodov, S. A., Effect of relative humidity on the yield and composition of secondary organic aerosol from toluene. *Submitted Environmental Science and Technology*

Hinks, M. L., Brady, M. V., Lignell, H., Song, M., Greyson, J., Bertram, A. K., Lin, P., Laskin, A., Laskin, J., Nizkorodov, S. A., Effect of viscosity on photodegradation rates in complex secondary organic materials. *Physical Chemistry Chemical Physics*. 2015.

Lignell, H., **Hinks, M. L.**, Nizkorodov, S. A., Exploring matrix effects on photochemistry of organic aerosols. *Proceedings of the National Academy of Sciences of the United States of America*. 2014.

Espinoza, M.G., **Hinks, M. L.**, Mendoza, A. M., Pullman, D. P., Peterson, K. I., Kinetics of Decomposition of Silver Nanoparticles Induced by Halide Ions. *Journal of Physical Chemistry C*. 2012, 116, 8305-8313

Presentations

The Ammonia Puzzle: Interactions with Particles and Impacts on Air Quality. *AirUCI HIH/Landmark Symposium*, Irvine, CA, April 2017

Impact of Ammonia on Dynamics of Anthropogenic SOA Formation and Composition. *35th Annual AAAR Conference*, Portland, OR, October 2016

Viscosity Effects on Photochemical Processes in Secondary Organic Materials. *252nd ACS National Meeting*, Philadelphia, PA, August 2016

Effect of Viscosity on Photochemistry in Secondary Organic Material.

Pacificchem 2015, Honolulu, HI, December 2015

Photochemistry in Atmospheric Condensed Phases: Exploring the Effects of Matrix. *248th ACS National Meeting*, San Francisco, CA August 2014

Other Experience

2016 – 2017	Vice-President and Founding Member – Science Policy Group at UCI
2016 – 2017	Science Communication Fellow – The Loh Down on Science (KPCC)
2016 – 2017	Communication Consultant – UCI Graduate Resource Center
2014 – 2017	Head of Professional Development – Iota Sigma Pi – Calcium Chapter

ABSTRACT OF THE DISSERTATION

Effect of Environmental Conditions on Composition and Photochemistry of Secondary Organic Aerosols

By

Mallory Lynn Hinks

Doctor of Philosophy in Chemistry

University of California, Irvine, 2017

Professor Sergey Nizkorodov, Chair

Atmospheric aerosols represent one of the greatest uncertainties in predicting the Earth's future climate. Secondary organic aerosols (SOA) are particularly complicated because they are highly susceptible to change upon exposure to different conditions, such as varying temperatures and relative humidities (RHs), sunlight, and different atmospheric pollutants. The goal of this work was to increase our understanding of the contribution of SOA to the Earth's radiation budget by exploring how different environmental conditions can affect aerosol properties and processes.

The first project investigated the effect of viscosity on photochemical kinetics of probe molecules embedded in laboratory-generated SOA. Temperature and RH of the system were varied independently to adjust the viscosity of the SOA and the samples were irradiated. At lower temperatures and humidities both systems exhibited lower photoreaction rates, suggesting that increased viscosity hinders the motion of the molecules in the SOA slowing down their photochemical reactions. This means that molecules trapped inside SOA in cold, dry parts of the atmosphere will photodegrade slower than in warm and humid areas.

The next stage of this work was to study the effect of RH on the mass loading and composition of SOA formed from toluene photooxidation. When the RH was increased from 0% to 75%, the yield of toluene SOA made under low NO_x conditions decreased by an order of magnitude. High resolution mass spectrometry revealed a significant reduction in the fraction of oligomers present in the SOA made under humid conditions compared to dry conditions. These results suggest that water vapor suppresses oligomer formation in low NO_x toluene SOA, reducing aerosol yield. This means that concentrations of toluene SOA in the atmosphere will be dependent on the RH and NO_x concentrations.

The last stage of this work investigated the interaction between SOA and ammonia. SOA made from toluene, n-hexadecane, or limonene in a chamber was exposed to gaseous ammonia while the mass loading and composition was monitored. These experiments indicated that ammonia could be taken up into SOA, leaving less ammonia in the atmosphere to neutralize atmospheric acids. This leads to a reduction of inorganic aerosols in the atmosphere.

CHAPTER 1

INTRODUCTION

1.1: GENERAL BACKGROUND ON ATMOSPHERIC AEROSOLS

Atmospheric aerosols are made up of a collection of solids, liquids, and gases suspended in the atmosphere. Aerosols attract a lot of attention from scientists because they represent one of the greatest uncertainties in predicting the Earth's future climate.¹⁻² Aerosols can influence the Earth's radiative budget directly by scattering or absorbing incoming solar radiation.¹⁻³ These direct effects depend on the optical properties of the aerosol particles, such as the extinction and absorption coefficient of the materials from which the particles are made.¹⁻³ For instance, black carbon (soot) and brown carbon (large, heavily conjugated organic molecules) in particles effectively absorb light⁴ and contribute to the overall warming of the climate.⁵⁻⁶ Aerosols can also influence climate through indirect effects by acting as cloud condensation nuclei (CCN) and ice nuclei (IN). The concentration of CCN in clouds can impact the lifetime and radiative properties of the clouds.¹⁻³ In addition to their climate effects, aerosol particles have been shown to negatively impact human health.⁷⁻¹³ Long-term exposure to fine particulate matter (PM_{2.5}, particles < 2.5 μm in diameter) has been shown to increase the risk for lung cancer,⁸ cardiovascular mortality,⁷⁻⁸ and a decrease in overall life expectancy.⁹ Lastly, aerosols can severely limit visibility in urban areas.¹⁴⁻¹⁶

Organic aerosols, which are made up of organic compounds containing mainly carbon, nitrogen, oxygen, and hydrogen, dominate the total amount of particulate matter in the atmosphere.¹⁷⁻¹⁹ These aerosols can enter the atmosphere through two general pathways. Primary aerosols are emitted directly via processes such as the burning of fossil fuels or biomass.²⁰ Secondary aerosols are formed by gas-phase and multi-phase chemical reactions in the atmosphere. However, the distinction between these two types of aerosols becomes

less well-defined as the air mass containing aerosols travels around the globe. Primary aerosols can evaporate under ambient conditions, converting a substantial portion of their mass to the gaseous species.²⁰ These vapors can then undergo chemical reactions similar to those typical of secondary aerosol processes, and the products of these reactions can condense back onto particles.²⁰ Therefore, aerosols that have been “aged” in the atmosphere for some time may exist in a “grey” area somewhere between the original labels of primary or secondary.

The term “secondary organic aerosols” (SOA) covers a wide range of ambient aerosols. They form when volatile organic compounds (VOCs) react with oxidants such as ozone, hydroxyl radical, or nitrate radical to form successively lower volatility products that condense into the particle phase of SOA.²¹⁻²³ The chemical and physical properties of the resulting SOA are highly dependent on the starting VOC, the oxidant, and the conditions of oxidation. Ozone and hydroxyl radical play a major role in this process in the daytime, while nitrate radical is the main oxidant during the nighttime hours.¹⁶ These reactions can occur in gas-phase, aqueous phase of cloud fog droplets,²⁴ and/or involve more than one phase, as in multi-phase chemistry.²⁵

The VOCs that act as SOA precursors are emitted from both anthropogenic and biogenic sources. Biogenic VOCs capable of forming SOA include isoprene (C_5H_8), monoterpenes (a diverse group of compounds with the chemical formula $C_{10}H_{16}$), sesquiterpenes (which have the formula $C_{15}H_{24}$), and larger compounds. Global emissions of isoprene are estimated at about 600 TgC (teragram carbon) per year.²⁶ Isoprene alone makes up the largest portion (70%) of the total biogenic VOC emissions by mass.²⁷ Monoterpenes, as a group, make up

about 10% of this total and sesquiterpenes contribute 2.5%.²⁷⁻²⁸ Although isoprene was initially assumed to not contribute significantly to aerosol formation in the atmosphere,²⁹ even a small yield of isoprene SOA is significant on the global scale.³⁰ Because of their large SOA yields, monoterpenes are expected to contribute to a large portion of the total atmospheric SOA mass.³¹ Sesquiterpenes have been shown to have even higher SOA yields, but their contribution is relatively small because of the low emissions of sesquiterpenes compared to isoprene and monoterpenes.³²⁻³³ In this work, the focus was placed on monoterpenes. Some of the most important monoterpenes include α -pinene and d-limonene, which comprise 34% and 9% of total monoterpene emissions by mass, respectively.²⁷ These compounds are generally emitted by tree leaves and saps.³⁴⁻³⁶

Anthropogenic VOCs encompass a wide range of chemical compounds, which can include alkanes, aromatics, and olefins.³⁷ These VOCs are emitted mainly from industrial solvent usage, and from combustion engines.¹⁶ Benzene, toluene, and xylenes are an important component of anthropogenic VOC emissions because they are used as a surrogate group for the aromatic VOCs as a whole.³⁷ These compounds are expected to contribute significantly to the total SOA mass in the southern California air basin.³¹ Toluene and xylenes, in particular, have been shown to produce SOA with relatively high yields.^{31, 38} Therefore, benzene, toluene, and p-xylene were selected to represent anthropogenic VOCs in this work. The structures of the biogenic and anthropogenic VOCs used in this work are provided in Figure 1.1.

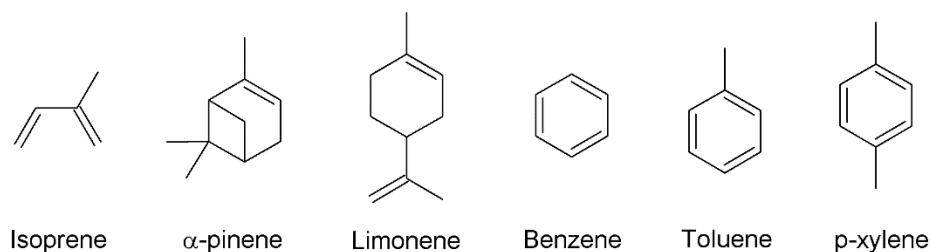


Figure 1.1. Structures of common biogenic and anthropogenic VOCs.

The oxidation of VOCs produces highly complex SOA. Laboratory experiments have shown that the oxidation of a single VOC can produce secondary organic material (SOM) made up of thousands of different compounds.³⁹⁻⁴² However, the ambient environment is much more complicated. When SOA particles are produced in the atmosphere, there could be many different VOCs being oxidized in parallel. Therefore, the chemical composition of ambient SOA is even more varied and complex than the SOA studied in the laboratory. Nevertheless, laboratory-generated SOA represent convenient models for studying chemical processes in SOA under controlled conditions.

1.2: ATMOSPHERIC AGING OF SOA

The properties of SOA continue to change long after the initial formation, which generally increases their complexity. The physical and chemical processes driving this change are collectively referred to as particle “aging”.⁴³⁻⁴⁴ It was already mentioned in section 1.1 that aging processes can contribute to the blurring of lines between primary and secondary aerosols. More importantly, when particles are exposed to different conditions in the atmosphere, their chemical composition and physical properties may change. Ambient SOA particles are regularly exposed to a variety of environmental conditions, which prompt the

change in chemical composition, and hence properties. For example, sunlight is an ever-present driver of chemical change to SOA particles because of its ability to produce gaseous free radicals that react with particles⁴³ and induce photochemical reactions directly in the particles.⁴⁴ Not all aging processes are driven by sunlight, however. SOA particles may encounter reactive gaseous pollutants in the atmosphere, such as ammonia, aldehydes, peroxides, epoxides, etc., and uptake of these pollutants onto aerosol surfaces can alter the chemical and physical properties of SOA.⁴⁵ As particles are exposed to temperatures ranging from -50 °C to over 25 °C, relative humidities (RH) from nearly 0% to over 100%, and diurnal cycle of irradiance, it is important to understand the mechanism of aging processes over a broad range of environmental conditions.

Arguably one of the most important climate effects of aging chemistry is the change of the particle absorption coefficient. During aging processes driven by solar irradiation, the absorption coefficient of the SOA may either increase⁴⁶ or decrease.⁴⁷⁻⁴⁹ In most cases, however, the absorption coefficient is thought to decrease when SOA is exposed to actinic radiation, a process referred to as photobleaching.⁴⁸ Furthermore, irradiation may alter the size or mass of the particles,⁵⁰⁻⁵³ which affect the light-scattering ability of the particles. These changes in optical properties are driven by the changes in the chemical make-up of SOA.^{45, 48, 50-56} As the SOA particles are irradiated, embedded photolabile molecules are broken down into smaller photoproducts. This process has been shown to reduce the peroxide content^{50, 56} of the SOA as well as cause particles to lose mass by emitting volatile photoproducts such as formic acid.⁵³ Under aqueous conditions, wherein SOA compounds are dissolved in cloud or fog droplets, irradiation can reduce the concentration of nitrogen-

containing organic compounds⁵⁴ and high molecular weight compounds in the SOA particles.⁵²

As will be discussed in detail in section 1.3, the SOA particle phase or viscosity is expected to be highly dependent on both temperature⁵⁷ and RH.⁵⁸⁻⁷² Furthermore, RH has significant impacts on particle mass loading and composition, which will be discussed in section 1.4 with a more comprehensive literature review in section 4.1.

Heterogeneous aging of SOA mainly involves the reactive uptake, or mass transfer from the gas phase to the particle phase, of other atmospheric pollutants. This type of aging includes oxidative aging, which occurs when atmospheric oxidants are taken up by SOA particles, changing their physical and chemical properties.⁴³ One process that has not been studied as extensively is the uptake of reducing agents, such as ammonia, onto SOA particles. This process will be discussed further in section 1.5.

1.3: EFFECTS OF AEROSOL PHASE

Investigations into the phase state of secondary organic aerosol (SOA) suggest that under certain conditions, both atmospheric and laboratory-generated SOA particles may behave as semi-solids or amorphous solids rather than liquids.⁵⁸⁻⁷² This realization has important implications for our understanding of processes occurring within SOA. Viscosity is expected to play a role in many of these processes, including the dynamics of particle growth,^{63,73} gas-particle partitioning,⁷⁴⁻⁷⁶ diffusion kinetics of water, oxidants, and other compounds,^{64,68,77-79} particle aggregation,⁶⁵ and reactive uptake on particle surfaces.⁸⁰⁻⁸⁴ Diffusion limitations imposed by the increased viscosity of SOA have already been shown to impact the particle

growth rates and mechanisms as well as the oxidation rates of organics within the SOA.^{59, 63, 68, 75, 77} However, it has been shown that between 40% and 90% RH the diffusion of molecules within toluene SOA particles is fast enough to achieve equilibrium gas-particle partitioning.⁸⁵ This suggests that, under typical ambient conditions (~50% RH) diffusion limitations will not be as relevant.⁸⁵ Under dry conditions in the atmosphere, on the other hand, these findings will be more pertinent.

The effect of temperature on the viscosity of SOA has not been extensively studied. However, temperature is known to change the viscosity of many different types of materials. A decrease in temperature from 20 °C to 0 °C will decrease the viscosity of α -pinene/O₃ SOA by roughly two orders of magnitude as discussed in Lignell *et al.*⁸⁶ This estimate was based on the glass transition viscosity of SOM and the average glass transition temperature of major products of α -pinene ozonolysis.^{59, 87} Recently, Rothfuss *et al.* measured the viscosity of aerosol surrogates as a function of temperature and determined that the viscosity of their sucrose/SDS system decreases by roughly two orders of magnitude upon increasing the temperature from ~78 °C to ~88 °C.⁵⁷ Therefore, we expect that the viscosity of ambient SOA is highly dependent on the temperature of the surrounding atmosphere. Specifically, as the temperature of the system increases, the viscosity of the SOA should decrease.

The effect of RH on SOA viscosity has been studied more extensively and is also expected to have a significant effect on the viscosity of SOA particles.^{58-60, 63-72} Water molecules entering the particles act as a plasticizer, decreasing the viscosity of the material. As the RH of the system increases, the SOM from which the particle is made will decrease in viscosity.

Additionally, the viscosity of SOA is highly dependent on the chemical composition of the particle, and generally increase with the degree of oxidation of the SOA compounds.⁸⁸ Therefore, the VOCs that the SOA are produced from will have a large role in determining the SOA viscosity. The viscosity of SOA made from α -pinene or limonene has been shown to be much lower than the viscosity of SOA made from toluene or benzene.^{46, 89}

1.4: EFFECTS OF WATER ON SOA

RH has significant effects on SOA extending beyond affecting the viscosity of the particle material. A detailed discussion of the current literature on effects of water on SOA composition and concentration is provided in section 4.1. Briefly, RH can alter the composition and concentration of SOA in the atmosphere in multiple ways. Water vapor can directly participate in VOC oxidation reactions.⁹⁰ For instance, it can react with stabilized Criegee intermediates formed during ozonolysis.⁹⁰ In addition, water present in hygroscopic particles can lead to hydrolysis of organic compounds and other particle-phase reactions.⁹¹ It can also have a strong effect on acidity of particles and can affect acid-catalyzed processes occurring in particles.⁹² Finally, under supersaturated conditions, aqueous chemistry occurring in cloud and fog droplets promotes photolysis driven conversion of small water-soluble molecules into non-volatile products that would not form in the absence of liquid water,²⁴ as well as photodegradation of dissolved SOA compounds.^{52, 54, 93-94} Due to the multiple effects of RH on the SOA formation mechanism, the SOA yield could potentially either increase or decrease as a function of RH.

1.5: EFFECTS OF AMMONIA ON SOA

One important pollutant that aerosol particles will commonly encounter in the atmosphere is ammonia. It enters the atmosphere from a variety of sources including automobiles, industry, and biomass burning.⁹⁵⁻⁹⁷ However, the largest contribution of ammonia to the atmosphere comes from agriculture, including animal waste and fertilizer application.⁹⁵⁻⁹⁷ Agriculture accounts for roughly half of the total ammonia emissions globally.⁹⁵⁻⁹⁷

In southern California, the amount of ammonia emitted by automobiles is on the same order of magnitude as the amount of ammonia emitted from agricultural sources.⁹⁸ However, automobiles are decentralized while agricultural sources of ammonia are more localized. Thus, ammonia coming from automobiles will be in low concentrations distributed across a large area, and ammonia coming from agricultural areas in southern California will be in high concentrations in a small area.⁹⁸ Therefore, the impacts of ammonia are important to understand in those areas.

Atmospheric ammonia is well known to neutralize acids, such as nitric acid or sulfuric acid producing inorganic salts. These salts can then aggregate to form inorganic aerosols. These inorganic aerosols, as opposed to organic aerosols, are generally made up of ammonium, nitrates, sulfates, sodium, and chloride. This acid-neutralization process contributes significantly to PM_{2.5} in southern California.⁹⁹⁻¹⁰⁰

Recent evidence has shown that ammonia can react with compounds in SOA by mechanisms other than simple acid-base chemistry. Biogenic SOA made from limonene that was exposed to ammonia was observed to undergo a browning process as a result of chemical reactions

between ammonia and carbonyl species within the secondary organic material (SOM). This process leads to the formation of highly-conjugated, light-absorbing, nitrogen-containing organic compounds (NOC).¹⁰¹⁻¹⁰⁵ The general mechanism involves the reaction of ammonia with carbonyls within the SOA to produce primary imines and amines, which may stabilize by intramolecular cyclization into heteroaromatic products based on imidazole, pyrrole, indole, etc.¹⁰⁶

Liu *et al.* recently reported chemical uptake coefficients for ammonia onto α -pinene SOA and m-xylene SOA.¹⁰⁷ The uptake coefficients were calculated from the change in nitrogen mass in the SOA particle before and after exposure to ammonia. Additionally, a different Liu *et al.* studied the formation of SOA from gasoline-powered vehicle exhaust in the presence and absence of ammonia. They found that particle mass loading increased rapidly in the presence of ammonia.¹⁰⁸ The increase was observed to be much higher in the presence of ammonia compared to its absence.¹⁰⁸ These studies have demonstrated the need to investigate this process in more depth and incorporate these effects into air quality models.

It is important to understand the interactions between SOA and ammonia, given that various global trends point toward an increase in ammonia emissions. The global human population is expected to continue growing in the future, which will increase agricultural production. The number of cattle and buffalo, which contribute to the largest amount of ammonia due to livestock waste, is expected to increase by 360 million relative to the 1999 cattle population (1.497 billion animals).¹⁰⁹ These trends indicate that the concentration of ammonia will increase significantly over the next few decades, particularly in areas where the surrounding human population is growing the fastest. According to the Food and Agriculture

Organization of the United Nations, annual ammonia emissions from livestock are expected to increase by 60% (or 18,000 metric tons) by 2030 from 1999 levels.¹⁰⁹ This increase will be most evident in developing countries, where the annual ammonia emissions are projected to increase by 17,000 metric tons.¹⁰⁹ Additionally, ammonia emissions have been shown to increase significantly under warmer temperatures.¹¹⁰⁻¹¹² A projected increase in temperature of 2-4 °C due to climate change could lead to overall increases of up to 27% in ammonia emissions.¹¹³ This increase in temperature is also expected to increase emission of VOCs from most sources,¹¹⁴ which will lead to more SOA. Because both ammonia emissions and SOA production will be increasing in the coming decades, it is important to understand how their interactions will affect particle concentration and composition.

The variable nature of SOA makes their effect on climate and human health difficult to predict. Understanding how SOA particles change under different conditions will help us better understand them and allow us to more easily model their behavior. By reducing the uncertainty in the effect of SOA and other types of aerosols on climate and ultimately health, we will be better prepared to implement the necessary regulations to combat climate change and prevent unnecessary deaths.

CHAPTER 2

EFFECT OF VISCOSITY ON PHOTODEGRADATION RATES INSIDE COMPLEX SECONDARY ORGANIC AEROSOL MATERIAL

Portions of this chapter are reproduced with permission from: Hinks, M. L.; Brady, M. V.; Lignell, H.; Song, M.; Grayson, J. W.; Bertram, A. K.; Lin, P.; Laskin, A.; Laskin, J.; Nizkorodov, S. A., Effect of viscosity on photodegradation rates in complex secondary organic aerosol materials. *Physical Chemistry Chemical Physics* **2016**, *18* (13), 8785-8793.

2.1: INTRODUCTION

Recent investigations into the phase state of secondary organic aerosol (SOA) have suggested that under certain conditions, both atmospheric and laboratory-generated SOA particles may behave as semi-solids or amorphous solids rather than liquids.⁵⁸⁻⁶³ This realization has important implications for our understanding of processes occurring within SOA material. The rheological properties of organic aerosols, such as viscosity, are expected to play a role in the dynamics of particle growth,^{63, 73} gas-particle partitioning,⁷⁴⁻⁷⁶ diffusion kinetics of water, oxidants, and other compounds,^{64, 68, 77-79} the dynamics of particle aggregation,⁶⁵ and reactive uptake on particle surfaces.⁸⁰⁻⁸³ Diffusion limitations imposed by the increased viscosity of SOA have already been shown to impact the particle growth rates and mechanisms as well as the oxidation rates of organics within the SOA.^{59, 63, 68, 75, 77}

Environmental conditions such as temperature and relative humidity (RH) are expected to have a significant effect on the viscosity of SOA particles.^{58-60, 63-69} As either temperature or RH of the system is increased, the secondary organic material (SOM) from which the particle is made will decrease in viscosity. For example, Renbaum-Wolff *et al.* reported that the viscosity of α -pinene/O₃ SOM increases by several orders of magnitude upon reducing the RH from 90% to 30%.⁶⁰ The effect of temperature on the viscosity of SOM has not yet been studied, but we estimate that a decrease in temperature from 20 °C to 0 °C will decrease the viscosity of α -pinene/O₃ SOM by two orders of magnitude, as discussed in Lignell *et al.*⁸⁶

The goal of this work is to investigate the effect of SOM matrix properties on the photochemical kinetics of photolabile, organic molecules within the SOM by varying the temperature and RH. Experiments were performed on three types of organic matrix

including α -pinene/ O_3 SOM (PSOM), limonene/ O_3 SOM (LSOM), and aged limonene/ O_3 SOM obtained by exposure of LSOM to ammonia (brown LSOM). These particular systems were selected for two main reasons. First, PSOM and LSOM are common SOA materials in both outdoor and indoor environments: α -pinene is the most important precursor to global SOA and limonene is the most important indoor SOA precursor.¹¹⁵⁻¹¹⁶ Second, brown LSOM was selected to test both the effect of exposure to ammonia on the viscosity of LSOM and to examine a different type of photochemistry. (We did not do experiments with PSOM exposed to ammonia because reaction of PSOM with ammonia, unlike that of LSOM, does not lead to browning.)⁴⁸ Although the elemental composition of LSOM and PSOM components is quite similar, with average O/C ratios of 0.39 and 0.37 respectively, the viscosity of PSOM is likely to be greater than that of LSOM because the products of α -pinene ozonolysis tend to be more structurally rigid.^{39, 106} Similarly, brown LSOM may be physically and chemically different from LSOM because it contains products of reactions of NH_3 with carbonyls.¹⁰⁶ Understanding how viscosity of SOA may play a role in the photochemical kinetics of different types of atmospheric molecules trapped within them is important in order to better predict the lifetimes of toxic pollutants.

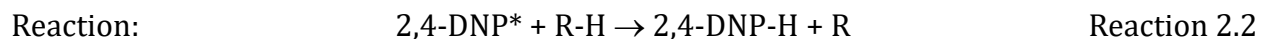
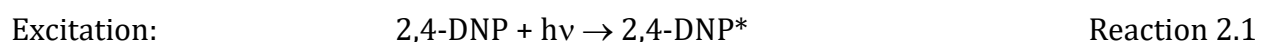
Ideally, these experiments should be done with submicron aerosol particles, similar to the ones found in the atmosphere, in order to maintain the correct time scale for the gas-to-particle exchange of volatile products and reactants (e.g., molecular oxygen dissolved in the particles) of the photochemical processes occurring in particles. However, experiments performed with aerosol particles would be more difficult and suffer from potential interference from competing gas-phase photochemical processes.⁴⁴ We have chosen to simplify the experiments by working with the bulk phase of SOM collected on a substrate.

For photochemical reactions that involve only condensed-phase reactants and products, bulk SOM experiments should provide the same information as experiments with aerosols.

As PSOM and LSOM photodegrade relatively slowly, a strongly absorbing, nitroaromatic pollutant 2,4-dinitrophenol (2,4-DNP) was dispersed in the SOM films to serve as a photochemical probe molecule. This compound enters the environment predominantly from pesticide use, manufacturing plants, biomass burning, and motor vehicles.¹¹⁷⁻¹²⁰ It is known to be present in surface and atmospheric waters and in organic matter. Although mixing of 2,4-DNP and biogenic SOA is unlikely, we use 2,4-DNP just as probe of SOM matrix effects on photochemistry. The photodegradation of 2,4-DNP upon UV irradiation is accompanied by a decay in its absorbance at 290 nm and an increase in absorbance in the visible region of the spectrum, where PSOM and LSOM do not absorb, due to the formation of photoproducts.⁸⁶

2,4-DNP is expected to photodegrade by a mechanism shown in Reactions 2.1-2.4. As 2,4-DNP is irradiated, it is excited to a triplet state (Reaction 2.1) and proceeds to abstract a hydrogen atom from a neighboring molecule possessing weakly-bound hydrogen atoms (Reaction 2.2). Saturated hydrocarbons, aromatic hydrocarbons, and water are not suitable hydrogen donors in this reaction, whereas alcohols and aldehydes readily participate in the H-atom transfer. We assume that the rate of reaction 2.2 may be diffusion (and thus viscosity) limited. Diffusion limitations in a more viscous matrix would allow more time for competing deactivation (Reaction 2.3) to occur, thus preventing formation of 2,4-DNP photoproducts (Reaction 2.4). For example, 2,4-DNP* would need just a few nanoseconds to diffuse 0.6 nm (a reasonable estimate for the distance to the closest abstractable H-atom) in a moderately viscous solvent such as octanol (viscosity $\sim 7 \times 10^{-3}$ Pa s), but it would need

several milliseconds to diffuse the same distance in PSOM (viscosity $\sim 10^4$ Pa s). The latter time is more than sufficient for the dissipation of the electronic excitation energy into heat. The excited states lifetime of 2,4-DNP has not been reported, but based on the triplet lifetimes of related nitrobenzene and nitrophenols (ortho, meta, and para) determined by Takezaki *et al.* we expect it to be < 1 ns.¹²¹ Therefore, diffusion limitations may arise in materials with viscosity comparable to that of PSOM.



Our previous study examined the photochemistry of 2,4-DNP at a range of temperatures in three different environments: water, octanol, and PSOM.⁸⁶ It was found that the rate of photochemical degradation of 2,4-DNP in PSOM was more strongly affected by temperature than the same reaction in octanol. We proposed that viscosity of the matrix is a key factor affecting the rates of photoreactions occurring in PSOM. However, other interpretations of the observations could not be excluded, for example, a different reaction mechanism in PSOM compared to octanol. To further investigate the possible matrix effects on the photochemistry of 2,4-DNP, we extended our measurements to various temperatures and RHs in two different types of matrices – PSOM and related material LSOM.

The third system examined in this study is brown LSOM formed by exposing fresh LSOM to ammonia vapors and drying the sample. It has a distinctive absorption band at 510 nm that, in combination with tails of UV absorption bands extending into the blue region of the

spectrum, give the material a characteristic brown color.^{101, 103-104, 106, 122} Lee *et al.* found that an aqueous solution of brown LSOM readily photobleaches after several minutes of exposure to UV radiation; the peak at 510 nm decays and the brown color disappears.⁴⁸ Because this system photodegrades quickly and possesses a distinct UV-absorbing functionality, an additional probe molecule was not used. Although the molecular nature of the actual chromophore is not presently known, it is likely to be an oligomeric, nitrogen containing compound formed by condensation reactions between SOA carbonyls and ammonia.¹⁰⁶

We find that all three model systems exhibit similar behavior wherein photodegradation rate is increased at higher temperature or higher RH. While the temperature effects can result from a number of factors, the fact that there is also an RH dependence suggests that viscosity is an important factor in photochemical reactions taking place within matrices. Increased viscosity may be hindering the motions of the molecules in the SOM and therefore slowing down the photochemical reactions in which they participate.

2.2: EXPERIMENTAL

For these experiments, it was necessary to collect a large amount of SOM in a short amount of time. Therefore, a continuous aerosol flow reactor was used. The 20 L flow tube produces high quantities of SOA by dark ozonolysis of an SOA precursor volatilized under a flow of dry air. A diagram of the flow tube is given in Figure 2.1 below. Ozone was produced using a commercial ozone generator at a mixing ratio of 70 ppm. The precursor, either α -pinene (98%, Alfa Aesar) or limonene (97%, Sigma-Aldrich) was introduced to the flow tube by injecting the liquid via syringe pump into a dry air flow. The precursor evaporates into the

air flow and is carried into the flow tube, where it reacts with the ozone, producing SOA. The residence time of the flow tube was about 4 minutes.

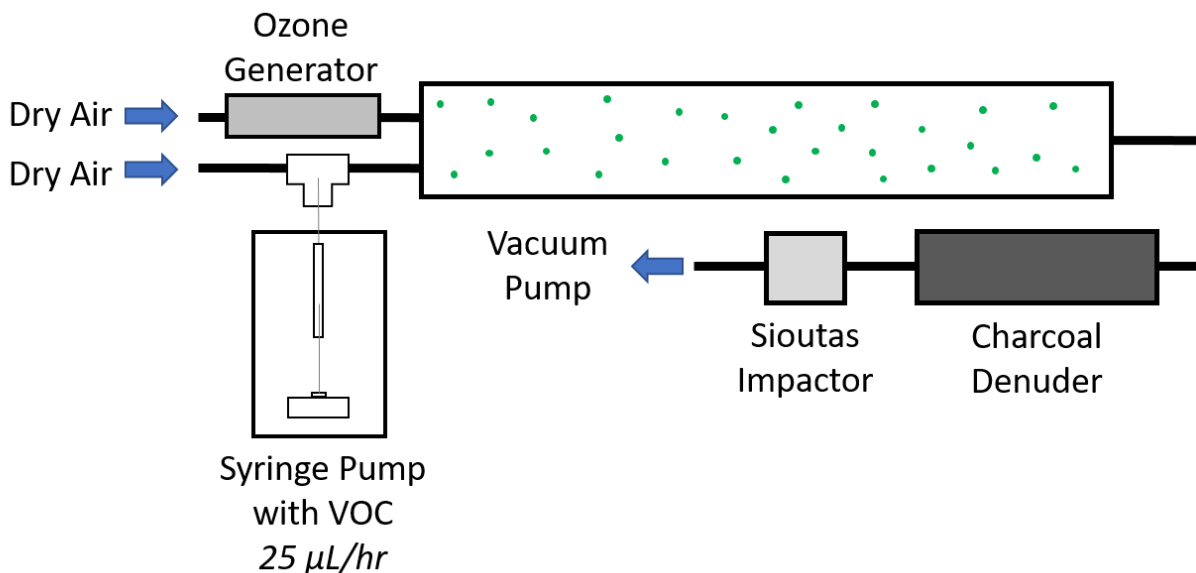


Figure 2.1. Diagram of the flow tube.

After leaving the flow tube, the SOA passed through a charcoal denuder to strip away excess ozone and VOCs. Then the SOM was collected on a 25 mm CaF₂ window with a Sioutas impactor equipped with a single stage D (0.25 μm cut point at 9 SLM collection flow rate). The original collection stage for the Sioutas impactor was designed for collection on foil substrates, so this collection stage was customized to accept a much thicker substrate like CaF₂ windows. A collection time of 45 minutes typically produced about 2 mg of SOM deposited on the window. As the SOA is impacted onto the window, it accumulated in a line as shown in Figure 2.2. Then the SOM was prepared for the photochemistry experiments as described below.

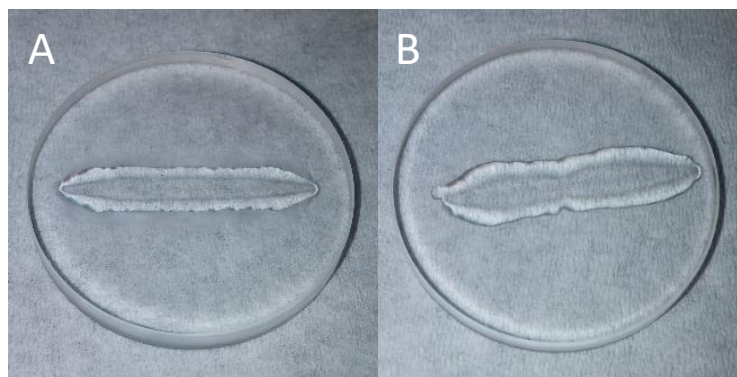


Figure 2.2. SOA after impactation of A) α -pinene SOA and B) limonene SOA made in the aerosol flow tube.

Three sets of experiments were performed in this study. The three systems investigated consisted of α -pinene SOM with 2,4-DNP, limonene SOM with 2,4-DNP, and brown limonene. For the 2,4-DNP experiments, the SOM was embedded with 2,4-DNP using a 100 μ L aliquot of 2,4-DNP in methanol. Then the SOM/2,4-DNP system was made into a thin film using one of two methods.

In the earliest experiments with α -pinene SOM, the film was made using the “sandwich technique”, where the SOM and 2,4-DNP was pressed between two CaF_2 windows. However, this method was not ideal. It resulted in the formation of bubbles within the film during longer photochemical experiments. These bubbles sometimes interfered with the UV-vis measurements of the film. Photos of the SOM in each stage of this preparation process is shown in Figure 2.3.

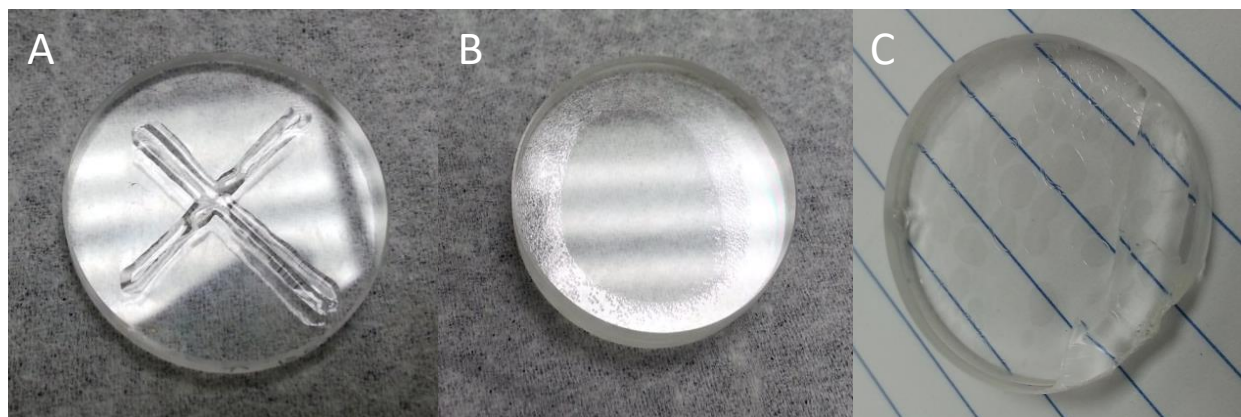


Figure 2.3. Photos of α -pinene SOM made in the flow tube. A) Fresh SOM collected in an X pattern. B) Sandwich technique for making SOM films. C) The bubbles produced within the film during long experiments between two (damaged) CaF_2 windows.

To address this issue, I used a different method for forming films, termed the “open-faced sandwich technique”. This method combined the embedding step with the film making step. A 100 μL aliquot of 2,4-DNP in methanol was pipetted onto the window. The methanol dissolves the SOM and as it evaporates distributes the SOM evenly across the window surface while simultaneously leaving the 2,4-DNP embedded within the SOM (Figure 2.4). This method was used for the limonene SOM/2,4-DNP system.

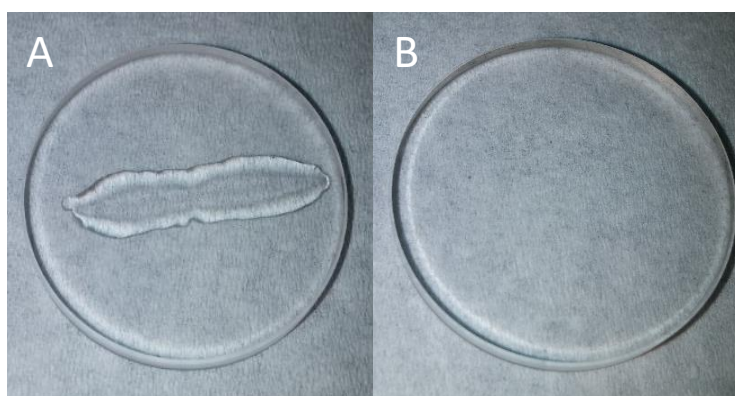


Figure 2.4. A) Freshly collected limonene SOM from the flow tube and B) open-faced sandwich film of limonene SOM embedded with 2,4-DNP.

The brown limonene SOM system was prepared by creating an “open-face sandwich” thin film of freshly made LSOM by pipetting 100 μL of methanol onto the window. Then the window with the thin film of LSOM was placed in a small petri dish, which was then placed inside a large petri dish filled with 30 mL of 0.1 M ammonium sulfate (>99%, EMD). Then the lid to the large petri dish was placed over both petri dishes. This technique allows the LSOM to absorb the vapors (estimated to contain 300 ppb ammonia using the AIM-II model) without touching the solution. The entire unit of petri dishes was stored in a dark cupboard for two days. Then the sample was removed, placed in a temperature and RH controlled photoreaction box, also known as Scott’s Solid State Setup or SSSS. Inside the SSSS, the thin film of LSOM was dried under a flow of dry air for an hour, after which the sample had browned. A picture of the brown limonene sample before and after NH_3 treatment is shown in Figure 2.5.

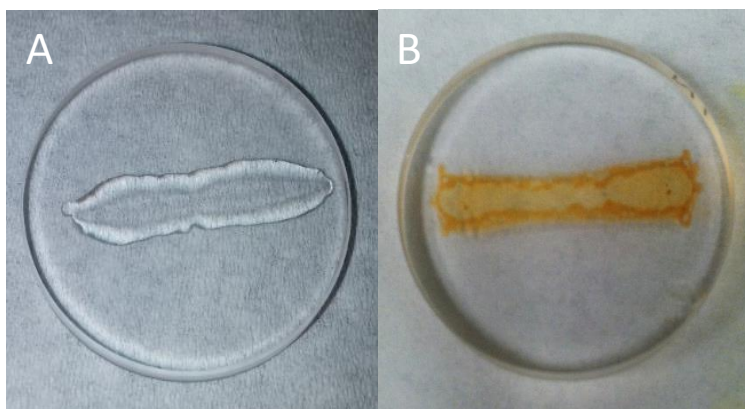


Figure 2.5. A) Freshly collected limonene SOM from the flow tube and B) limonene SOM after exposure to NH_3 and drying (“Brown” limonene SOM)

After each sample was prepared, it was irradiated inside the SSSS. A diagram of this setup is shown in Figure 2.6. The sample was situated on top of a quartz microscopy slide within the SSSS. The temperature of the slide was controlled using a circulating water cooler connected

to an aluminum heat sink. This water cooler technique was able to achieve temperatures ranging from 0 °C to 25 °C. However, we were interested in doing experiments below 0 °C. In order to reach even lower temperatures, two Peltier coolers (TE Technology, Inc. TC-48-20) were used in tandem with the water cooler. Throughout the experiment temperature was monitored using a type-K thermocouple mounted on the microscope slide.

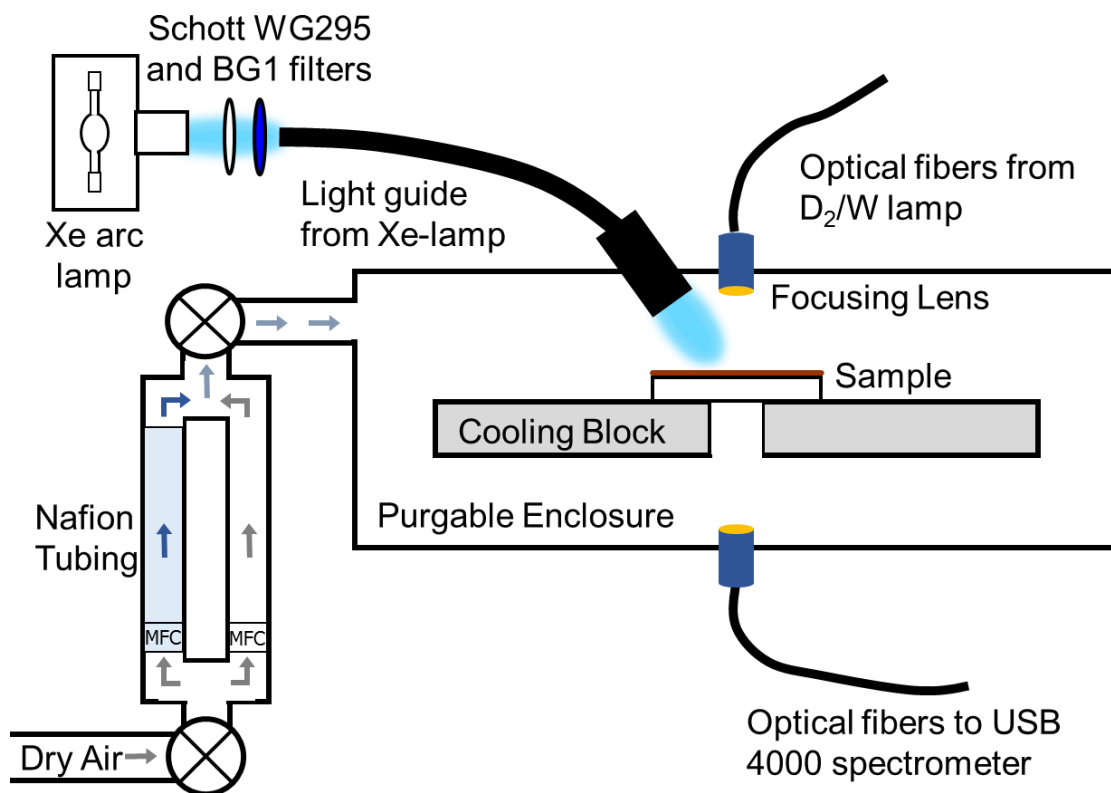


Figure 2.6. A schematic diagram of the SSSS used to irradiate each sample at a range of RHs and temperatures.

The RH within the SSSS was adjusted by mixing flows of dry (<2% RH) and wet (>98% RH) air. Dry air was split into two separate flows. The flow rate of each flow could be controlled independently through two mass flow controllers. One flow passed through a Nafion drier/humidifier (PermaPure) while the other flow passed through standard ¼" Teflon

tubing of the same length. The humidified air was recombined with the dry air as the flows entered the box of the SSSS. The resulting RH could be tuned by adjusting the flow through each mass flow controller. A Vaisala HMP237 humidity probe was used to measure the viscosity inside the SSSS.

A 150 W xenon arc lamp (Newport model 66902 lamp housing) was used as the irradiation source in these experiments. In order to restrict the light coming from the xenon arc lamp to the wavelengths that are most relevant for tropospheric photochemistry, the light produced by the lamp was first reflected by a 280-400 nm dichroic mirror and passed through a 295 nm long-pass filter (Schott WG295) and UV band-pass filter (Schott BG1). This resulted in a wavelength range of 290-400 nm. This light was then piped into the SSSS using a liquid light guide (Edmunds #53-691) at a 15° angle with respect to the film normal.

We used a custom spectrometer setup to record absorptions spectra of the sample film. This setup consisted of a D₂/W light source coupled to an Ocean Optics USB4000 spectrometer. The radiation from the light source was piped into the SSSS, across the sample, and to the spectrometer using 600 μm optical fiber cables.

In order to study the effect of RH on viscosity and gain insight into the effect of viscosity on photochemical kinetics occurring with SOA particles we collaborated with Allan Bertram's group at University of British Columbia (UBC). SOM samples made in the flow tube were collected using the Sioutas impactor onto substrates coated with trichloro(1*H*,1*H*,2*H*,2*H*-perfluorooctyl)silane (Sigma-Aldrich). These substrates were coated by the Bertram group. As the SOA particles were collected onto the hydrophobic substrates from the flow tube, they

coagulated into supermicron SOM particles. The substrates with the supermicron particles were sent to UBC to perform poke-flow viscosity measurements.

The poke-flow measurements were performed on the samples in a RH-controlled flow-cell. A needle mounted on a micromanipulator was allowed to pass through a small hole in the flow-cell to poke the particles. When a particle was poked with the needle a hole appeared in the previously hemispherical shape. When the needle was removed, the hole slowly shrank as the particle returned to its original shape. The entire process was monitored and recorded with a reflectance optical microscope (Zeiss Axio Observer, 40× objective) equipped with a CCD camera. The poke-flow time was defined as the time needed for the hole to shrink to half of its diameter immediately after the needle was removed. Photos of this process are shown in Figure 2.7 below.

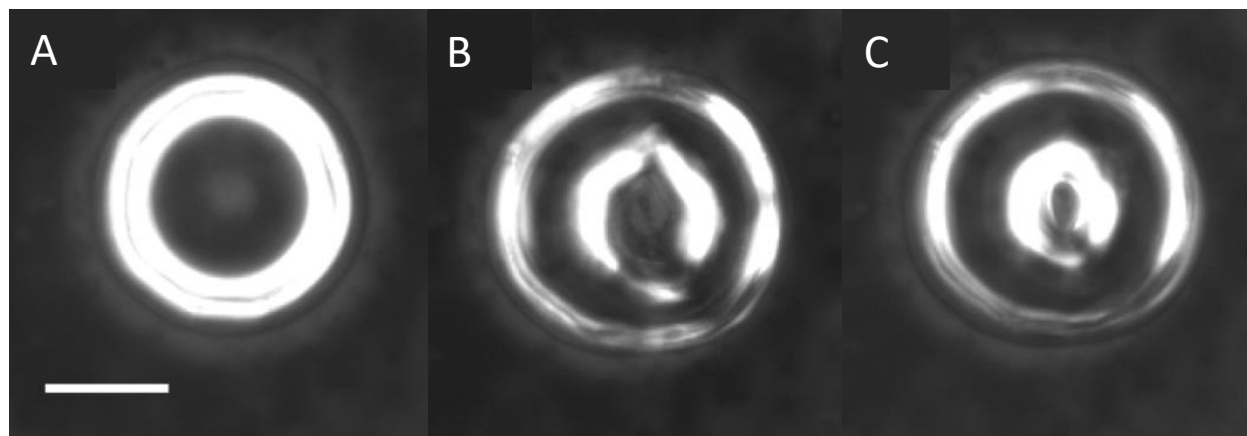


Figure 2.7. Optical microscope images of an SOM particle A) before poking, B) immediately after being poked, and C) after recovering $\frac{1}{2}$ of the initial hole diameter.

Simulations of fluid flow were carried out using *COMSOL Multiphysics* (version 4.3a) to convert $\tau_{(exp, flow)}$ values into viscosity.^{67, 123} In the simulations, a half-torus geometry with an inner radius, R , and a tube radius, r , were required. These values were set to match the

experiments, and the viscosity was varied until the modeled flow time, $\tau_{(mod, flow)}$, was equal to $\tau_{(exp, flow)}$. The physical parameters needed for these simulations include: slip length (the interaction between the fluid and solid surface), surface tension and density of the SOM, and the contact angle at the particle-substrate interface. Upper and lower limits of the parameters used in these simulations are provided in Table 2.1.

Table 2.1. Physical parameters used in the simulations to determine viscosities of α -pinene-derived SOM (PSOM) and limonene-derived SOM (LSOM). R and r indicate the radius of the tube and the radius of the inner hole, respectively, for a half-torus geometry.

		Slip length (nm) ^a	Surface tension (mN m ⁻¹) ^b	Density (g cm ⁻³) ^c	Contact angle (°) ^d
PSOM	Values for lower limit	5	40	1.30	70 (if $r < 2R$), 90 (if $r > 2R$)
	Values for upper limit	10000	75	1.30	90 (if $r < 2R$), 70 (if $r > 2R$)
LSOM	Values for lower limit	5	23	1.47	60 (if $r < 2R$), 80 (if $r > 2R$)
	Values for upper limit	10000	72	1.67	80 (if $r < 2R$), 60 (if $r > 2R$)
Brown LSOM	Values for lower limit	5	23	1.47	65 (if $r < 2R$), 80 (if $r > 2R$)
	Values for upper limit	10000	72	1.67	80 (if $r < 2R$), 65 (if $r > 2R$)

^a Refs. 124-137

^b For PSOM, surface tension values were based on the viscosity of model compounds.¹³⁸ For LSOM and brown LSOM, surface tension values were based on the estimated surface tension of liquid limonene at 293 K (as the lower limit) and the surface tension of pure water at 293 K (as the upper limit) values from ACD/Labs (chemspider.com) and Engelhart *et al.*¹³⁹

^c For PSOM, density values are based on Chen and Hopke, 2009.¹⁴⁰ For LSOM and brown LSOM, density values are based on values from Kostenidou *et al.*¹⁴¹

^d Contact angles (70-90° for PSOM and 60-80° for LSOM) were determined using 3-D fluorescence confocal images of the SOM particles on the substrates.

Previous validation experiments with sucrose-water particles and high viscosity standards have shown that the poke-flow technique combined with simulations of fluid flow is capable of providing both lower and upper limits of viscosity that are consistent with literature or measured values when the viscosity of particles are in the range of 5×10^2 to 3×10^6 Pa s.¹²³ The major source of uncertainty in the viscosity of the SOM arises from uncertainty in the physical properties of SOM that are used in simulations (i.e., values shown in Table 2.1). Particle to particle variability of $\tau_{(exp, flow)}$ is typically small.

2.3: RESULTS AND DISCUSSION

The absorption spectra of (a) 2,4-DNP in LSOM and (b) brown LSOM taken during the course of photodegradation are presented in Figure 2.8. The absorption spectra for 2,4-DNP in PSOM is very similar to 2,4-DNP in LSOM, so the absorption spectra is not included in Figure 2.8. The inset of each graph corresponds to the absorbance decay at the representative wavelength for each system (290 nm for 2,4-DNP in LSOM and PSOM, and 510 nm for brown LSOM). The combined absorbance from the SOM and the reactant can be expected to follow Equation 2.1,

$$A(t) = A_{SOM} + A_0[\beta + (1 - \beta) \times e^{-kt}] \quad \text{Equation 2.1}$$

where A_{SOM} is the absorbance due to the SOM matrix, assumed to be unchanged by photolysis, A_0 is the starting absorbance due to the reactant, k is the photodegradation rate constant, and β is the ratio of the absorption coefficient of the photolysis product(s) to that of the reactant at the wavelength of interest. (The value of β is 0 for non-absorbing products, smaller than 1 for weakly absorbing products, 1 at the isosbestic point, and larger than 1

when products absorb stronger than the starting compound.) Since we were interested only in the values of k , the observed decays were fit using the simplified equation:

$$A(t) = \text{const}_1 + \text{const}_2 \times e^{-kt} \quad \text{Equation 2.2}$$

to obtain rate constants for each set of experimental conditions. The use of Equation 2.2 automatically accounts for any uncompensated wavelength-independent offsets in the absorbance measurements.

It should be noted that in the case of 2,4-DNP, the decay in absorbance at $\sim 250 - 320$ nm is accompanied by an increase in the broad absorption band in the visible range ($\sim 400 - 450$ nm) indicating formation of a brown carbon product (a result of reduction of one of the $-\text{NO}_2$ groups to $-\text{NH}_2$ group as discussed below). The rate constants k determined from Equations 2.1 and 2.2 at 290 nm (decrease in absorbance, $\beta < 1$, $\text{const}_2 > 0$) and 420 nm (increase in absorbance, $\beta > 1$, $\text{const}_2 < 0$) were the same within the uncertainties of the fitting.

The increase in the visible absorbance of the irradiated 2,4-DNP samples is an important observation for two reasons. First, it confirms recent findings that photochemical processing is capable of altering the light absorption properties of brown carbon.^{48-49, 142} Second, it shows that, depending on the system, photochemical processes in brown carbon are capable of creating light-absorbing compounds, not just destroying (photobleaching) them. Our work provides evidence that brown carbon has a dynamic absorption spectrum that can be altered on atmospherically relevant time scales via photochemistry.

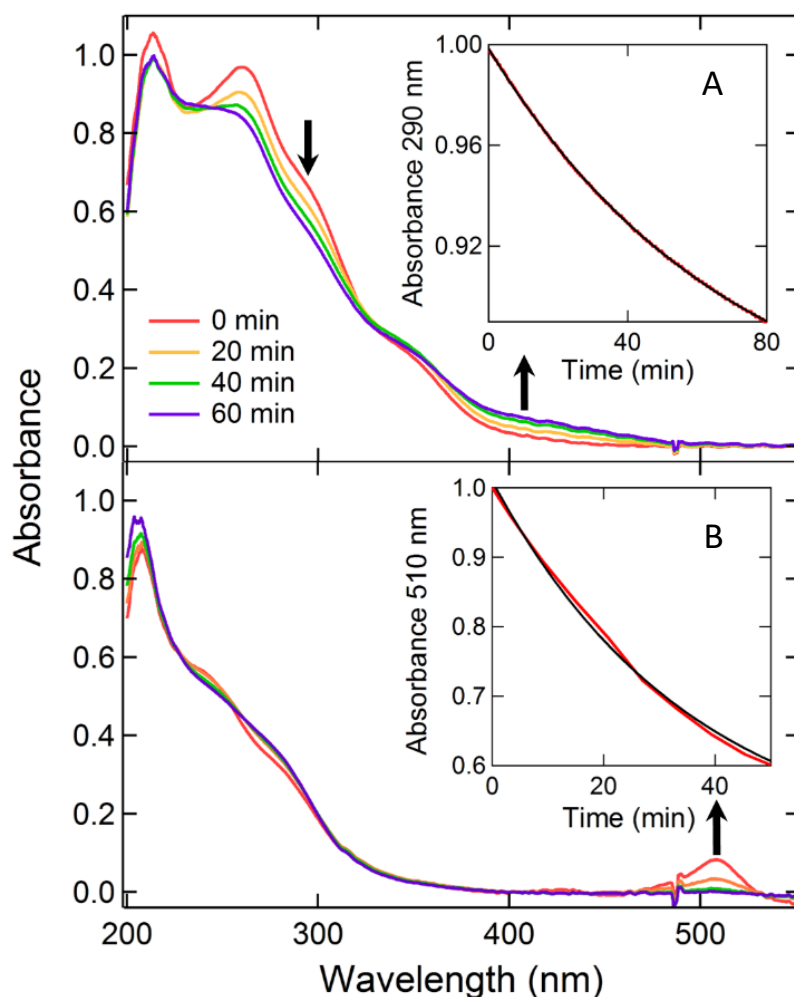


Figure 2.8. Representative absorption spectra recorded during the photodegradation of A) 2,4-DNP in LSOM and B) brown LSOM. The insets show the decay of A) the 290 nm peak of 2,4-DNP and B) the 510 nm peak characteristic of the brown LSOM chromophore where the red trace is the experimental decay and the black trace is the fit to Equation 2.2. The arrows indicate the wavelength at which spectra were fit to Equation 2.2 to get the rate constants.

To investigate the mechanism of 2,4-DNP photodegradation, we performed LC-PDA-MS (liquid chromatography coupled to a photodiode array detector and an electrospray ionization high-resolution mass spectrometer) measurements on irradiated samples of 2,4-DNP in isopropanol (0, 30, and 60 min of irradiation in a quartz cuvette by the same light source as used for the film experiments). Isopropanol was used as the solvent in this analysis

because it allowed for a simpler spectrum than SOM would have, as SOM is very complex and is made up of many different molecules that would yield a complicated background spectrum.³⁹ The full results of the LC-PDA-MS analysis, as well as experimental details, are provided in the supporting information section. We assigned the observed products of photodegradation of 2,4-DNP by analogy with photochemistry of related compounds, nitrobenzene and 2-nitrophenol. Based on the m/z values and UV-vis absorption spectra of the eluted peaks, we were able to assign products to the structures shown in Figure 2.9. We emphasize that we did not have standards for any of these compounds for unambiguous identification, so the assignments should be regarded as tentative. Nevertheless, our results strongly suggest that photoreduction of $-NO_2$ group(s) in 2,4-DNP is the main mechanism of photodegradation. We observed peaks corresponding to an $-NH_2$ (aniline) product as well as to an $-NO$ (nitroso) intermediate which is expected for this process. Based on the UV-vis absorption spectra (Figure A.9 in the appendix) the compounds containing an aniline group are likely the ones responsible for the brown color of the 2,4-DNP photodegradation products after the irradiation and cause the growth of the visible absorption band at ~ 400 - 450 nm. The formation of aniline products has significant implications for understanding the environmental fate of 2,4-DNP because of the high reactivity of aniline compounds.

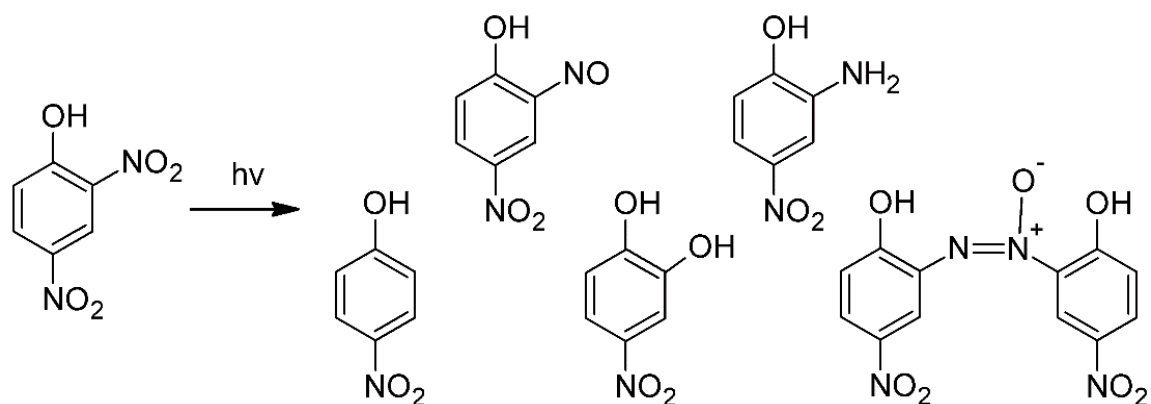


Figure 2.9. Products tentatively identified by LC-PDA-MS after 2,4-DNP photolysis in isopropanol. Details leading to the assignments are provided in the supporting information section.

Regarding the kinetics of 2,4-DNP photodegradation, as discussed in Lignell *et al.*,⁸⁶ the effective activation energy of reactions with low intrinsic barriers is determined by the surrounding matrix's viscosity, which depends strongly on temperature. The photodegradation of 2,4-DNP fits this profile – it has low activation energy in octanol and much higher activation energy in PSOM, likely due to the high viscosity of the PSOM film.⁸⁶ The activation energy of each system studied in the current work was determined using the Arrhenius plot shown in Figure 2.10. This plot illustrates the relationship between temperature and rate constant for each system (including 2,4-DNP in PSOM shown previously in Ref. ⁸⁶) under dry conditions. The results indicate that the activation energy of the photodegradation of 2,4-DNP in LSOM (24 ± 1 kJ/mol) is lower than that in PSOM (48 ± 6 kJ/mol). If these activation energies are actually viscosity-dependant, then this suggests that PSOM has a higher viscosity than LSOM. Another observation of the current work is that both of the reactions that occurred in LSOM (2,4-DNP and brown LSOM) had similar activation energies (24 ± 1 kJ/mol and 16 ± 5 kJ/mol, respectively) implying that the

viscosities of LSOM and brown LSOM are similar. This would be consistent with minor compositional differences between the two materials.¹⁰⁶

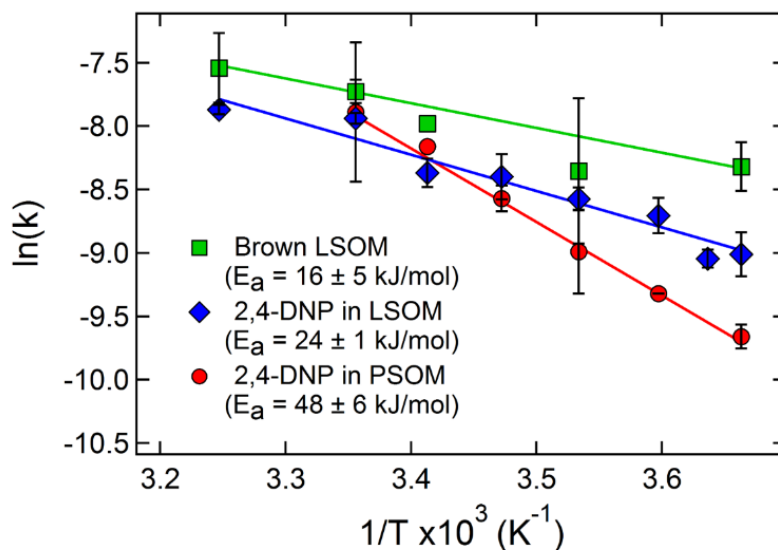


Figure 2.10. Arrhenius plots of the photodegradation rate of 2,4-DNP in PSOM (red), 2,4-DNP in LSOM (blue), and brown LSOM (green) under dry conditions. The slopes correspond to activation energies of 48, 24, and 16 kJ/mol, respectively. Markers with no error bars represent experiments that were performed once. All other markers are the average of 2-6 data points obtained at each temperature.

In order to test this hypothesis, the viscosities of LSOM and PSOM generated in our flow tube were experimentally determined from poke flow experiments at different RHs, specifically, by measuring how quickly a half-sphere of SOM returns to its original shape after being distorted by a needle. The results of these experiments are shown in Figure 2.11.

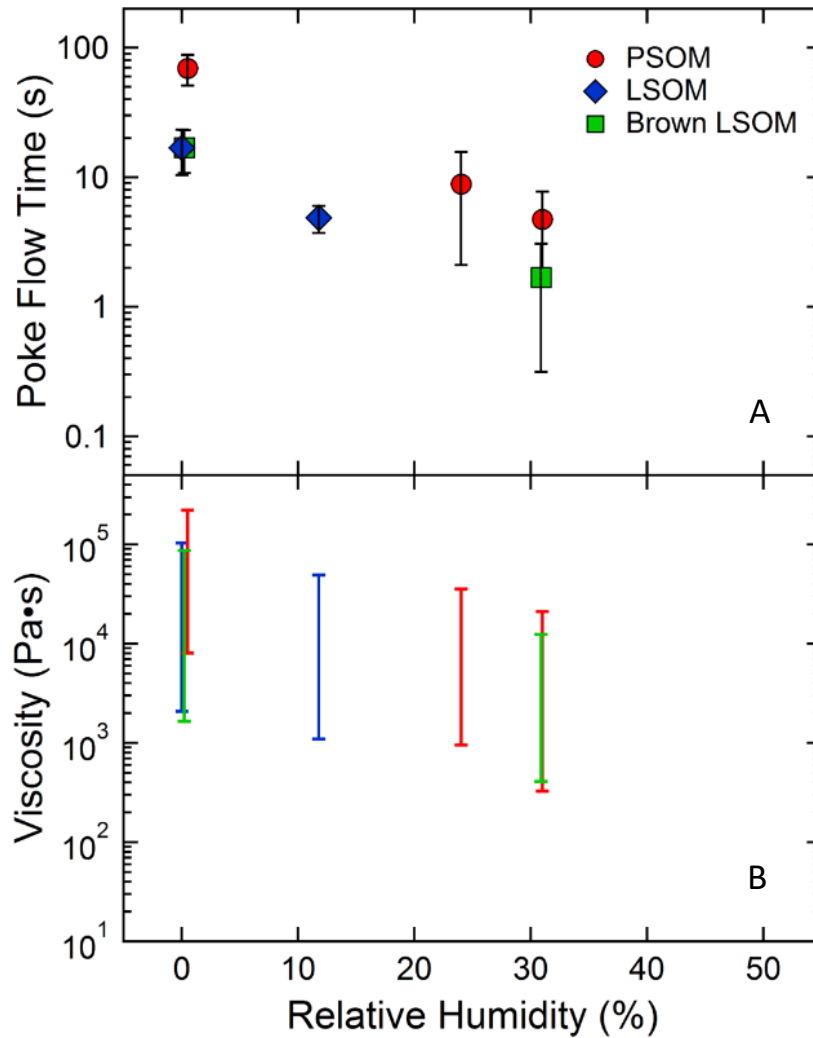


Figure 2.11. A) Average experimental flow time from the poke-flow experiments as a function of relative humidity. The markers correspond to the average of 4-11 individual poke flow measurements. The error bars represent one standard deviation for the repeated measurements. B) Simulated ranges of viscosities as determined by upper and lower limits. The error bars are dominated by uncertainties in the fitting parameters listed in Table 2.1.

Figure 2.11a depicts the average experimental flow time, which is taken for the equivalent area diameter to decrease to 50 % of its initial diameter. The PSOM had a longer experimental flow time than either LSOM or brown LSOM. For example, under dry conditions the experimental flow time of PSOM is longer by approximately an order of magnitude than

the experimental flow times of LSOM and brown LSOM, strongly suggesting a higher viscosity. Unlike the clearly different poke flow times in PSOM and LSOM, the error bars on the absolute viscosity values shown in Figure 2.11b overlap because of the sensitivity to the model parameters needed to convert the poke flow times into the viscosity values. However, the simulated upper and lower limits of viscosity also suggest that PSOM is more viscous than LSOM or brown LSOM. These results are qualitatively consistent with larger apparent activation energies for the photodegradation of 2,4-DNP in PSOM vs. LSOM. It is also clear from Figure 2.11 that the viscosity of SOM is strongly related to RH, which is in agreement with previous measurements.⁶⁰

Irradiation of all systems under a range of RHs revealed that as RH was increased, the photoreaction rate constant increased (Figure 2.12). The number of data points in Figure 2.12 is limited because each point requires several days of experiments, however, the increase in the rate with RH is clear. We interpret this to be the result of water molecules softening the SOM matrix and allowing for the photoexcited molecules to diffuse to their reaction partners faster. We note that liquid-liquid phase-separation (LLPS) is possible in PSOM at very high RH > 95%,¹⁴³⁻¹⁴⁴ but the increase in the photodegradation rate is also observed at lower RH. Therefore we do not think that LLPS is responsible for the RH dependence of the photodegradation rate. The change of RH seemed to have a larger effect on the brown LSOM system than either of the 2,4DNP/SOM systems. This is most likely due to the fact that 2,4-DNP photodegrades extremely slowly in water.⁸⁶ As water molecules are introduced to the film, the rate of photodegradation may be increased due to decreased viscosity, but it is partly offset by the dilution of the molecules that 2,4-DNP can react with. The photodegradation of brown LSOM, on the other hand, is not affected by the presence of

water molecules. Therefore, the increase in the rate of photodegradation due to decreased viscosity will be greater for brown LSOM than for 2,4-DNP in LSOM or PSOM which may explain the larger RH dependence seen in brown LSOM.

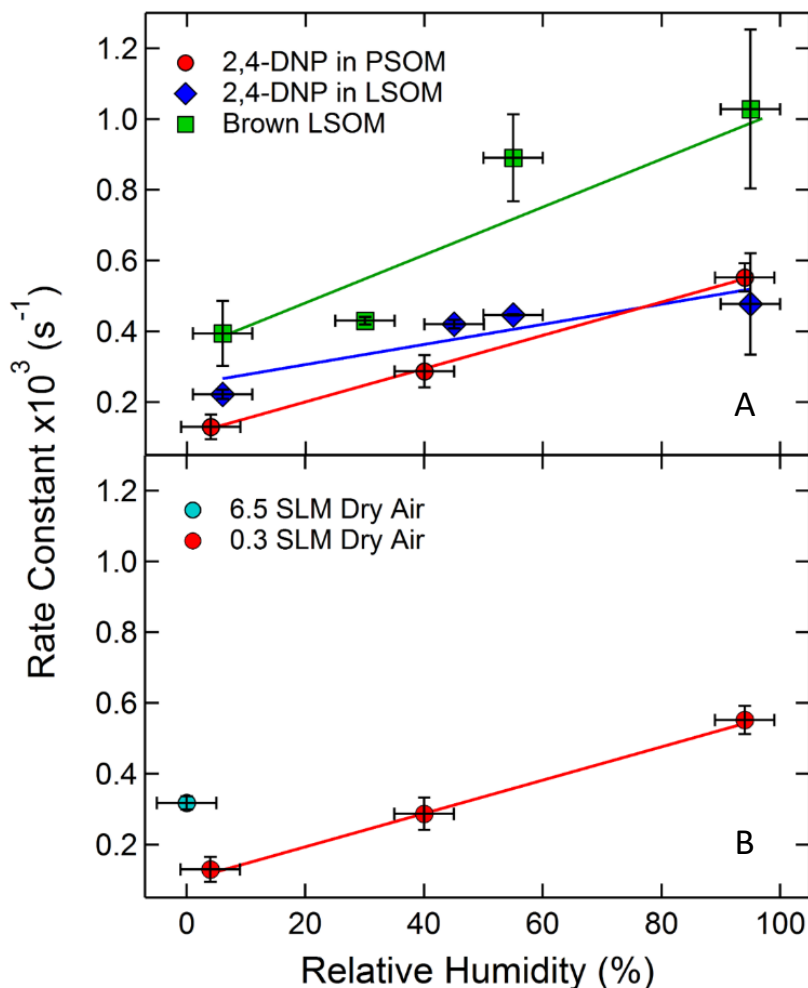


Figure 2.12. A) The rate constants as a function of relative humidity for the photodegradation of 2,4-DNP in PSOM 2,4-DNP in LSOM, and brown LSOM. Each marker with error bars represents the average of all the data points at each RH. These experiments were repeated 2-6 times. The slopes of the fit were $(4.7 \pm 0.1) \times 10^{-6}$, $(2.9 \pm 0.9) \times 10^{-6}$, and $(8 \pm 2) \times 10^{-6} \text{ s}^{-1}/\%RH$ for 2,4-DNP in PSOM 2,4-DNP in LSOM, and brown LSOM respectively. Plot B) demonstrates the effect of drying speed.

We should point out that viscosity is not the only property of SOM that can change with RH. It is conceivable that the presence of water in the SOM film changes the molecular composition by means of hydration of aldehydes, hydrolysis of anhydrides, and other reactions involving water. For example, hydrolysis reactions of organonitrates in aerosols have been observed at the RH levels used in this work.¹⁴⁵ While these reactions may also contribute to the observed changes in the photodegradation rate, the physical effect of RH on the SOM viscosity likely dominates over the chemical effect of RH on the molecular composition of SOM. Additional experiments with materials that are not reactive towards water are needed to fully separate the chemical and physical effects of RH.

Koop *et al.* and other groups have previously found that the viscosity of an aerosol particle at a particular RH strongly depends on the rate at which the system is dried/humidified.^{59, 146-148} It has been suggested that drying quickly will cause water molecules nearest the surface of the particle to evaporate quickly, creating a highly viscous “crust” that prevents water molecules in the interior of the particle from escaping. This results in an aerosol particle that contains a lower viscosity core.^{59, 146} Drying more slowly allows more time for water molecules within the particle to diffuse to the outer layers and evaporate, causing the particle to be more uniform in terms of viscosity. Thus the interior viscosity of the slowly dried particle is actually expected to be higher than that of the interior of the quickly dried particle.

In our studies, the lowest RH experiments were performed under two different flow rates of dry air (6.5 SLM and 0.3 SLM). We found that the samples that were dried under a high flow rate of dry air photodegraded more quickly than samples dried under the slower flow rate.

This was a reproducible effect, demonstrated by Figure 2.12b (note the small vertical error bars calculated from the repeated experiments). The red dots correspond to samples of 2,4-DNP in PSOM that were dried/humidified under a 0.3 SLM flow rate, and the light blue dot represents the samples that were dried under a 6.5 SLM flow rate. The fast dried samples with a low viscosity core had a photodegradation rate that was a factor of ~ 3 higher than the slow dried samples with a high viscosity core. This provides additional indirect evidence that the viscosity of SOM plays an important role in the photodegradation of these systems.

These results suggest that certain types of photochemical reactions may be suppressed in condensed-phase environment of the highly-viscous aerosols relative to the same reactions in common organic solvents. In particular, photochemical processes involving secondary reactions of electronically-excited organic molecules with the matrix constituents are likely to be affected by the diffusion limitations, and therefore, by the viscosity. This scenario clearly applies to 2,4-DNP, which photodegrades by a reaction of its triplet excited state with suitable hydrogen atom donors (reactions 2.1-2.4). The photodegradation rate of the unidentified chromophore in the brown LSOM is similarly affected by viscosity. However, we want to emphasize that not all organic photochemical reactions will be suppressed in viscous aerosols by the same mechanism. Direct photolysis processes occur on faster time scales and do not require the excited molecules to diffuse through the matrix before the reaction. Such reactions are less likely to be affected by the material viscosity; for example, Norrish-I splitting of carbonyls can be efficient even in crystals.¹⁴⁹ On the other hand, caging effects could be more significant in highly-viscous solvents, and result in suppression of direct photolysis quantum yields. Therefore, the effects of viscosity on photochemical reactions need to be investigated on a case by case basis.

These results could help in the interpretation of atmospheric lifetimes of particulate nitroaromatic compounds, some of which are known toxins. In cold and dry segments of the atmosphere, such as over the polar regions and near the tropopause, these compounds could survive longer if they are trapped inside highly-viscous particles. In contrast, the same compounds could degrade faster under warm, humid conditions or when they are unprotected on the particle surface. It is possible that other types of photolabile organic compounds can similarly be protected from photodegradation under cold, dry conditions. It is also possible that photosensitized reactions can similarly be suppressed by the viscosity of the SOM matrix. These effects will need to be investigated in future studies. It also remains to be seen if these conclusions can be applied to other types of SOA, including those formed from anthropogenic sources.

2.4: CONCLUSIONS

In our previous work,⁸⁶ we found that the photodegradation rate of 2,4-DNP in viscous PSOM had a significantly stronger temperature dependence than the same process in much less viscous octanol. We suggested that this effect was due to the fact that temperature has a stronger effect on the viscosity of PSOM than on the viscosity of octanol. The increased viscosity may be hindering the motion of electronically excited 2,4-DNP molecules within SOM, slowing its photodegradation. In order to examine this effect, we expanded the scope of the previous measurements to investigate the effect of relative humidity on the photodegradation kinetics of 2,4-DNP in PSOM. We also investigated LSOM as an alternative organic matrix for 2,4-DNP photodegradation, and carried out similar experiments with a completely different photochemical system, specifically brown LSOM obtained by exposure

of LSOM to ammonia. In all cases, as the viscosity of the SOM was increased by cooling the material or exposing it to dry air, the reaction rate decreased. The activation energy for the 2,4-DNP photodegradation in PSOM and LSOM were correlated with the explicitly measured viscosity of the materials.

CHAPTER 3

EFFECT OF SOA COMPOSITION ON VISCOSITY AND PHOTOCHEMISTRY

3.1: INTRODUCTION

The viscosity of various types of secondary organic aerosol (SOA) has been an important topic of investigation recently.⁵⁸⁻⁶³ It is expected to play a role in many aerosol processes, such as the dynamics of particle growth,^{63, 73} gas-particle partitioning,⁷⁴⁻⁷⁶ diffusion kinetics of water, oxidants, and other compounds,^{64, 68, 77-79} the dynamics of particle aggregation,⁶⁵ and reactive uptake on particle surfaces.⁸⁰⁻⁸³, as discussed in Chapters 1 and 2.

We are particularly interested in the effect of viscosity on photochemical processes. Previously, we studied this effect by varying the temperature of the secondary organic material (SOM) and the RH of the surrounding atmosphere to indirectly adjust the viscosity of the SOM.⁴⁶ However, it is well established that increasing temperature of a material will change the rate of photochemical reactions independent of viscosity. And although RH controls the viscosity of SOM, it also adds water to the SOM system. It is possible that the water could change the molecular composition of the SOM by hydration of aldehydes, hydrolysis of anhydrides, and other reactions involving water. For example, Liu *et al.* found that organonitrates in aerosols could undergo hydrolysis at RHs greater than 50%.¹⁴⁵ This chemistry significantly reduced the concentration of organonitrates in the aerosols and thus changed the composition of the particles.¹⁴⁵ These reactions may also contribute to the observed changes in the photodegradation rate. Therefore, it is difficult to decouple the effect of temperature or RH on SOM photochemistry from the effect of viscosity.

To further investigate the effect of viscosity of SOM photochemistry, it would be useful to have a method of directly manipulating the viscosity of SOM at a given temperature and RH. The logical approach is to mix two SOA precursors that independently produce SOM with

drastically different viscosities and vary the mixing ratio between them. Our previous experiments described in Chapter 2 focused on viscous biogenic SOM from alpha-pinene and limonene.⁴⁶ Comparing our previous work to Song *et al.* showed that the viscosity of SOM formed from toluene is several orders of magnitude higher than limonene or α -pinene SOM.^{46, 89} Therefore, mixtures of toluene and limonene were chosen for these experiments.

The goal of this study was to investigate if viscosity of SOM could be controlled by varying the ratio of toluene and limonene and if these differences in viscosity affected photochemistry of the SOM. Mixtures of VOCs are routinely photooxidized in smog chambers to produce SOA, however, the chambers do not produce enough material for the photochemical experiments. In previous photochemistry experiments, described in Chapter 2, an aerosol flow reactor was used to produce large amounts of SOM from either limonene or α -pinene by dark reaction with ozone. This flow tube produces SOM at high rate but does not generate high SOA yields from toluene ozonolysis because ozone will not readily attack toluene's aromatic pi bonds. To address this issue, I built a different flow reactor, similar in design to the Oxidation Flow Reactor (OFR) that generates high quantities of SOA by photooxidation of VOCs at very high OH concentrations. The reactor will be referred to as Mallory's Aerosol Generating Irradiation Chamber (MAGIC) in this thesis.

3.2: AEROSOL GENERATION – MAGIC

MAGIC is designed to generate large amounts of SOA by photooxidation of VOCs. Hydroxyl radical (OH) is produced by photolysis of ozone under humid conditions. Then, OH oxidizes the SOA precursor, producing SOA, which we can collect and use in photochemical

experiments. This reactor consists of an 8 L reaction vessel surrounded by 2 UV lamps that emit 254 nm radiation. A diagram of MAGIC is provided in Figure 3.1.

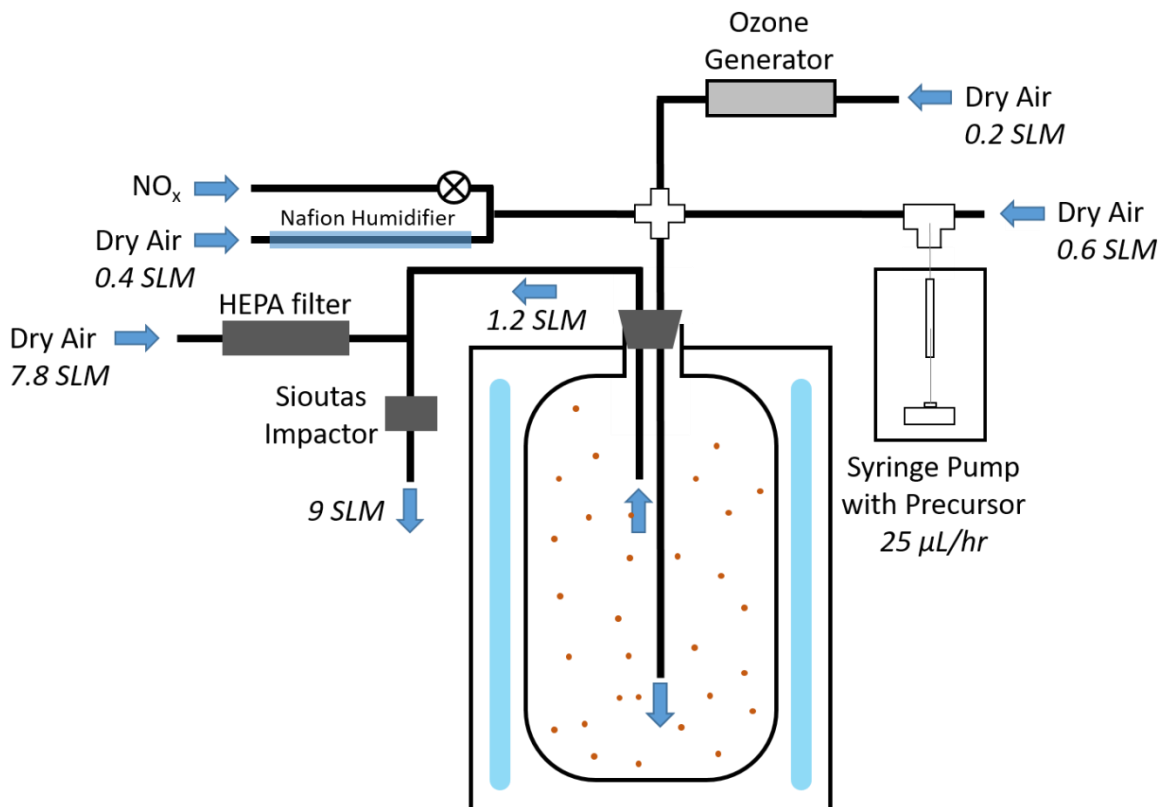


Figure 3.1. Diagram of MAGIC.

Three separate flows are combined inside the reaction vessel. The first is a flow containing ozone, which is produced by flowing dry air through an ozone generator lamp at a flow rate of 0.2 SLM. The second is a flow containing the SOA precursor vapor. The pure VOC liquid is injected via syringe pump into a flow of dry air at a rate of 25 µL/hr. As the precursor is slowly pushed into the air flow, it evaporates and is carried into the main reaction vessel at a flow rate of 0.6 SLM. Finally, the air inside the vessel is humidified by flowing dry air through a Nafion drier/humidifier (PermaPure) at a rate of 0.4 SLM. There is also a port to introduce NO_x to use when performing high NO_x experiments, but the experiments in this

study were performed under low NO_x conditions, so this flow was turned off. For low NO_x experiments, only the three main flows (ozone, precursor, and water vapor) are used. The combined flow through the reaction vessel is 1.2 SLM. This results in a residence time of roughly 7 minutes. When the flows are mixed inside of the reaction vessel, the resulting relative humidity (RH) is around 50%. The estimated steady state concentration of the precursor inside the reaction vessel with the UV lamps turned off is 50 ppm for pure limonene and 80 ppm for pure toluene and the steady state concentration of ozone is about 7.0 ppm. With the UV lamps turned on to generate OH, the steady state concentration of ozone is reduced to about 2.5 ppm

MAGIC has undergone some changes over time, so two sets of conditions were used in this study. Initially, the interior surface of the 8 L reaction vessel was uncoated quartz and the vessel itself was surrounded by 9 UV lamps. This set of conditions will be referred to as “Batch 1” conditions. Later, the quartz reaction vessel was coated with a hydrophobic substance, fluoropel 801A (Cytonix). This coating was originally intended to minimize the loss of NO_y on the walls for high NO_x experiments. Additionally, we found that SOA made with only 2 lamps produced SOA with a slightly higher yield, so we decided to use only 2 UV lamps to reduce the effective oxidative age of SOA. This effect has been previously observed. Lambe *et al.* reported a decrease in SOA yield with higher UV lamp power for isoprene photooxidation SOA in an OFR as well and m-xylene SOA and α-pinene SOA.¹⁵⁰⁻¹⁵¹ For this study, “Batch 2” conditions will refer to experiments performed with the hydrophobic coating on the reaction vessel and 2 UV lamps.

The emission spectrum of these lamps provided in Figure 3.2 shows a large peak at 254 nm, which is responsible for driving the photochemistry within the reactor through the following reactions:



Inside the reaction vessel, the UV light breaks the ozone down into O_2 and O (which includes $O(^3P)$ and $O(^1D)$). Water vapor then reacts with $O(^1D)$ to produce OH , which oxidizes the SOA precursor. Semivolatile organic compounds are produced and the SOA begins to form. The SOA flows out the exit tube, where it can be analyzed by external instrumentation or collected for offline analysis.

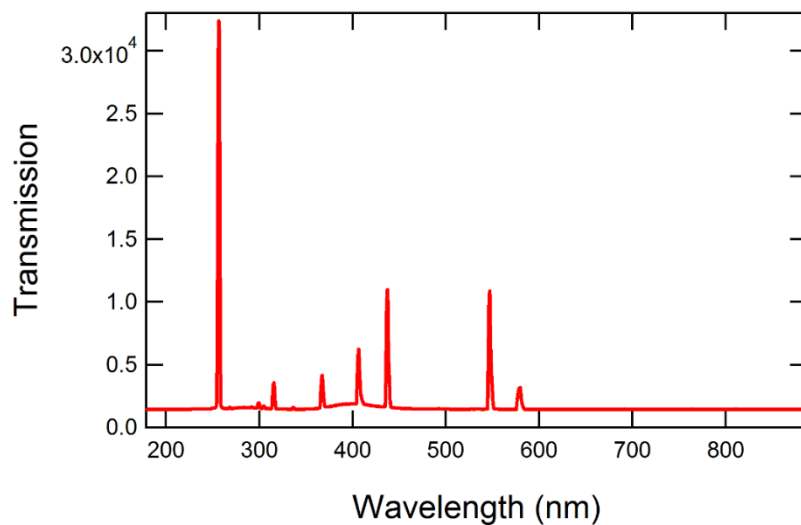


Figure 3.2. Emission spectrum of MAGIC's UV lamps.

A Scanning Mobility Particle Sizer (SMPS) and Aerosol Mass Spectrometry (AMS) were used to characterize three types of SOA made by MAGIC (benzene SOA, toluene SOA, and p-xylene

SOA) upon exiting the reaction vessel. The SMPS data revealed that the mass loading for each type of SOA was around $1 \times 10^4 \mu\text{g}/\text{m}^3$ (or $10 \text{ mg}/\text{m}^3$) with an average geometric mean diameter of 280 nm. The AMS provided further information about the composition of each type of SOA as shown in Figure 3.3. The SOA was characterized under two different sets of conditions in MAGIC. As mentioned above, the first (batch 1) was using an uncoated reaction vessel and 9 UV lamps. The second (batch 2) was using a vessel coated in fluoropel 801A and 2 UV lamps.

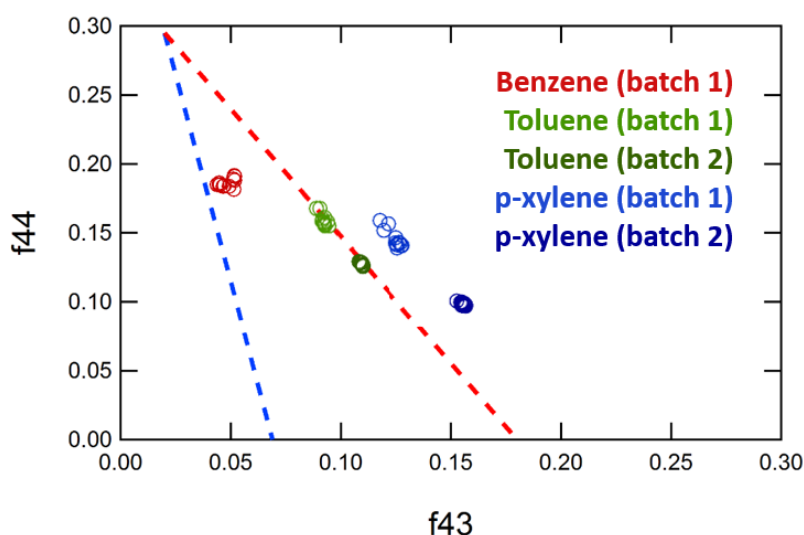


Figure 3.3. Abundance of fragments at m/z 44 as a function of abundance of fragments at m/z 43 (so called “triangular plot”) for benzene, toluene, and p-xylene SOA made by MAGIC. AMS measurements from both batch 1 and batch 2 conditions are shown. The darker colored dots for toluene and p-xylene refer to batch 2.

The AMS data presented in Figure 3.3 plots f_{44} vs f_{43} (where f_{44} is the fractional intensity of ion at m/z 44, corresponding to CO_2^+ , and f_{43} is the fractional intensity of ion at m/z 43, mostly $\text{C}_2\text{H}_3\text{O}^+$). Such f_{43} vs. f_{44} plots are commonly used in the AMS literature to classify aerosols by the extent of their oxidation.¹⁵²⁻¹⁵³ The relative intensity of m/z 44 is representative of the CO_2^+ fragment, which results from the decomposition of organic acids. The m/z 43 fraction is dominated by the $\text{C}_2\text{H}_3\text{O}^+$ fragment, which comes from saturated

carbonyl groups. The triangle formed by the dashed lines indicates the region in which ambient oxidized organic aerosol measurements fall. That is, the triangle region reflects a compilation of experimental field measurements of ambient aerosols. In general, f₄₄ of SOA increases as it becomes more oxidized and more aged. The base of the triangle illustrates that less oxidized SOA are more varied in composition than more oxidized SOA. As SOA ages in the atmosphere, this variety decreases.¹⁵² Figure 3.3 shows that there is a clear distinction between the SOA made from benzene, toluene, and p-xylene. It suggests that benzene SOA is more oxidized than either toluene SOA or p-xylene SOA. It also shows that the second batch of SOA analyzed was less oxidized or aged than batch 1 as a result of reducing the number of UV lamps. This effect was also observed by Lambe *et al.* in two different studies. They generated SOA from a variety of precursors in an OFR at a range of different light intensities. Higher light intensities achieved higher OH exposures. They found that the O:C increased as the OH exposure increased.^{151, 154}

In addition to SMPS and AMS on-line analysis, samples of SOA made by MAGIC were collected and analyzed by ultrahigh-resolution mass spectrometry (FT-ICR-MS) at Pacific Northwest National Laboratory. These samples were made under the same conditions as batch 1 of the AMS results (i.e. uncoated reaction vessel and 9 UV lamps). The mass spectra of each sample (benzene SOM, toluene SOM, and p-xylene SOM) along with the van Krevelen diagram for each sample are shown in Figure 3.4.

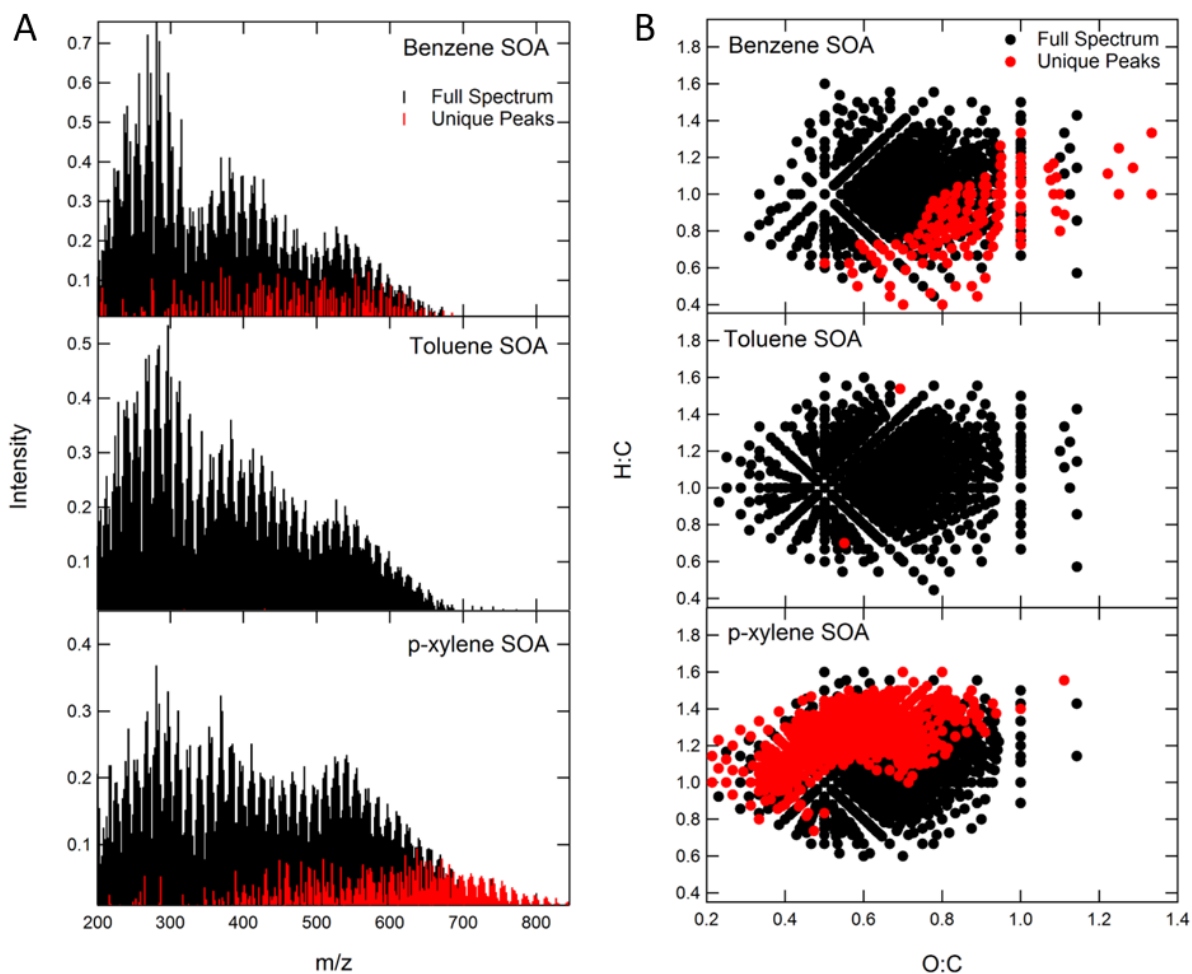


Figure 3.4. A) FT-ICR-MS spectra and B) van Krevelen diagram for benzene SOA (top), toluene SOA (middle) and p-xylene SOA (bottom). Red indicates peaks that were unique to the sample.

The overall mass spectra for all three types of SOA are similar and they have many peaks in common. However, the peaks that are unique to each sample show some key differences. Specifically, the peaks unique to p-xylene SOA have a higher m/z . The van Krevelen plot shows the most important difference. The peaks that are unique to benzene SOA appear to have a much higher O:C than the other two SOA, and the peaks unique to p-xylene SOA have a lower O:C. The average O:C is provided in Table 3.1 below. These FT-ICR-MS results

demonstrate that benzene SOA is the most oxidized of the three, which supports the AMS results.

The average oxygen to carbon ratio of each type of SOA was calculated from both batches of AMS data and the FT-ICR-MS data. This information is shown in Table 3.1 below. All three results indicate that benzene SOA has the highest O:C. It also shows that batch 2, which used 2 UV lamps, had a smaller O:C than Batch 1, which used 9 UV lamps. This suggests that the extra lamps in MAGIC were not necessary for SOA formation, and the extra UV light was further aging the SOA within the reaction vessel, as expected from previous literature on OFRs.^{151, 154}

Table 3.1. Summary of MAGIC oxygen to carbon ratio characterization.

SOA Type	<O>:<C> AMS batch 1	<O>:<C> AMS batch 2	<O>:<C> FT-ICR-MS
Benzene	0.97	N/A	0.73
Toluene	0.87	0.80	0.63
P-xylene	0.80	0.66	0.60

This characterization of MAGIC SOA has shown that MAGIC produces distinct SOA from a variety of precursors.

3.3: EXPERIMENTAL

SOA for these viscosity experiments were made by MAGIC from mixtures of toluene and limonene as described in the previous section. After leaving the reaction vessel, the SOA was impacted onto a 25 mm CaF₂ window with a Sioutas impactor equipped with a single stage D (0.25 μm cut point at 9 SLM collection flow rate) slit. The flow exiting the reaction vessel

was 1.2 SLM. However, the Sioutas impactor is designed to operate at 9 SLM, making it necessary to use make-up dilution air by pulling room air through a HEPA filter. A collection time of 2 hours typically produced about 1 mg of SOM deposited on the window, which corresponds to about 50% collection efficiency for the impactor.

As the SOA was impacted onto the window, it accumulated in a line. Photos of SOM made from mixtures of toluene and limonene in various proportions are given in Figure 3.5. They show visually that as the proportion of toluene in the mixture is increased the resulting SOM seems to become thicker in consistency as well as have a more pronounced color.

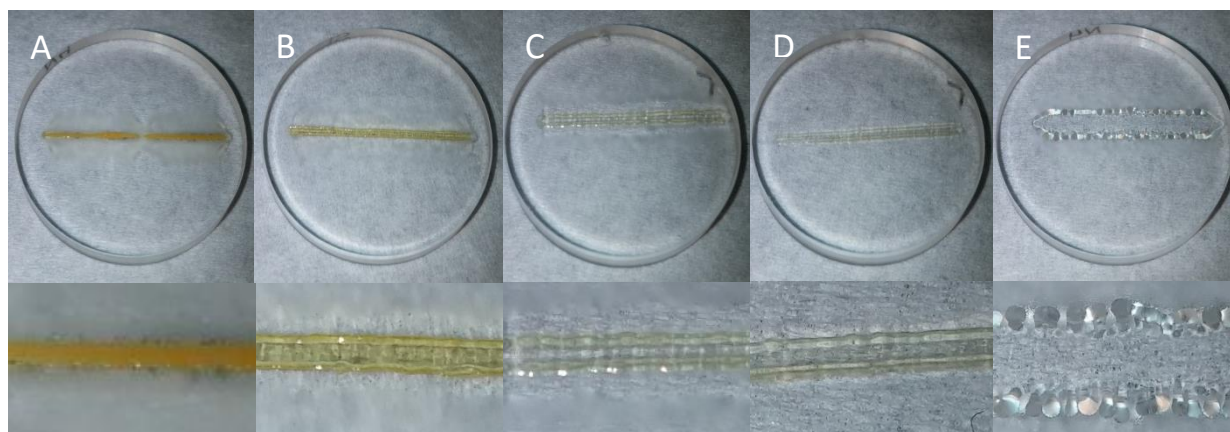


Figure 3.5. SOM after impaction of a) 100% toluene/0% limonene SOA, b) 80% toluene/20% limonene SOA, c) 50% toluene/50% limonene SOA, d) 20% toluene/80% limonene SOA, and e) 0% toluene/100% limonene SOA.

After impaction, the SOM was prepared for photochemistry experiments using the “open-face sandwich” technique described in Chapter 2. No probe molecules were used for these experiments, so a thin film of SOM was created by pipetting 100 μ L of methanol onto the window. This dissolved the SOM and spread the material out evenly across the window. When the methanol evaporated, a thin film of SOM was left behind. After each sample was prepared, it was irradiated inside the SSSS as described in Chapter 2.

Briefly, radiation from a 150 W xenon arc lamp was piped into the SSSS after being reflected by a 280-400 nm dichroic mirror and passed through a 295 nm long-pass filter (Schott WG295) and UV band-pass filter (Schott BG1). This resulted in an irradiation wavelength range of 290-400 nm. As the sample was irradiated, the absorbance was monitored using a custom spectrometer setup. The radiation from a D₂/W light source was piped into the SSSS, across the sample and into the spectrometer using optical fiber cables.

The temperature and RH of the SSSS was not adjusted, meaning room temperature and RH (20 °C and 50% RH) were used for these experiments. The absorption spectra of toluene SOM taken throughout the course of photodegradation are shown in Figure 3.6. The inset displays the decay at 325 nm. This wavelength was used to calculate photodegradation rate constants for each sample, for all proportions of toluene and limonene.

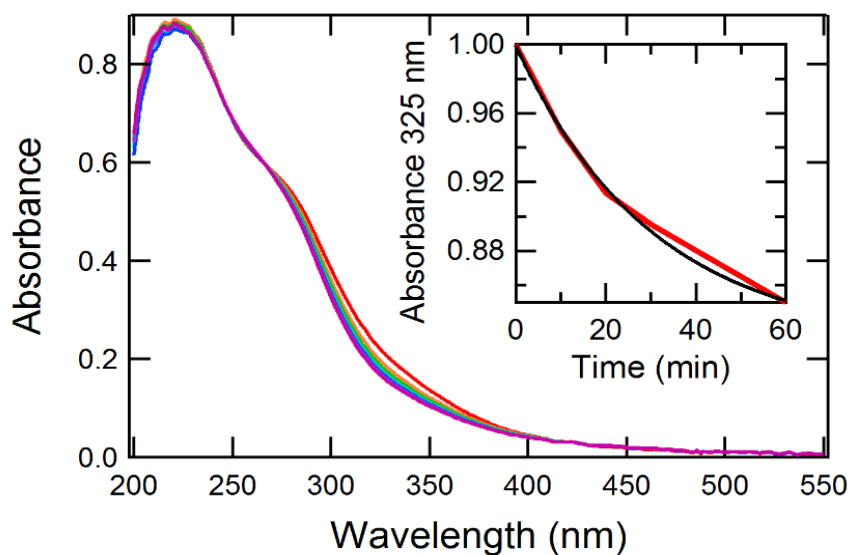


Figure 3.6. Absorption spectra of toluene SOM as a function of irradiation time

3.4: RESULTS AND DISCUSSION

We analyzed the photochemical kinetics of the photodegradation of each sample by plotting the absorbance at 325 nm as a function of irradiation time and fitting that to the exponential decay function in Equation 3.1.

$$A(t) = \text{const}_1 + \text{const}_2 \times e^{-kt} \quad \text{Equation 3.1}$$

The wavelength 325 nm was chosen because that was where the absorbance of the toluene SOA decreased the most during photochemistry. The effective rate constants (k) as a function of toluene percentage in the precursor mixture are plotted in Figure 3.7. One photochemical experiment was performed for each type of sample. However, there is a clear trend. The rate constant was inversely proportional to the percentage of toluene in the precursor mixture.

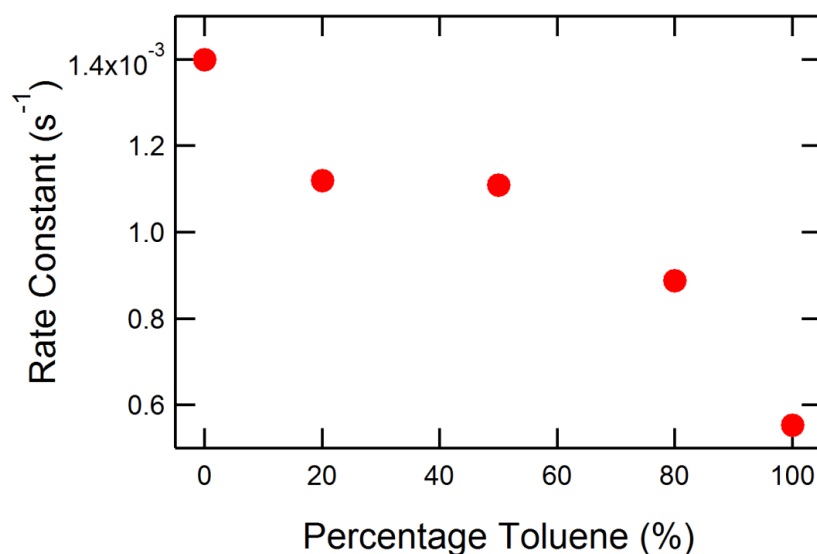


Figure 3.7. Calculated effective rate constants for each sample.

Based on previous viscosity measurements done by the Bertram group, toluene SOM is much more viscous than limonene SOM. Therefore, we expect that the SOM formed from a mixture

of toluene and limonene to fall in between the viscosities of pure toluene SOM and pure limonene SOM. We also expect that as the percentage of toluene in the mixture increased that the viscosity of the resulting SOM would increase.

This was somewhat supported by visual inspection of the impacted SOM (Figure 3.5). SOM made from pure toluene formed a thin line on the CaF₂ window. In contrast, impaction of SOM made from pure limonene resulted in a line, which could be easily deformed under pressure. The limonene SOM material had spread out because it was pushed to the side by the air jet. As the Sioutas impactor collects the SOM, it continues to force air across the CaF₂ window at a rate of 9 SLM. It is possible that both limonene and toluene SOA particles initially land in the center but because the toluene SOM is so viscous, it resists flowing away from the center of the window. However, limonene SOM is less viscous so the air flow causes the SOM to flow slightly away from the center of the window throughout the collection period.

Two SOM samples were sent to the Bertram group at University of British Columbia for poke flow viscosity measurements: one made from 80% toluene/20% limonene and one made from 20% toluene/80% limonene. Poke flow measurements were performed at 50% RH and 30% RH. Estimations for each viscosity were made on the basis that 1 second of poke flow time corresponds to roughly 1000 Pa s. The estimated viscosities for each sample at each RH are shown in Table 3.2.

At 50% RH the viscosity of the 80% toluene sample was more viscous than the 20% toluene sample, but not significantly. This is the RH that was used for the photochemistry experiments. At 30% RH, however, there was an order of magnitude difference in viscosity for these two samples. This may be due to the fact that the viscosity of toluene SOM is much

more sensitive to changes in RH than limonene SOM.^{46, 70} So an 80% toluene SOM sample will change more across a range of RHs than a 20% toluene SOM sample, especially at lower RHs.⁸⁵ This effect is seen in Table 3.2.

Table 3.2. Estimated viscosities of the 20% toluene sample and the 80% toluene sample at 30% RH and 50% RH.

	Estimated Viscosity (Pa·s)	
RH	20% Toluene	80% Toluene
30%	3×10^5	5×10^6
50%	7×10^3	1×10^4

We observed a slight effect on the photochemical kinetics by adjusting the percentage of toluene in the SOM precursor at a RH of 50%. If this photodegradation is truly viscosity controlled, we would expect to see a much stronger effect if we perform these experiments at a lower RH.

3.5: CONCLUSIONS AND FUTURE WORK

This work demonstrated that by mixing two SOA precursors (toluene and limonene) we were able to adjust the viscosity of the resulting SOM by roughly an order of magnitude, depending on RH. Previously we used temperature and/or RH to indirectly control the viscosity of SOM. However, it is difficult to decouple the effects of viscosity on photochemical kinetics from the effects of either temperature or RH. Adjusting the composition of the precursor gives us a more direct method of controlling viscosity of SOM. However, these experiments came with their own set of complications.

It would have been ideal to use a probe molecule, as we had done in previous studies. However, toluene SOM generated by MAGIC absorbed significantly below 400 nm. Therefore, any probe molecule used would have to absorb at wavelengths above 400 nm, where there would be no interference with the matrix. This stipulation added to the requirements that a probe molecule would need to fulfill. It needed to be atmospherically relevant and photodegrade at atmospherically relevant wavelengths. However, finding a molecule that fit these requirements proved to be a challenge. We decided to use the photodegradation of SOM itself for the preliminary experiments reported here.

In these preliminary experiments, we found that as the viscosity of the SOM was increased by raising the ratio of toluene to limonene in the precursor mixture, the photodegradation of the SOM slowed down. This is a promising result, but clearly there is more work to be done for this study. First, these photochemistry experiments should be performed at a few different RHs, especially at lower RHs, where the difference in sample viscosities is larger. Additionally, it would be beneficial to know how the molecules in each sample compare. Are the molecules in the 20% toluene sample the same as the molecules in the 80% toluene sample, perhaps in different proportions? Or are they completely different molecules? To answer these questions, it would be useful to analyze each sample (0% toluene, 20% toluene, 50% toluene, 80% toluene, and 100% toluene) by mass spectrometry.

CHAPTER 4

EFFECT OF RELATIVE HUMIDITY ON THE FORMATION AND COMPOSITION OF TOLUENE SOA

Portions of this chapter are reproduced with permission from: Hinks, M. L., Montoya, J., Ellison, L., Lin, P., Laskin, J., Laskin, A., Shiraiwa, M., Dabdub, D., Nizkorodov, S. A., Effect of Relative Humidity on the Yield and Composition of Secondary Organic Aerosol from Oxidation of Toluene, *Submitted Environmental Science and Technology*, **2017**

4.1: INTRODUCTION

Secondary organic aerosol (SOA) is an important component of atmospheric particulate matter. It is formed in the atmosphere via oxidation of volatile organic compounds (VOCs) by common atmospheric oxidants such as O_3 , OH , and NO_3 .¹⁵⁵ The SOA formation mechanisms depend in a complex way on environmental parameters such as solar irradiance, temperature, and relative humidity (RH). The RH effects have multiple aspects: (a) Gaseous water can directly participate in the VOC oxidation reactions. For example, water is well known to react with carbonyl oxide intermediates in ozonolysis of alkenes;⁹⁰ (b) Aerosol liquid water present in hygroscopic particles can lead to hydrolysis of organic compounds and other particle-phase reactions involving or catalyzed by water;⁹¹ (c) aerosol liquid water has a strong effect on acidity of particles and, therefore, affects acid-catalyzed processes occurring in particles;⁹² (d) Water can act as a plasticizer for SOA particles making them less viscous, thus affecting the rate of their growth;^{60, 63, 156} (e) Finally, under supersaturated conditions, aqueous chemistry occurring in cloud and fog droplets promotes photolysis driven conversion of small water-soluble molecules into non-volatile products that would not form in the absence of liquid water,²⁴ as well as photodegradation of dissolved SOA compounds.^{39, 54, 93-94} Water is ubiquitous in the atmosphere, and therefore, it is important to understand how it affects formation processes, chemical composition, and physical properties of SOA.

The amount of SOA that is produced from a given VOC is often expressed in the form of fractional SOA yield (Y),²²

$$Y = \frac{\Delta SOA}{\Delta VOC} \quad \text{Equation 4.1}$$

where ΔSOA represents the increase in the organic aerosol mass concentration produced when the concentration of VOC is reduced by ΔVOC . Due to the multiple effects of RH on the SOA formation mechanism, the SOA yield could potentially either increase with RH (positive correlation) or decrease with RH (negative correlation). A summary of the studies studying the effect of RH on SOA yield is given in Table 4.1.

Table 4.1. Examples of previous studies of the effect of RH on SOA yield.

Reference	Precursor	O ₃	OH	NO _x	Seeds	[Precursor]	Yield Effect
Walser <i>et al.</i> (2007) ⁵⁵	Limonene	Y				8 ppm	Positive
Yu <i>et al.</i> (2011) ¹⁵⁷	Limonene	Y				350 ppb	Positive
Saathoff <i>et al.</i> (2009) ¹⁵⁸	Limonene, α -pinene	Y				16-50 ppb	Positive
Jonsson <i>et al.</i> (2006) ¹⁵⁹	Limonene, α -pinene, carene	Y				15, 30 ppb	Positive
Jonsson <i>et al.</i> (2008) ¹⁶⁰	Limonene, α -pinene, carene	Y				7 ppb	Positive
Czoschke <i>et al.</i> (2006) ¹⁶¹	α -pinene	Y			Y	150 ppb	Negative
Czoschke <i>et al.</i> (2003) ¹⁶²	α -pinene	Y			Y	0.7, 1.2 ppm	Negative
Chu <i>et al.</i> (2016) ¹⁶³	α -pinene		Y/N ^a	Y	Y/N	200 - 300 ppb	Positive and Negative
Cocker <i>et al.</i> (2001) ¹⁶⁴	α -pinene	Y			Y/N	150 ppb	None
Kristensen <i>et al.</i> (2001) ¹⁶⁵	α -pinene	Y	Y	Y	Y	20 ppb	None

Bonn et al. (2002) ¹⁶⁶	Monoterpenes	Y				1 ppm	Negative
Emanuelsson et al. (2013) ¹⁶⁷	β -pinene	Y				79, 109, 164 ppb	Negative
Fry et al. (2009) ¹⁶⁸	β -pinene			Y		15 ppb	None
Boyd et al. (2015) ¹⁶⁹	β -pinene	Y	Y	Y	Y	7 - 17 ppb	None
Riva et al. (2016) ¹⁷⁰	ISOPOOH	Y	Y		Y	50, 300 ppb	Slight Positive
Zhang et al. (2011) ¹⁷¹	Isoprene			Y	Y	400, 800 ppb	Negative
Dommen et al. (2006) ¹⁷²	Isoprene			Y		180 - 2500 ppb	None
Nguyen et al. (2011) ¹⁷³	Isoprene		Y	Y		250 ppb	None
Lewandowski et al. (2015) ¹⁷⁴	isoprene, 1,3-butadiene			Y	Y	7 ppm	Negative
Harvey et al. (2016) ¹⁷⁵	3-hydroxypropanal	Y				-	Negative
Kamens et al. (2011) ¹⁷⁶	Toluene			Y	Y	1 ppm	Positive
Cao et al. (2010) ¹⁷⁷	Toluene		Y	Y/N	Y	100, 300 ppb	Negative
Zhou et al. (2011) ¹⁷⁸	Toluene, xylene			Y	Y/N	125 ppb	Positive
Cocker et al. (2001) ¹⁷⁹	Xylene, trimethylbenzene			Y	Y/N	230 ppb, 400 ppb	None
This work	Toluene		Y	Y/N		300 ppb, 1 ppm	Negative

^aY/N indicates that both conditions were used in the study.

Biogenic VOCs such as limonene, α -pinene, and isoprene are the most studied SOA precursors in terms of the RH effects. The most consistent results have been obtained by several research groups for SOA produced by limonene ozonolysis (without seed particles) over a range of limonene concentrations from 7 ppb to 8 ppm.^{55, 157-160} In all the studies, a positive correlation between RH and SOA yield was reported,^{55, 157-160} which is likely

attributed to the fact that reactions of water with carbonyl oxide intermediates of limonene ozonolysis produce more oxygenated and lower volatility compounds than those produced under dry conditions.

SOA from α -pinene ozonolysis has been studied both with and without seed particles for a range of α -pinene concentrations from 20 ppb to 1.2 ppm. Some studies reported a positive correlation between RH and SOA yield,¹⁵⁸⁻¹⁶⁰ whereas others reported no effect,¹⁶⁴⁻¹⁶⁵ and some reported a negative correlation.^{161-162, 166} The disparity in these results is most likely due to variability in concentrations and seed particle effects. Studies that used lower concentrations of α -pinene (< 150 ppb) generally reported negative correlations,^{161-162, 166} while studies that used higher concentrations (> 150 ppb) of α -pinene observed positive relationships.¹⁵⁸⁻¹⁶⁰ However, this trend could also correspond to the use of seed particles. Chu *et al.* investigated the effect of RH on the yield of α -pinene produced under high NO_x conditions and observed a positive correlation when ammonium sulfate seed particles were used and a negative correlation using iron sulfate seed particles.¹⁶³ They found that SOA formed in presence of the iron sulfate seeds at higher RH contained a lower organic mass with more oxygenated products. Their result suggested that SOA products are fragmenting on the iron sulfate seed particles to yield more volatile molecules, thus reducing the SOA mass.

Bonn *et al.* studied the effect of humidity on SOA produced by ozonolysis of exocyclic and endocyclic monoterpenes.¹⁶⁶ They reported a negative correlation between RH and SOA yield and noted that this effect was more pronounced for exocyclic monoterpenes such as α -pinene than endocyclic monoterpenes such as β -pinene. This result is consistent with a

decrease in α -pinene SOA yield at higher RH reported by Emanuelsson *et al.*¹⁶⁷ However, other studies of Fry *et al.* and Boyd *et al.* did not observe changes in α -pinene SOA yield at a variety of RHs.¹⁶⁸⁻¹⁶⁹

For isoprene SOA, the results appear to be more consistent. Zhang *et al.* and Lewandowski *et al.* both investigated the yield of isoprene SOA made in the presence of seed particles and observed a negative correlation between RH and SOA yield.^{171, 174} Dommen *et al.* performed similar experiments in the absence of seed particles and reported that increasing RH had no effect on the SOA yield but had some effect on the evolution of SOA volatility. Over the RH range studied, both dry and humidified samples increased in volatility over time, but the process was more pronounced under dry conditions.¹⁷²

Chemical composition of SOA is just as important as its yield because it determines their climate and health relevant properties. Nguyen *et al.* performed ESI-HRMS on isoprene SOA formed under high and low RH conditions and found that the high RH samples contained fewer high molecular weight oligomers than the low RH samples.¹⁷³ Similarly, Zhang *et al.* investigated the effect of RH on the composition of isoprene SOA and found that oligoesters present in the SOA were suppressed at higher RH, while the formation of organosulfates was enhanced.¹⁷¹ Comparable results were observed in other similar systems. For example, Riva *et al.* studied the effect of RH on SOA made from oxidized isoprene hydroxy hydroperoxide (ISOPOOH) and found that increasing RH led to an increase in abundance of some oligomers while decreasing the abundance of other oligomers.¹⁷⁰ Harvey *et al.* investigated the effect of RH on 3-hydroxypropanal ozonolysis SOA and found that increasing RH resulted in a decrease in SOA yield and a decrease in oligomerization.¹⁷⁵

The effect of RH on anthropogenic SOA, including SOA formed from toluene, m-xylene, and 1,3,5-trimethylbenzene (TMB) has also been studied, albeit in less depth. Two studies have been performed on m-xylene SOA. Zhou *et al.* found that increasing RH increased SOA yield, while Cocker *et al.* observed no RH effect on m-xylene SOA yield.¹⁷⁸⁻¹⁷⁹ Cocker *et al.* also reported similar results for TMB. These experiments were all performed under high NO_x conditions. Toluene SOA made under high NO_x conditions has been found to either have a positive correlation between RH and SOA yield or no effect.¹⁷⁶⁻¹⁷⁸ Toluene SOA made under low NO_x conditions has only been investigated by Cao *et al.*, who observed a negative correlation between RH and SOA yield.¹⁷⁷ Thus far, the effect of RH on toluene SOA chemical composition has not been studied. In this work, we investigate the effect of RH on both toluene SOA yield and composition to better understand how the two are related. We observe an unusually strong RH dependence of the yield and composition of low-NO_x SOA from toluene, and we attribute it to the more extensive oligomerization of SOA compounds under dry conditions. These findings have important implications for toluene SOA concentrations in dry, urban areas, especially in areas where regulations aim to reduce NO_x emissions in the future.

4.2: EXPERIMENTAL

Toluene SOA was made at RHs ranging from 0% RH to 90% RH. Particle concentrations for each experiment were monitored with a Scanning Mobility Particle Sizer (SMPS Model 3080, TSI Inc.), while the temperature (± 1 °C) and RH ($\pm 2\%$ RH) were monitored with a Vaisala HMT330 probe. A Proton Transfer Reaction Time-of-Flight Mass Spectrometer (PTR-ToF-MS, IONICON) was used to measure toluene concentrations throughout each experiment.

Before each experiment, the chamber was humidified to the desired RH by flowing purified air (typical VOC mixing ratios below 1 ppb) through a Nafion humidifier (PermaPure). Hydrogen peroxide (H_2O_2) was introduced to the chamber by injecting a measured volume of aqueous H_2O_2 (30 wt%) into a bulb where it was evaporated and carried into the chamber by a flow of purified air over a period of 30 minutes. Next, toluene (Fisher Scientific, ACS grade) was introduced into the chamber in a similar manner, by evaporating a measured volume of liquid toluene into a stream of air over a period of five minutes. Most of the experiments were performed with 1000 ppb toluene to collect a sufficient amount of SOA for offline analysis. Lower concentration experiments with 300 ppb toluene were performed to test the concentration effects. The ratio of toluene to H_2O_2 was kept constant for both types of experiments; H_2O_2 concentration was 2000 ppb and 600 ppb in high toluene and low toluene experiments, respectively.

In the high NO_x experiments, gaseous NO (1000 ppm in N_2) was added to the chamber over a period of 3 minutes at a flow rate of 100 sccm to achieve a total NO concentration of 300 ppb (for the low NO_x experiments this step was skipped). After adding all the chemicals to the chamber, they were mixed with a fan. Then, the UV lights were turned on, producing OH from the H_2O_2 and initiating the photooxidation of toluene. The amount of SOA was monitored with the SMPS. No drier was used between the chamber and SMPS. The sheath flow of the SMPS was recirculated to have similar RH to the chamber air. The SMPS data was corrected for particle wall loss effects assuming an effective first-order rate constant for the loss of mass concentration of $9.3 \times 10^{-4} \text{ min}^{-1}$ measured in a separate experiment (the rate constant was assumed to be independent of particle size).

In selected high RH (75% RH) and low RH (0% RH) experiments, SOA samples were collected onto Teflon filters for offline analysis by nanospray desorption electrospray ionization high-resolution mass spectrometry (nano-DESI-HRMS). The SOA filter samples were analyzed in both positive and negative ion modes using an LTQ-Orbitrap mass spectrometer (Thermo Corp.) with a resolving power of 10^5 at m/z 400 equipped with a custom-built nano-DESI source.¹⁸⁰⁻¹⁸¹ Mass spectra of solvents and blank filters were recorded as controls. Mass spectra of related samples were clustered together, and the m/z axis was calibrated internally with respect to known SOA products. The peaks were assigned formulas, $C_cH_hO_oN_nNa_{0-1}^+$ or $C_cH_hO_oN_n^-$, constrained by valence rules and elemental ratios (c,h,o,n refer to the number of corresponding atoms in the ion).¹⁸² The resulting ion formulas were converted into molecular formulas of the corresponding neutral species. All data reported below refers to the formula and molecular weights of the neutral species.

4.3: RESULTS AND DISCUSSION

A summary of all the experiments performed in this study, along with the conditions used in each, is presented in Table 4.2. Additionally, representative examples of the wall loss corrected particle mass concentration obtained from SMPS data are shown in Figure 4.1 as a function of photooxidation reaction time for both the low NO_x and the high NO_x toluene SOA systems.

Table 4.2. Summary of experiments. ^a

Sample ID	Initial RH	NO _x ppm	Toluene ppm	H ₂ O ₂ ppm	SOA from SMPS μg/m ³	Wall Loss Corrected SOA μg/m ³	Yield	<i>Y_{RH}/Y_{dry}</i>
Low NO_x - High Toluene								
LN-HT-0712	0	-	1.0	2.0	203	232	0.16	1.00
LN-HT-0523	0	-	1.0	2.0	187	217	0.15	
LN-HT-0901	0	-	1.0	2.0	175	212	0.15	
LN-HT-0519	0	-	1.0	2.0	160	182	0.13	
LN-HT-0615	18	-	1.0	2.0	78.5	91.6	0.065	0.42
LN-HT-0614	22	-	1.0	2.0	72.5	82.6	0.058	
LN-HT-0528	43	-	1.0	2.0	73.8	83.5	0.059	0.40
LN-HT-0831	74	-	1.0	2.0	36.0	38.1	0.026	0.13
LN-HT-0711	75	-	1.0	2.0	25.8	27.1	0.019	
LN-HT-0524	76	-	1.0	2.0	19.6	20.5	0.015	
LN-HT-0520	77	-	1.0	2.0	25.0	27.5	0.019	
LN-HT-0604	88	-	1.0	2.0	18.6	19.2	0.014	0.13
LN-HT-0526	89	-	1.0	2.0	30.5	32.0	0.023	
Low NO_x - Lower Toluene								
LN-LT-1006	0	-	0.3	0.6	22.4	26.9	0.055	1.00
LN-LT-1007	75	-	0.3	0.6	7.9	8.7	0.022	0.40
High NO_x - High Toluene								
HN-HT-0621	0	0.3	1.0	2.0	330	389	0.27	1.00
HN-HT-0715	43	0.3	1.0	2.0	209	256	0.18	0.66
HN-HT-0622	77	0.3	1.0	2.0	227	268	0.19	0.70

^a The Sample ID uses LN to refer to low NO_x, HN to refer to high NO_x, HT to refer to high toluene, and LT to refer to lower toluene, as well as the experiment date in the form of MMDD.

Under high NO_x conditions there was a small difference in the maximum mass concentration achieved under 0%, 40%, and 75% RH (less than a factor of 2), but under low NO_x conditions there was a clear and significant difference. For the low NO_x system, the wall loss corrected particle mass concentration decreased by a factor of 8 over the range of RHs studied. The effect was reproducible as essentially the same mass concentration was observed in experiments repeated on different days under the same initial conditions.

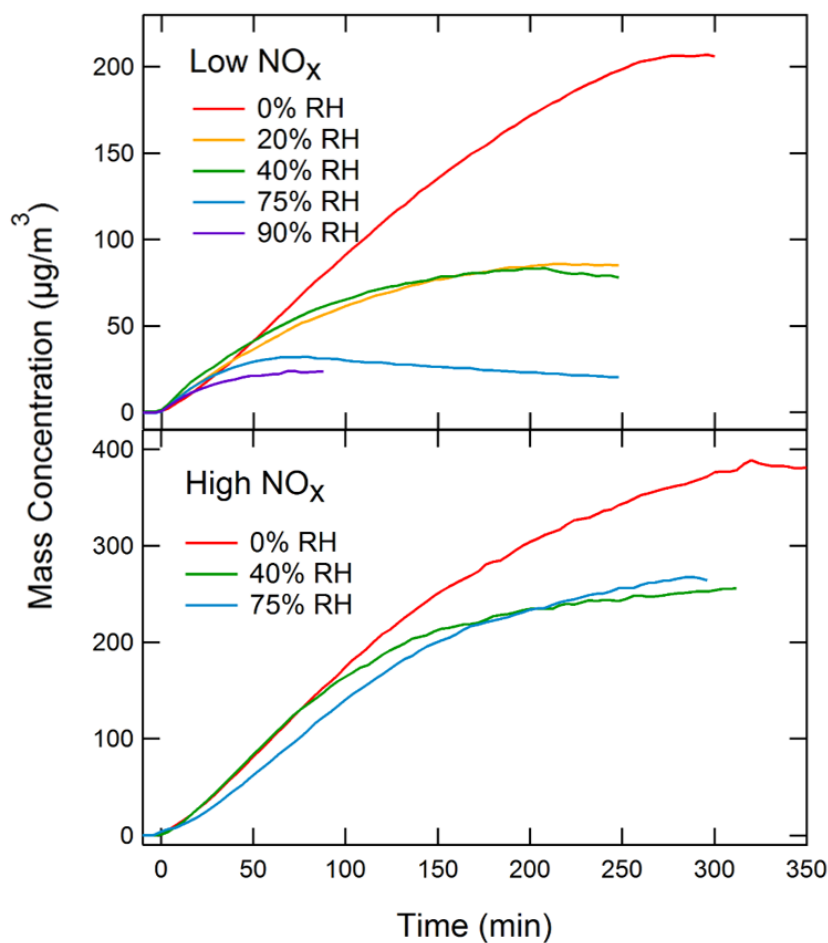


Figure 4.1. Examples of particle mass concentration measurements by SMPS (corrected for wall-loss) as a function of photooxidation time under low-NO_x (top) and high-NO_x (bottom) conditions.

For each experiment, the aerosol yield was calculated using Equation 3.1. Δ SOA was determined from the SMPS data assuming a previously measured density of toluene SOA of 1.4 g/cm^3 .¹⁸³ We applied wall-loss correction to the Δ SOA data as described in the experimental section. Δ VOC was calculated from the known initial concentration of toluene in the chamber and from the relative change in the PTR-ToF-MS signal of toluene after 6 hours of photooxidation. Because of the high concentrations of toluene used in most experiments, the toluene signal was tracked through its ^{13}C peak to avoid issues with ^{12}C peak distortion. Δ VOC was assumed to be the same for experiments performed under the same conditions and was held constant for each yield calculation. This assumption was tested using PTR-ToF-MS data for samples LN-LT-1006 and LN-LT-1007. Over a 6-hour long experiment under 0% RH the PTR-ToF-MS toluene signal decreased to 57% of its original signal and under 75% RH, the toluene signal decreased to 64% of its original signal. These values are the same within the typical uncertainty of PTR-ToF-MS measurements indicating that the amount of toluene reacted during an experiment is comparable across RHs.

Under low NO_x conditions, the toluene SOA yield was found to decrease by approximately an order of magnitude over the range of RH studied in this work, from 0.15 ± 0.02 at 0% RH to 0.020 ± 0.005 at 75%-90% RH. In contrast, the toluene SOA yield under high NO_x conditions did not change as much. The average yield of the high NO_x experiments was 0.27 at 0% RH and 0.19 at 75% RH. Since the low- NO_x experiments revealed an unusually strong RH dependence of the aerosol yield, we also measured the yield for the SOA formation through dark reaction of 500 ppb of limonene with 1000 ppb of ozone. The limonene SOA control tests demonstrated a slight increase of the SOA yield on RH, in agreement with the previous studies.^{55, 157-160}

To allow for an easier comparison across different experiment types, we use a ratio of yields (Y_{RH}/Y_{dry}), where Y_{RH} is the average yield in experiments at specific RH and Y_{dry} is the average yield at dry conditions (0% RH). Figure 4.2 plots Y_{RH}/Y_{dry} as a function of RH for the low and high NO_x experiments that were performed using 1.0 ppm of toluene. At this toluene concentration, the Y_{RH}/Y_{dry} for the low NO_x system was found to decrease from 1.0 at 0% RH to 0.13 at 75% RH, representing a decrease by a factor of almost 10. Using a toluene concentration of 300 ppb, the change for the low NO_x system was smaller, but still significant. The Y_{RH}/Y_{dry} was 1.0 at 0% RH and 0.4 at 75% RH. However, in the high NO_x system, where a toluene concentration of 1.0 ppm was used, there was much weaker trend in the yields as a function of RH, with the Y_{RH}/Y_{dry} decreasing from 1.00 to 0.70 from 0 to 75% RH.

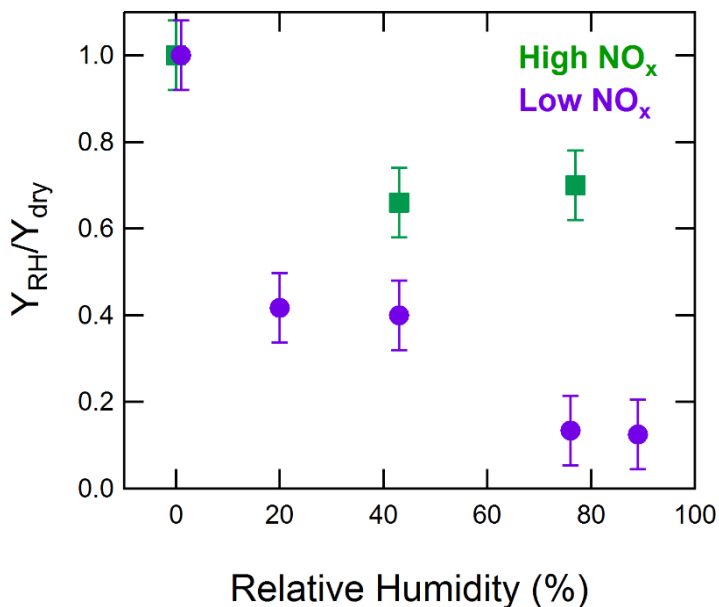


Figure 4.2. Y_{RH}/Y_{dry} for the Low NO_x – high toluene system and the high NO_x – high toluene system. Error bars for each data point reflect the standard deviation of the low NO_x – high toluene system at 0% RH.

The differences in yields between the low and high RH systems cannot be explained by hygroscopic growth of particles at elevated RH. Throughout the experiment, the SMPS

sampled air directly from the chamber. Each experiment lasted many hours, which allowed the sheath flow in the SMPS to approach the RH of the chamber air. Therefore, the particles sized by the SMPS contained some aerosol liquid water and would appear larger than their dry size. If the organic mass in particles did not change at different RH levels, we would have observed an *increase* as opposed to a decrease in the measured particle mass concentration. With a typical hygroscopic growth factor (the ratio of particle diameters in the humidified and dry air) for SOA of 1.1 at 85% RH,¹⁸⁴ the increase in the apparent mass concentration would have been by a factor of about 1.3. Instead, the mass concentration decreased by almost a factor of 10 at higher RHs.

The chamber experiments are known to be affected by the irreversible wall loss of particles as well as reversible partitioning of semivolatile compounds on the walls.¹⁸⁵⁻¹⁸⁷ While we correct our data for the particle wall loss, we can only estimate what effect the loss of volatile compounds has on the apparent yields. If the loss of semivolatiles increased with RH in this chamber, we would have observed suppression in the yield of limonene ozonolysis SOA in our control experiments. However, the yield of limonene ozonolysis SOA was not strongly affected by RH. By the same logic, the loss of semivolatiles should have been comparable for high NO_x and low NO_x toluene SOA, however, the SOA yield reduction was much larger in the latter case. Therefore, we do not think that the RH-dependent wall loss of semivolatiles is solely responsible for these observations. The dramatic dependence of the low NO_x toluene SOA yield on RH is therefore a real effect, and not an artifact of the measurements. It is also consistent with results of Cao *et al.*, who observed a negative correlation between RH and low NO_x toluene SOA yield, but no correlation between RH and high NO_x toluene SOA yield.¹⁷⁷

The most likely explanation for the observed RH effect is that there are chemical reactions in the system that directly involve water and change the chemical composition of the particles thereby affecting their growth rate. Previous studies have shown that RH can affect the composition and potential yield of SOA by altering the fraction of low-volatility oligomers in SOA. Increased RH could potentially suppress oligomerization occurring by condensation reactions by shifting the reaction equilibrium toward the products as discussed in Nguyen *et al.*¹⁷³ In order to test this hypothesis, samples were analyzed using both negative and positive ion mode nano-DESI-HRMS. The raw mass spectra of a low RH sample and a high RH sample are shown in Figure 4.3, plotted as a function of the molecular weight of the neutral compound. The mass spectra obtained in the positive and negative ion modes represent the compounds ionizable in these modes, and are not expected to be identical.¹⁸⁸

The low-NO_x mass spectrum shown in Figure 4.3 is qualitatively similar to the low-NO_x mass spectrum of toluene SOA discussed in Lin *et al.*, which was prepared in a different smog chamber but analyzed by the same nano-DESI instrument.¹⁸⁹ As shown in Figure 4.3, the increase in RH resulted in a visible reduction in the overall peak abundance for both ion modes, most likely due to the reduction in particle mass at high RH. However, the major observed SOA compounds remained approximately the same. Table 4.3 reports five most abundant peaks for both the low and high RH samples observed in positive and negative modes. The fact that the major peaks are so similar between the low and high RH samples suggests that, although the aerosol yield decreases, the mechanism of formation of the major products remains roughly the same.

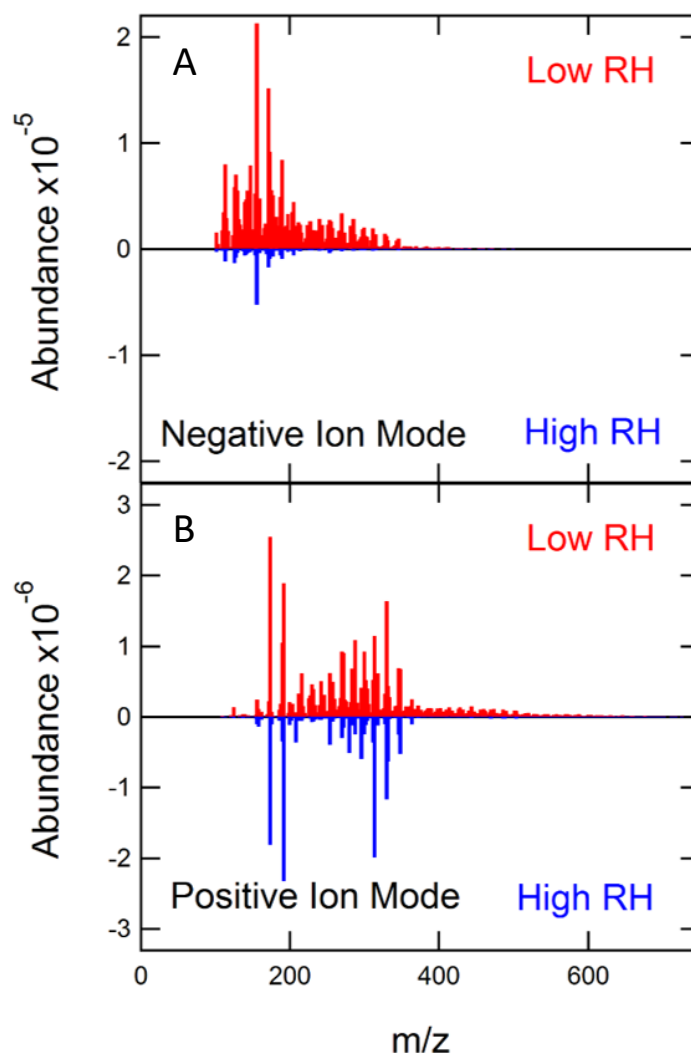


Figure 4.3. High-resolution mass spectra obtained in negative ion mode (A) and positive ion mode (B). The red upward-pointing mass spectra represent the samples made under low RH (LN-HT-0712) and the blue inverted mass spectra represent the samples made under high RH (LN-HT-0711).

While the major oxidation products were largely the same at low and high RH, the less abundant products were affected by RH much stronger. Specifically, the abundances of high-molecular weight compounds were visibly reduced at high RH, suggesting that the oligomer formation is suppressed at high RH conditions (Figure 4.3). To better quantify this effect, Figure 4.4 shows the combined peak abundances as a function of the number of carbons in

each molecule. Monomer compounds containing 7 carbon atoms and dimer compounds containing 14 carbon atoms clearly dominate the distribution. Many other compounds with carbon numbers up to 32 also appear in the mass spectrum, and these minor compounds appear to be the most affected by RH.

Table 4.3. Most abundant compounds observed in the low and high RH samples. ^a

Positive Ion Mode		Normalized Peak Abundance	
Nominal Mass	Formula	Low RH	High RH
174	C ₇ H ₁₀ O ₅	1	1
192	C ₇ H ₁₂ O ₆	0.74	0.86
330	C ₁₄ H ₁₈ O ₉	0.64	0.78
314	C ₁₄ H ₁₈ O ₈	0.45	0.50
288	C ₁₂ H ₁₆ O ₈	0.43	0.11
332	C ₁₄ H ₂₀ O ₉	0.17	0.27
Negative Ion Mode		Normalized Peak Abundance	
Nominal Mass	Formula	Low RH	High RH
156	C ₇ H ₈ O ₄	1	1
172	C ₇ H ₈ O ₅	0.71	0.86
174	C ₇ H ₁₀ O ₅	0.43	0.78
190	C ₇ H ₁₀ O ₆	0.40	0.50
114	C ₅ H ₆ O ₃	0.38	0.27

^a Five most abundant peaks observed in each spectrum. In negative ion mode, the same most abundant peaks were observed at the low and high RH. In positive ion mode, the most abundant species differed by one compound in the low and high RH experiments, hence the table contains 6 formulas.

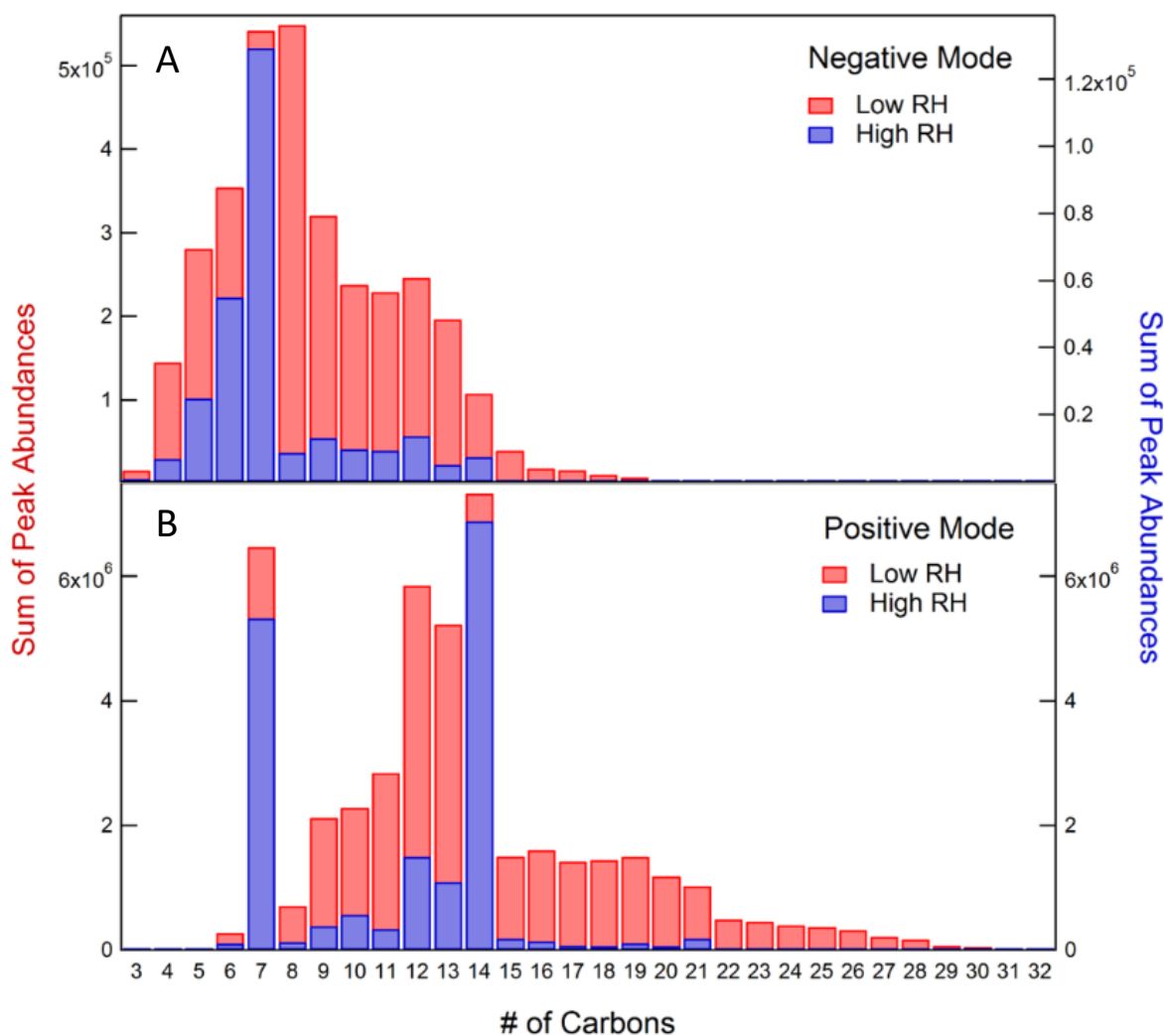


Figure 4.4. Combined abundance of all peaks as a function of number of carbon atoms in negative mode (A) and positive mode (B). The data for the low RH sample (LN-HT-0712) are shown in red and the data for the high RH sample (LN-HT-0711) are shown in blue.

When comparing the low RH sample to the high RH sample, there is a significant decrease in combined peak abundance for molecules with more than 7 carbons under high RH conditions. This suggests that the abundance of dimers and trimers decreases with an increase in RH. Because these higher molecular weight oligomers tend to have lower volatility,¹⁹⁰ they play an important role in the formation and growth of aerosol particles.

With the lower fraction of oligomers produced under high RH conditions, the population of the oxidation products becomes more volatile on average, resulting in a lower SOA yield.

To better illustrate the effect of RH on the yield of condensable oxidation products, the volatility distributions were estimated for the low-NO_x toluene SOA compounds using the “molecular corridor” approach.¹⁹⁰⁻¹⁹¹ This parameterization was developed specifically for atmospheric organic compounds containing oxygen, nitrogen, and sulfur,¹⁹⁰ and it makes it possible to estimate the pure compound vapor pressure, C_0 , from the elemental composition derived from high-resolution mass spectra.^{54, 192} C_0 is related to the more commonly used effective saturation mass concentration, $C^* = \gamma \times C_0$, where γ is the activity coefficient.^{21, 193} C_0 becomes equal to C^* under the assumption of an ideal thermodynamic mixing. The C_0 values were calculated for each compound observed in the positive and negative ion mode mass spectra. The values were binned as commonly done in the volatility basis set (VBS)¹⁹⁴ in equally spaced bins of base-10 logarithm of C_0 . The contribution of each compound to its volatility bin was taken to be proportional to its relative abundance in the mass spectrum. Because of the approximate correlation between the ESI detection sensitivity and molecular weight,¹²² the mass fraction of the detected SOA compound can be taken to be proportional to its peak abundance. This is an approximation, but it is suitable for comparing distributions for SOA produced and analyzed under the same experimental conditions.⁵⁴

Figure 4.5 shows the resulting distribution of the SOA compounds by volatility. Under typical ambient conditions, compounds with C_0 above $\sim 10 \mu\text{g m}^{-3}$ (falling above the $\log(C_0) = 1$ bin) are more likely to be found in the gaseous phase. Some of these more volatile compounds were detected in the negative ion mode. They may correspond to carboxylic acids that

adsorbed to the filter during sampling. Less volatile compounds were preferentially observed in the positive ion mode.

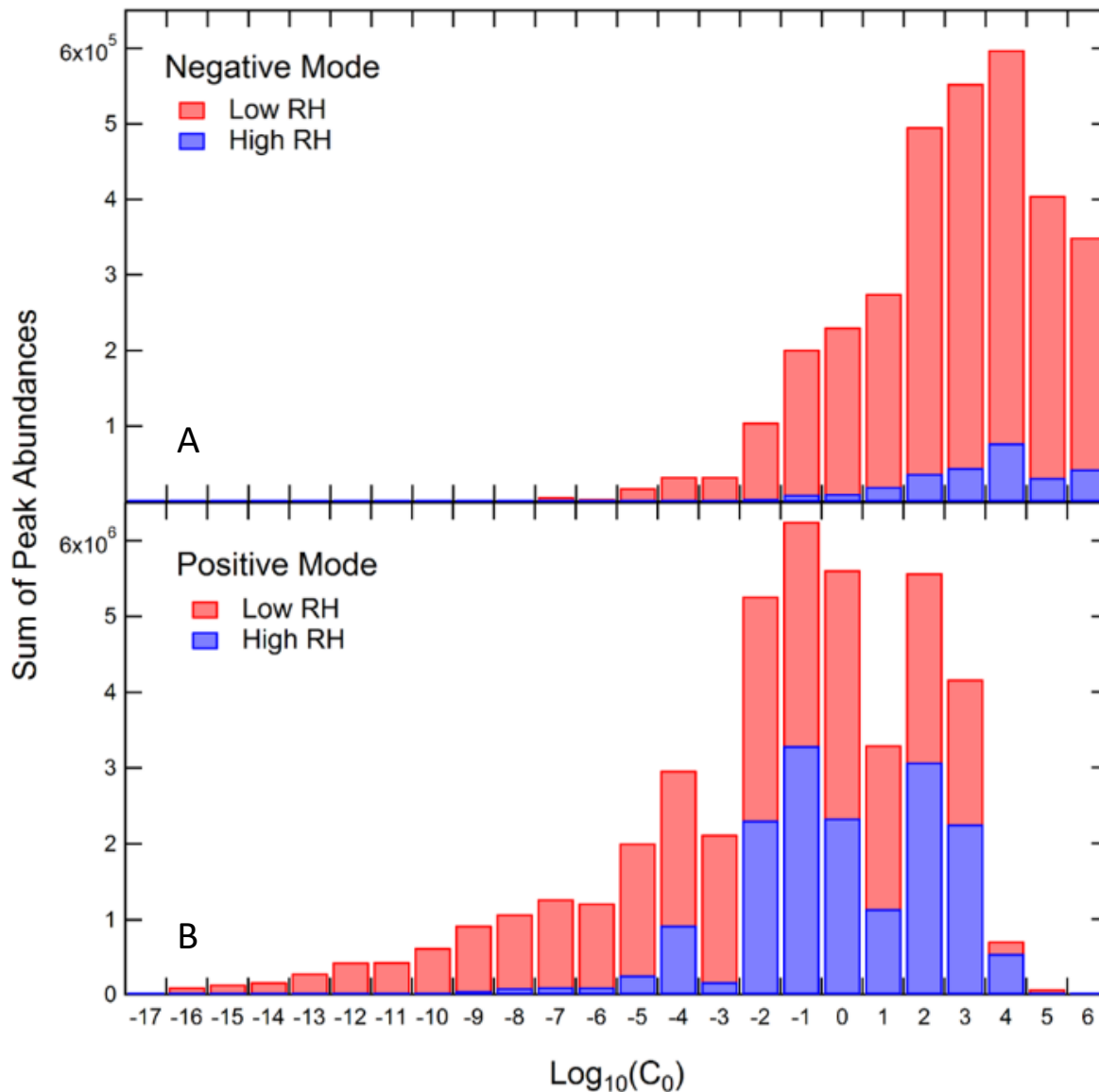


Figure 4.5. Estimated volatility distribution for the compounds observed in the negative (A) and positive (B) ion mode at high (red bars) and low (blue bars) RH. The height of each bar is proportional to the total ESI abundance of compounds falling within the volatility bin.

In both positive and negative ion modes, the compounds falling in the lower volatility bins were visibly suppressed at high RH. For example, the high RH to low RH ratio of the combined

peak abundances for the compounds falling below $\log(C_0) = 1$ is 0.3 in the positive ion mode and 0.05 in the negative ion mode. This is consistent with nearly an order of magnitude suppression in the aerosol yield for low-NO_x toluene SOA.

The suppression of the aerosol yield under high RH conditions could be also be affected by the formation and partitioning kinetics of SOA. At low RH, SOA formation may be controlled by reactive uptake of semivolatile compounds and formation of high molecular weight compounds such as dimers and oligomers.¹⁹⁵ In addition, semivolatile compounds colliding with particles may become physically trapped, and their re-partitioning or evaporation may be suppressed by the glassy solid state of toluene SOA.^{70, 74} For example, Perraud *et al.* observed that, under dry conditions, the growth of SOA particles from oxidation of α -pinene was more consistent with the irreversible uptake of semivolatiles onto particles, and not with the equilibrium gas-particle partitioning.⁶³ Ye *et al.* recently examined RH-dependent gas-particle exchange in high-NO_x toluene SOA, and found that there was resistance to gas-particle exchange below 20% RH but virtually no resistance above 40% RH.⁸⁵ As the RH is increased, the resistance to gas-particle exchange should decrease, and SOA formation should become controlled by quasi-equilibrium growth.¹⁵⁶ If the shift from the irreversible uptake to quasi-equilibrium growth is the primary mechanism for the SOA yield suppression at high RH, based on the result of Ye *et al.*,⁸⁵ we should have observed a large drop in the yield for high-NO_x SOA in addition to that of the low-NO_x SOA. While the high-NO_x SOA yield did decrease at high RH, the decrease was considerably smaller than for the low-NO_x case (Figure 4.2). Therefore, the suppression of the yield at high RH may be a consequence of coupled effects of suppressed oligomerization with the shift from the irreversible uptake to quasi-equilibrium growth mechanism.

4.4: CONCLUSIONS

This study has demonstrated that low-NO_x toluene SOA yield is reduced under high RH conditions. This effect is consistent with observations by Cao *et al.*, who observed a negative correlation between RH and the low NO_x toluene SOA yield, but no correlation between RH and the high NO_x toluene SOA yield.¹⁷⁷ Based on the comparison between the high NO_x and low NO_x SOA yield RH dependence, the plausible reason for the yield suppression at high RH is the change in the SOA chemical composition that favors lower-molecular weight, more volatile compounds. The reduction of dimers and trimers in the high RH samples suggests that low volatility oligomers are not forming in toluene SOA under low NO_x conditions, which means particle growth is suppressed and yield is reduced. Additionally, irreversible uptake of semi-volatile compounds and slow evaporation from a glassy solid matrix may favor faster growth of particles under low RH conditions.

These results have potential impacts in the urban atmospheric environment where toluene is commonly present alongside NO_x because both are emitted by anthropogenic sources. Under high NO_x conditions, the total amount of toluene SOA will most likely not depend strongly on atmospheric RH. However, these results suggest that if NO_x in urban areas is significantly reduced, the total amount of toluene SOA would be similarly suppressed under normal atmospheric conditions (~50% RH), even if toluene emissions stay the same. This may be relevant in cities like Los Angeles, which plan to significantly reduce NO_x emissions.

Additionally, there are many locations that become dry under certain meteorological conditions. For example, during California's Santa Ana winds, the RH regularly decreases below 10% RH. Under such dry atmospheric conditions in a low NO_x environment, the yield

of toluene SOA would no longer be suppressed. This change would result in a “burst” of toluene SOA, changing the overall concentration of SOA in the area. It is also possible that the effect of RH on the SOA yield is a common feature of all low NO_x aromatic SOA. If this is the case, the production of SOA from naturally emitted aromatic compounds (indole, benzyl acetate, benzaldehyde, etc.), which exist in low-NO_x environments, would be strongly modulated by the ambient humidity.

CHAPTER 5

CHEMICAL UPTAKE OF AMMONIA BY SOA PARTICLES

5.1: INTRODUCTION

When secondary organic aerosol (SOA) is formed in the atmosphere, it is exposed to a variety of environmental conditions, including temperature, humidity, and sunlight, as well as pollutants. One such atmospheric pollutant is ammonia (NH_3), which enters the atmosphere from a variety of sources including automobiles, industry, and biomass burning.⁹⁵⁻⁹⁷ However, the largest contribution of ammonia to the atmosphere comes from agriculture, including animal waste and fertilizer application.⁹⁵⁻⁹⁷ Agriculture accounts for roughly half of the total ammonia emissions globally.⁹⁵⁻⁹⁷

Ammonia emissions on a local scale are more variable. In southern California, the amount of ammonia emitted by automobiles is on the same order of magnitude as the amount of ammonia emitted from agricultural sources.⁹⁸ While automobiles are decentralized, agricultural sources of ammonia are more localized. Thus, ammonia is highly concentrated around agricultural areas, reaching mixing ratios of over 100 ppb.⁹⁸

Atmospheric ammonia is well known to neutralize acids, such as nitric acid or sulfuric acid, through reactions 1 and 2. The salts produced by this neutralization process (ammonium nitrate and ammonium sulfate) have low vapor pressure and can condense to form inorganic aerosols. This is a major process that contributes significantly to fine particulate matter, or $\text{PM}_{2.5}$, in southern California.⁹⁹⁻¹⁰⁰



In addition to these processes, which involve the formation of inorganic particulate matter, recent evidence has shown that ammonia can react with certain organic compounds in SOA. Biogenic SOA exposed to ammonia was observed to undergo a browning process as a result of chemical reactions between ammonia and carbonyl species. This process leads to the formation of highly-conjugated light-absorbing nitrogen-containing organic compounds (NOC).¹⁰¹⁻¹⁰⁵ The general mechanism, shown in Figure 5.1, involves the reaction of ammonia with carbonyls within the SOA to produce primary imines and amines, which releases water from the SOA particle. The products subsequently react with carbonyls in the SOA to form more stable secondary imines.

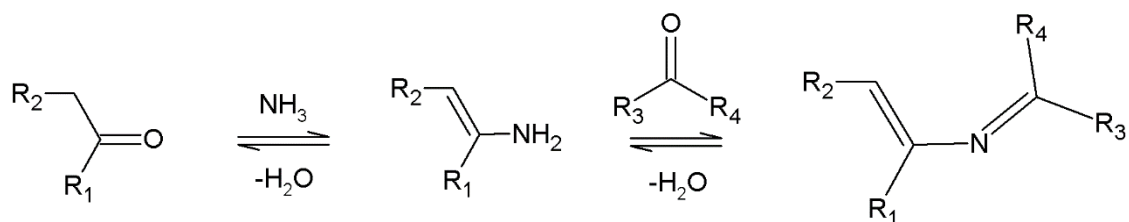


Figure 5.1. Mechanism of formation of nitrogen-containing organic compounds.

Liu *et al.* (2015) recently reported chemical uptake coefficients for ammonia onto α -pinene SOA and m-xylene SOA.¹⁰⁷ The uptake coefficients were calculated from the change in nitrogen mass in the SOA particle after exposure to ammonia. The concentration of nitrogen-containing organic compounds was determined by fitting peaks including those from the NH_x, NO_x, C_xH_yN_n, C_xH_yON_n and C_xH_yO₂N_n fragment groups detected by a high resolution time of flight aerosol mass spectrometer (ToF-AMS).

The formation of SOA from gasoline vehicle exhaust was studied in the presence and absence of ammonia.¹⁰⁸ The authors found that particle mass loading increased rapidly in the

presence of ammonia to much higher levels than in its absence.¹⁰⁸ In this case, most of the increase was probably due to reaction 5.1 because gasoline vehicle exhaust contains plenty of NO_x, which can photooxidize to nitric acid. However, reactions shown in Figure 5.1 could contribute as well. Despite this evidence that the presence of ammonia can change aerosol composition, as well as the total mass loading, the effects of ammonia still need to be incorporated in air quality models.

It is important to understand the interactions between SOA and ammonia, given that various global trends point towards an increase in ammonia emissions. The population is expected to continue growing in the future, which will increase agricultural production. The number of cattle and buffalo, which emit the largest amount of ammonia of all livestock, is expected to increase by 360 million relative to the 1999 cattle population (1.497 billion animals). These trends indicate that the concentration of ammonia will increase significantly over the next few decades, particularly in areas where the population is growing the fastest. According to the Food and Agriculture Organization of the United Nations, annual ammonia emissions from livestock are expected to increase by 60% (or 18,000 metric tons) by 2030 from 1999 levels.¹⁰⁹ This increase will be most evident in developing countries, where the annual ammonia emissions are projected to increase by 17,000 metric tons.¹⁰⁹ Additionally, ammonia emissions have been shown to increase significantly under warmer temperatures which shift equilibria (1) and (2) to the left.¹¹⁰⁻¹¹² A projected increase in temperature of 2-4 °C due to climate change could lead to overall increases of up to 10-27% in ammonia emissions.¹¹³ This increase in temperature is also expected to increase emission of VOCs from most sources,¹¹⁴ which will lead to more SOA. Since both ammonia emissions and SOA

production will be increasing in the coming decades, it is important to understand how their interactions will affect particle concentration and composition.

The goal of this work was to experimentally study the uptake of ammonia onto different types of laboratory-generated SOA and incorporate this information into the Dabdub group's University of California, Irvine-California Institute of Technology (UCI-CIT) airshed model in order to understand how this uptake may affect air quality now and in the future as the climate changes. The studied SOA precursors were limonene, n-hexadecane, or toluene. Limonene was chosen as a representative of biogenic VOCs because it is one of the most important monoterpenes. It has also been shown to react visibly under exposure to ammonia vapors (see Chapter 2). N-hexadecane represented anthropogenic alkanes from diesel, and toluene was chosen to represent aromatic, anthropogenic VOCs.

5.2: EXPERIMENTAL

SOA for these experiments was produced in a 5 m³ smog chamber by photooxidation of either limonene, n-hexadecane, or toluene under low or high NO_x conditions. Limonene SOA was also produced via dark ozonolysis. Before each experiment, the chamber was humidified by flowing purified air (typical VOC mixing ratios below 1 ppb) through a Nafion humidifier (PermaPure) until the RH reached 50%. Then the air flow was shut off and the chamber sealed. A diagram of the smog chamber is provided in Figure 5.2.

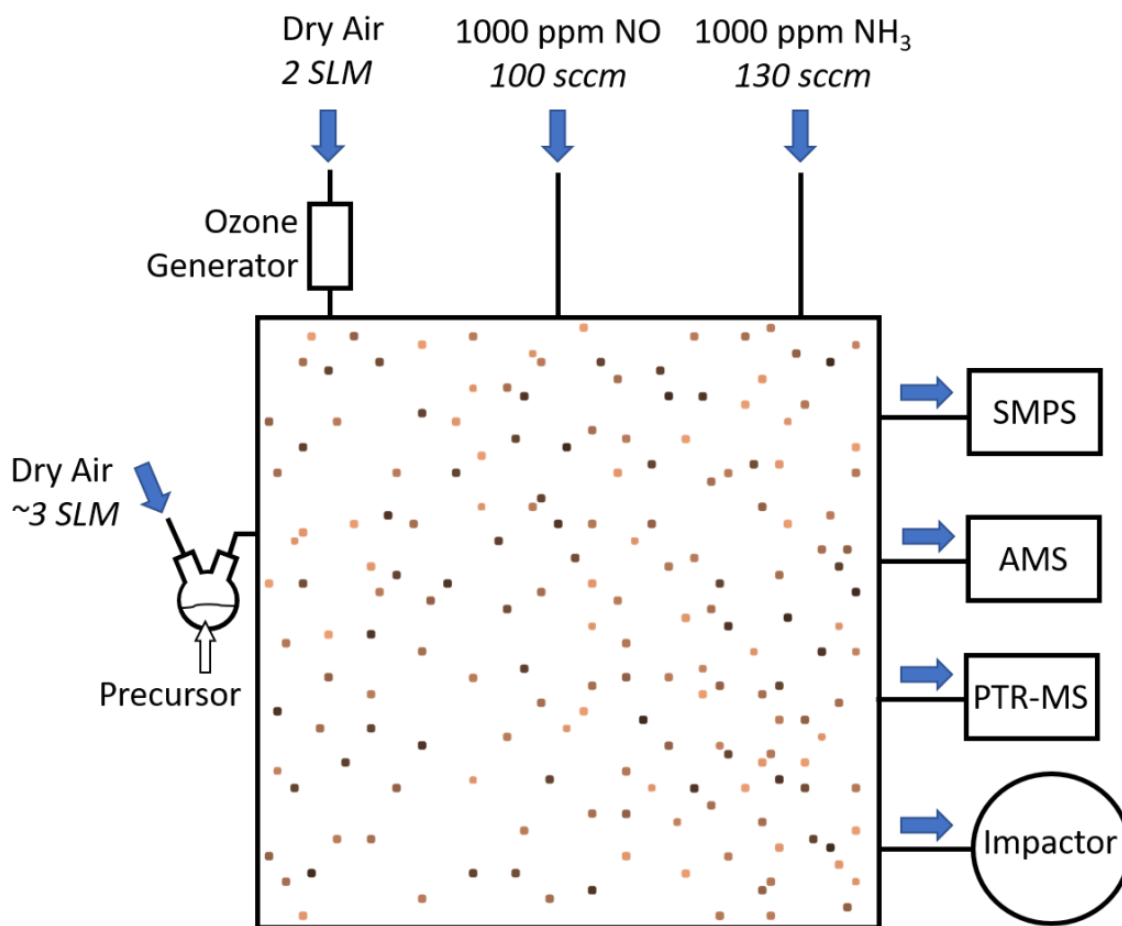


Figure 5.2. Diagram of the Nizkorodov Lab Smog Chamber. The inlet flows are not continuous but rather applied for a short period of time to inject a given reactant.

To produce SOA via photooxidation, hydrogen peroxide (H_2O_2) was introduced to the chamber by injecting a measured amount of aqueous H_2O_2 (30 wt%) into a bulb where it was evaporated under a flow of dry air and carried into the chamber. After 30 minutes of flowing air through the bulb at 3 SLM, the H_2O_2 had completely evaporated as verified by visual inspection. Next, the precursor (toluene, n-hexadecane, or limonene) was introduced into the chamber by the same method as the H_2O_2 . The time needed to completely evaporate the VOC was much shorter; usually 5 minutes. Both high and low NO_x experiments were performed. In the high NO_x experiments, gaseous NO (1000 ppm in N_2) was added to the

chamber over a period of 3 minutes at a flow rate of 100 SCCM to achieve a total NO concentration of 300 ppb. Nothing was added for low NO_x experiments. After all the reactants were added and mixed within the chamber with a fan, the fan was shut off and the UV lamps were turned on to initiate the photooxidation of the precursors and particle formation. The particle concentration continued to grow over 1 to 3 hours depending on the precursor.

To generate SOA via dark ozonolysis, ozone (O₃) was produced using a commercial ozone generator in a flow of pure oxygen, which flowed into the chamber at a rate of 2 SLM for 30 seconds to reach a mixing ratio of 500 ppb of ozone. The concentration of ozone was monitored throughout the experiment using an ozone monitor. The ozone was mixed within the chamber for 5 minutes using a fan located inside the chamber to allow even distribution within the chamber. Next, 3 μL of limonene was injected into a bulb, where it was evaporated and carried into the chamber under a flow of dry air. This resulted in a limonene mixing ratio of 100 ppb. The SOA began to form rapidly inside the chamber as the limonene was oxidized by the ozone. The particle concentration continued to grow over the next hour until the total particle mass concentration reached just over 250 μg/m³.

After the SOA concentration had reached its maximum, ammonia was introduced to the chamber at a flow rate of 130 SCCM from a gas cylinder containing 1000 ppm of ammonia in N₂. The ammonia was added for either 5 or 25 minutes, theoretically resulting in a mixing ratio of ammonia of either 100 or 500 ppb, respectively. However, subsequent experiments were performed to determine the actual ammonia concentration within the chamber using an Ecotech EC 9842 series NO_x/NH₃ analyzer. Adding ammonia to the chamber for 5 minutes resulted in a concentration of 50 ppb, while adding ammonia for 25 minutes yielded a

concentration of 200 ppb, with the rest presumed lost on the injector surfaces and chamber walls.

Throughout each experiment, particle concentrations were monitored with a Scanning Mobility Particle Sizer (SMPS Model 3080, TSI Inc.), while the temperature (± 1 °C) and RH ($\pm 2\%$ RH) were monitored with a Vaisala HMT330 probe. Lastly, a time of flight aerosol mass spectrometer (ToF-AMS, Aerodyne) was used to monitor the composition of the SOA before and after addition of ammonia. In addition, the particles could be collected onto Teflon filters for offline Direct Analysis in Real Time Mass Spectrometry (DART-MS) analysis. The DART-MS consisted of a Xevo TQS quadrupole mass spectrometer (Waters) equipped with a commercial DART ion source (Ion-Sense, DART SVP with Vapur ® Interface). These experiments are ongoing, but we have done a range of experiments so far. A summary of the experiments that have been completed are summarized in Table 5.1.

Table 5.1. Summary of experiments. A green X represents experiments that have been completed and a red O represents experiments that will need to be done in the future.

	Precursor	Limonene	n-hexadecane	Toluene
Low NO _x	O ₃ , 50 ppb NH ₃	X	-	-
	O ₃ , 200 ppb NH ₃	X	-	-
	OH, 50 ppb NH ₃	O	X	X
	OH, 200 ppb NH ₃	O	X	X
High NO _x	O ₃ , 50 ppb NH ₃	-	-	-
	O ₃ , 200 ppb NH ₃	-	-	-
	OH, 50 ppb NH ₃	X	X	X
	OH, 200 ppb NH ₃	X	O	X

5.3: RESULTS AND DISCUSSION

In our chamber experiments, we investigated the effect of ammonia on each type of SOA under high and low NO_x conditions. The SMPS data for each type of experiment is shown in Figure 5.3 below. In all cases the low NO_x experiments showed no significant change in particle mass loading upon addition of the ammonia. However, in the high NO_x experiments there was a clear increase in particle mass loading immediately following the addition of ammonia into the chamber. This increase in particle mass concentration was accompanied by an increase in particle size, from around 300 nm average diameter to 319 nm, as measured by the SMPS.

The SMPS data shown in Figure 5.3 was collected during experiments where ammonia was added to the chamber for 5 minutes. This concentration of ammonia (~50 ppb) was sufficient to increase the particle mass loading for the high NO_x experiments. However, the following results were obtained with a mixing ratio of 200 ppb, by adding ammonia to the chamber for 25 minutes.

In a few experiments the SOA was generated in the chamber under low NO_x conditions in the absence of ammonia and collected onto a Teflon filter for offline DART analysis. Each Teflon filter was cut in half. One half was placed in a small petri dish, which was then placed inside a large petri dish filled with 30 mL of 0.1 M ammonium sulfate (>99%, EMD). Then the lid to the large petri dish was placed over both petri dishes. This technique allows the SOA on the filter to absorb the vapors (estimated to contain 300 ppb ammonia using the AIM-II model) without touching the solution. The entire unit of petri dishes was stored in a dark cupboard for two days.

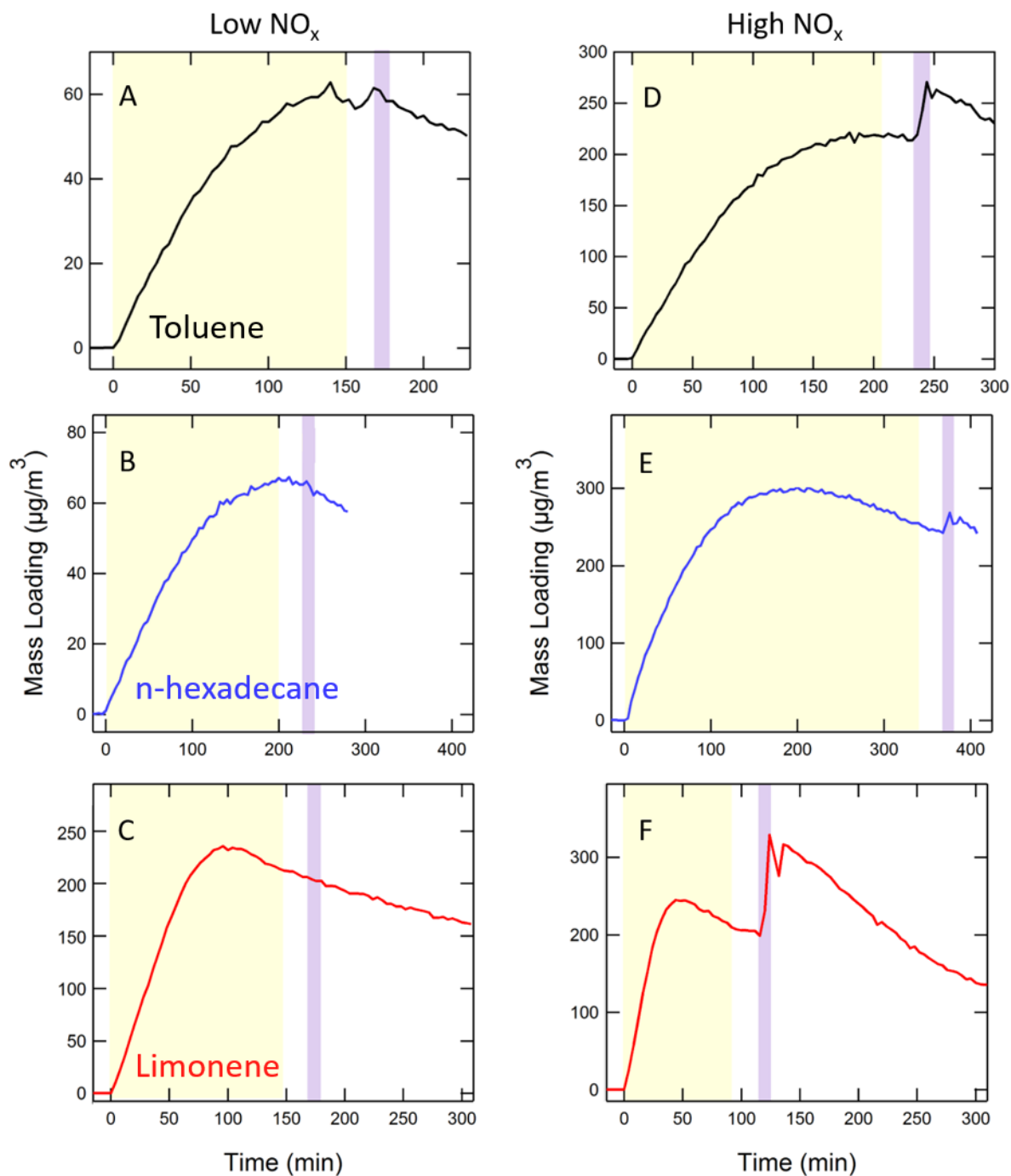


Figure 5.3. SMPS data for A) toluene/OH (black) SOA low NO_x B) n-hexadecane/OH (blue) SOA low NO_x C) limonene/OH SOA (red) low NO_x D) toluene/OH (black) SOA high NO_x E) n-hexadecane/OH (blue) SOA high NO_x F) limonene/OH SOA (red) high NO_x. The yellow section indicates the time during which the lamps were on. The purple section indicates the time during which ammonia is introduced to the chamber (5 minutes, 50 ppb).

The other half of the Teflon filter was placed in a different small petri dish, which was set inside a large petri dish filled with 30 mL of nanopure water. Then the petri dishes were covered and store in an identical manner as the ammonium sulfate exposed sample. This half of the sample filter acted as a control.

After two days of aging, each aged SOA sample was extracted into acetonitrile. An aliquot (~60 μL) of blank acetonitrile and of each sample solution was pipetted onto a wire mesh separately. DART-MS was then performed on the blank and both solutions by evaporating the solution off of the wire mesh in front of a flow of dry air to carry the sample into the DART-MS.

The DART-MS data were analyzed (with the blank MS spectrum subtracted) to see whether nitrogen was being incorporated into organic molecules, following the ammonia exposure. A proton is added (positive mode) or subtracted (negative mode) under typical DART ionization conditions. Therefore, we observe largely unfragmented molecular ions of with an m/z of $[M+1]^+$ in the positive ion mode or $[M-1]^-$ ions in the negative ion mode.¹⁹⁶ The initial SOA compounds, before they are exposed to ammonia, consist of C, H, and O atoms (CHO compounds). Such CHO compounds have even nominal molecular weights and, therefore, show up at odd nominal m/z values under DART ionization mechanisms. On the other hand, compounds containing one nitrogen atom (CHON) have odd nominal molecular weights, and should show up at even m/z values. If SOA compounds react with ammonia the peaks at even m/z values will increase in abundance. Therefore, the fraction of nitrogen containing compounds in the sample exposed to ammonia can be estimated using the following equations:

$$f_N = \frac{1}{\sigma} (Ratio_{NH_3} - Ratio_{control}) \quad \text{Equation 5.1}$$

$$Ratio = \frac{\sum_{even} I_i}{\sum_{odd} I_i} \quad \text{Equation 5.2}$$

The parameter σ accounts for higher ionization probability of CHON relative to CHO compounds. In the absence of better information, the average detection sensitivity for CHO and CHON was assumed to be equal ($\sigma = 1$ for this analysis). The results of this analysis are shown in Table 5.2.

Table 5.2: Nitrogen fraction in each type of sample exposed to ammonia.

SOA Sample	Nitrogen Fraction f_N
Toluene/OH	5%
n-hexadecane/OH	5%
Limonene/O ₃	11%

The estimated nitrogen fraction of limonene/O₃ SOA exposed to ammonia was double the nitrogen fraction of either of the other two types of SOA suggesting that ammonia reacts more efficiently with the components of limonene/O₃. This effect is consistent with previous observations by Updyke *et al.* who observed that limonene/O₃ SOA changed its mass absorption coefficient (MAC) the most compared to other types of SOA.¹⁰⁴ However, this comparison is difficult to make because Updyke *et al.* results were based on the change in MAC values of various types of SOA after exposure to ammonia, and not on the actual measurements of the nitrogen fraction in the exposed SOA.¹⁰⁴ It is possible that SOA tested in Updyke *et al.* studied were reacting similarly to limonene SOA, but did not increase in MAC. Indeed, Laskin *et al.* found that ammonia did react with both α -pinene/O₃ SOA and

limonene/O₃ SOA producing NOC, but unlike the limonene/O₃ SOA sample, the α-pinene/O₃ SOA sample did not brown.¹⁰⁵

We also performed this analysis on one limonene/O₃ SOA sample that was exposed to ammonia in the chamber (while the SOA was in the aerosol phase) rather than in a petri dish. The nitrogen fraction of this sample estimated from Equation 5.1 was 20%. This sample was exposed to ammonia inside the chamber at a concentration of roughly 200 ppb for around 1.5 hours. This suggests that ammonia reacts significantly faster with SOA in the aerosol phase than in the collected bulk phase. This could be due to much faster diffusion of ammonia through small aerosol particles in the chamber compared to that through the bulk SOM material in the Petri dish experiments.

An estimate for the uptake coefficient for limonene SOA under low NO_x conditions was attempted using the following equation:

$$\gamma = \frac{4 \cdot N_A \cdot f_N \cdot C_{mass}}{v \cdot C_{area} \cdot C_{NH_3} \cdot \Delta t \cdot MW} \quad \text{Equation 5.3}$$

where N_A is Avogadro's number, f_N is the nitrogen fraction calculated in the DART-MS experiment, C_{mass} is the particle mass concentration from the SMPS measurements, v is the average speed of ammonia molecules at room temperature calculated from the Maxwell-Boltzmann distribution to be 610 m/s, C_{area} is the total particle area concentration of the particles, also from the SMPS measurements, C_{NH_3} is the concentration of ammonia in the chamber, Δt is the time that the particles were exposed to ammonia, and MW is the average molecular weight of the SOA particles (assumed to be 300 g/mol in this estimate).

Based on this experiment, we estimate that ammonia is being taken up by limonene SOA with an uptake coefficient of $\sim 1 \times 10^{-5}$ under low NO_x conditions. Previous work by Liu *et al.* reported uptake coefficients of on the order of 10^{-3} for the first three hours of ammonia exposure. The uptake coefficient after 7 or more hours of exposure was calculated to be much lower, on the order of 10^{-5} .¹⁰⁷ Our estimated uptake coefficient for limonene SOA is on the lower end of this range. However, we will need to perform more in-depth uptake experiments to determine uptake coefficients for each type of SOA more concretely.

These preliminary experiments have shown that limonene SOA can take up ammonia in our chamber experiments under low NO_x conditions without increasing the particle mass loading. However, we did observe an increase in mass loading under high NO_x conditions. ToF-AMS data allowed us to compare the effect of ammonia on low NO_x and high NO_x SOA composition. Figure 5.4 compares the effect of ammonia on the composition of low NO_x and high NO_x toluene SOA and Figure 5.5 compares the effect on limonene SOA.

Under high NO_x conditions, there was a rapid increase in NH and NO fragments in all types of SOA immediately following the addition of ammonia to the chamber. The NH family of fragments includes NH^+ , NH_2^+ , NH_3^+ , and NH_4^+ . The NO family of fragments includes NO^+ , NO_2^+ , and NO_3^+ . This increase was accompanied by a significant increase in particle mass concentration and particle geometric mean diameter. All of this points toward the condensation of ammonium nitrate onto the SOA particles. In high NO_x experiments nitric acid builds up in the chamber as a result of the reaction between NO_2 with OH. Ammonia can react with the nitric acid to form ammonium nitrate, which has much lower volatility than nitric acid, leading to its condensation onto particles.

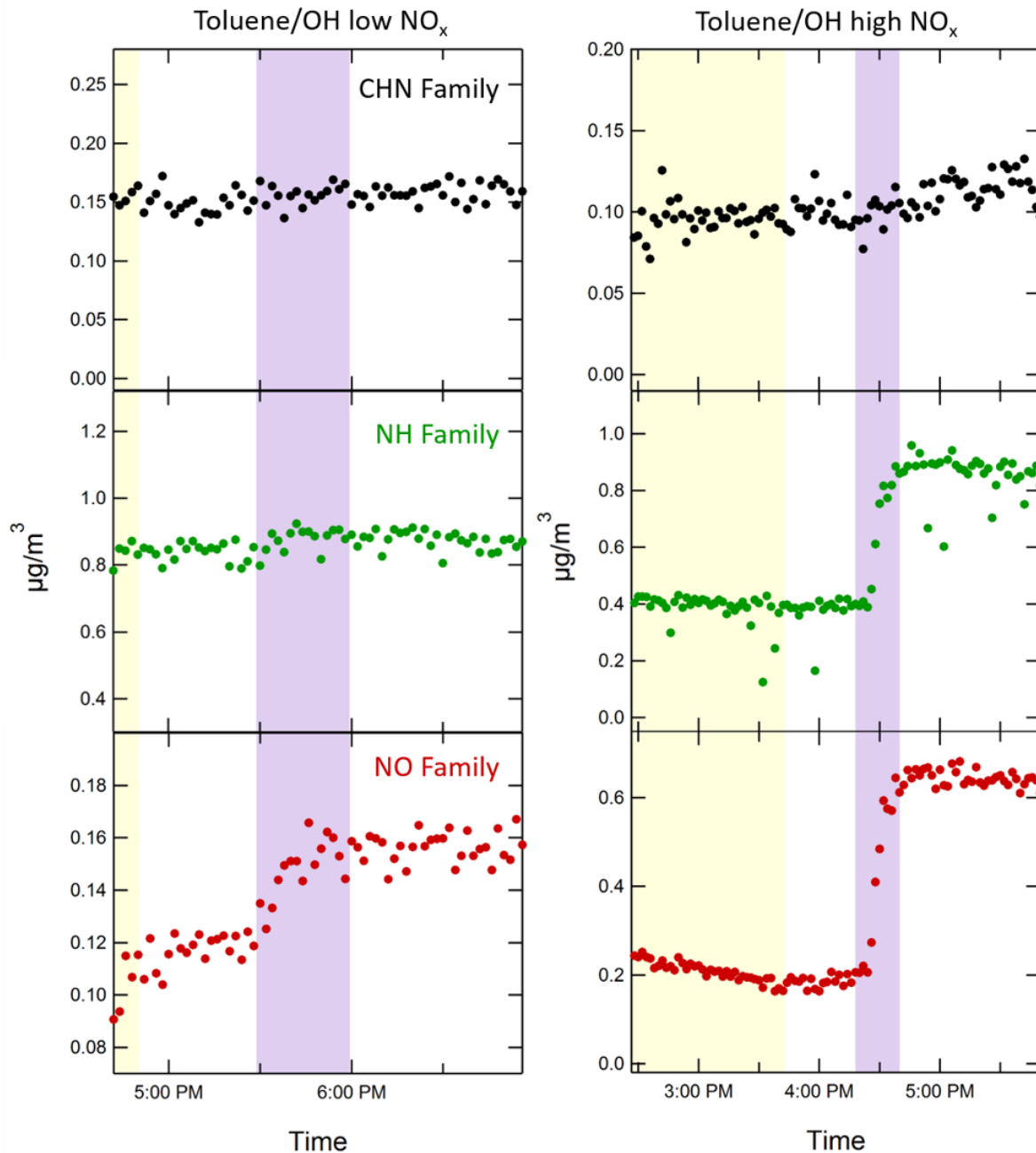


Figure 5.4. ToF-AMS data for toluene/OH SOA under low NO_x (left) and high NO_x (right) conditions. The yellow region indicates the time during which the light was on for photooxidation. The purple region indicates the time during which ammonia was added to the chamber. The CHN family of ToF-AMS fragments is plotted in black in the top panels. The NH family of fragments is plotted in green in the middle panels. The NO family of fragments is plotted in red in the bottom panels.

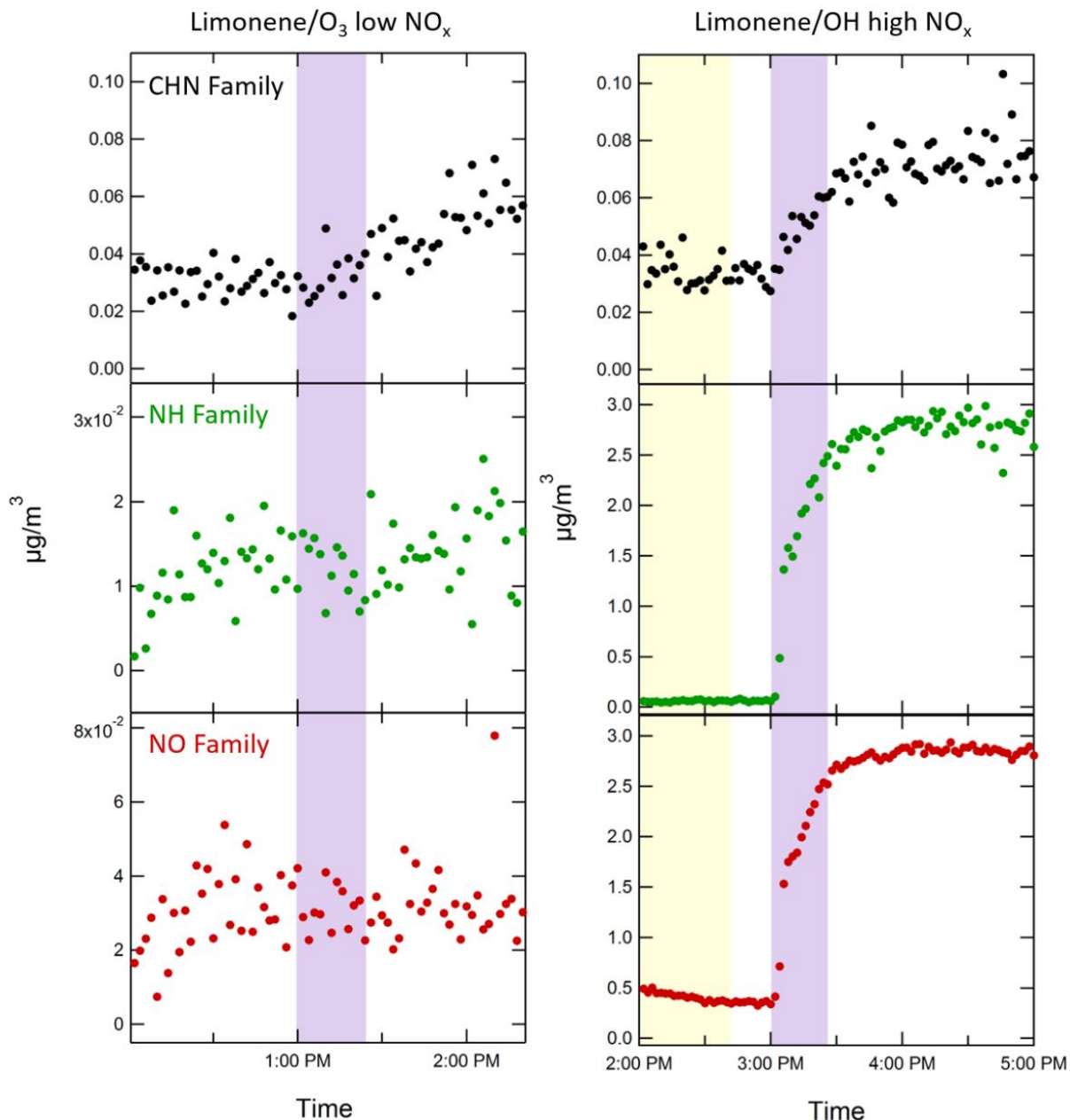


Figure 5.5. ToF-AMS data for limonene/O₃ SOA under low NO_x (left) and limonene/OH SOA under high NO_x (right) conditions. The yellow region indicates the time during which the light was on for photooxidation. The purple region indicates the time during which ammonia was added to the chamber. The CHN family of ToF-AMS fragments is plotted in black in the top panels. The NH family of fragments is plotted in green in the middle panels. The NO family of fragments is plotted in red in the bottom panels.

The toluene/OH high NO_x SOA system also showed a very slight increase in the CHN family. The CHN family includes all ionic fragments with the general formula C_cH_hN_n⁺. This increase was much more pronounced in the limonene/OH high NO_x SOA system. However, it is not clear whether this is a real result of the experiment or an artifact arising from formation of CHN compounds during pyrolysis of SOA/ammonium nitrate on the AMS vaporizer.

Under low NO_x conditions the limonene/O₃ SOA showed a gradual increase in CHN fragments upon addition of ammonia. The CHN fragments continued to grow for at least an hour. The specific fragments that were observed to increase were CHN⁺, C₂H₃N⁺, C₂H₄N⁺, and C₃H₈N⁺. Since under low-NO_x condition, the only possible source of nitrogen in the particles is the SOA + NH₃ reaction, this observation supports the assumption that ammonia is being taken up by the SOA and reacts with carbonyls in the aerosol. However, the increase in CHN fragments was not accompanied by an increase in particle mass concentration. This suggests that as ammonia enters the particle it displaces water molecules as described in Scheme 1.

The increase in CHN fragments was not observed in toluene/OH SOA or in n-hexadecane/OH SOA. These observations, in combination with the DART-MS results, suggest that, of the three systems studied, limonene/O₃ SOA was the most reactive with ammonia. Limonene ozonolysis products have been shown to contain many carbonyls and dicarbonyls.¹⁹⁷ It is likely the presence of these carbonyl groups that make limonene/O₃ SOA so reactive with ammonia. It is also well known that ammonia, along with amines, react readily with carbonyls to produce imines, which would yield the CHN fragments that we observed in the ToF-AMS.

There was also a slight increase in NO fragments in the toluene/OH SOA experiment under low NO_x conditions. However, this increase was an order of magnitude less than in the high NO_x experiment and may be due to low levels of NO_x impurities in the chamber.

5.4: CONCLUSIONS

This work has demonstrated that SOA can take up ammonia from the surrounding atmosphere by a mechanism that was not previously considered in air quality models. Ammonia reacts with carbonyls to form imines, releasing water from the aerosol particle. However, this process depends on the type of SOA. Our results suggest that the uptake of ammonia onto limonene/O₃ SOA and similar SOA types containing many carbonyl groups would be expected to be much stronger than onto the other types of SOA, likely due to the presence of carbonyls.

In order to study the impact that this uptake could have on air quality, we collaborated with the Dabdub group. They customized the UCI-CIT air-shed model to include an uptake coefficient ranging from 10^{-5} to 10^{-2} for ammonia onto SOA. Then they compared their simulated scenario to the base case scenario, which no uptake of ammonia was included. Including the uptake in the model with the uptake coefficient of 10^{-2} resulted in a decrease in ammonia of up to ~50%. The largest decrease of ammonia was observed near Chino, where there is a large amount of agricultural activity. Furthermore, the reduction of atmospheric ammonia resulted in a decrease in inorganic aerosols and overall PM_{2.5} in the area. This is shown in Figure 5.6, which depicts the difference in 24-hour average PM_{2.5} from the base case.

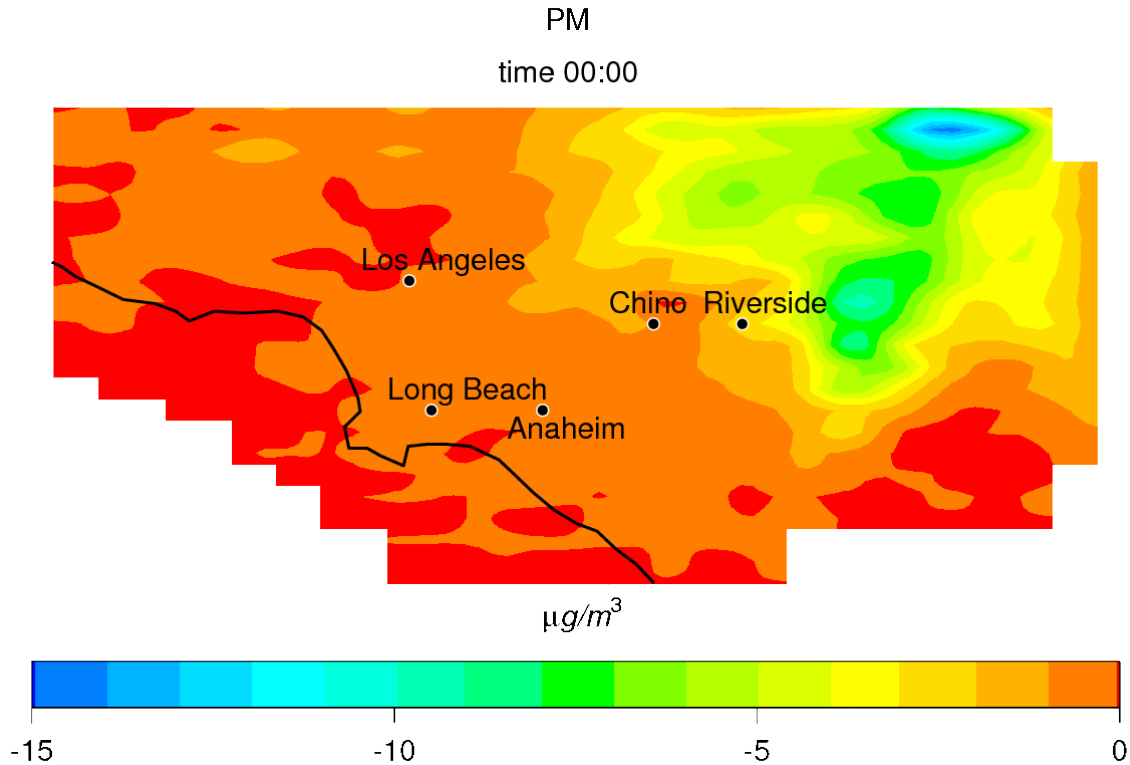


Figure 5.6. Difference from base case in 24-hour average of $\text{PM}_{2.5}$ when including ammonia uptake onto SOA using an uptake coefficient of 1×10^{-2} .

The contour plot shows a decrease of $15 \mu\text{g}/\text{m}^3$ in the 24-hour average in $\text{PM}_{2.5}$ in the northeastern region of the South Coast Air Basin. This region tends to accumulate pollutants as the prevailing winds blow inland from the ocean. This is a significant decrease, considering that in the U.S. the 24-hour average air quality standard for $\text{PM}_{2.5}$ is $35 \mu\text{g}/\text{m}^3$.

The uptake coefficient used for this model was on the higher end of the uptake coefficients reported by Liu *et al.* and was intended to represent the maximum effect that the uptake of ammonia onto SOA particles could have on air quality. The estimated uptake coefficient for ammonia into limonene SOA obtained from these preliminary experiments was significantly lower. When uptake coefficients on the order of 10^{-5} were incorporated into the model, there was little to no effect on $\text{PM}_{2.5}$ concentrations in SoCAB.

Previously, air quality models did not include any interactions between SOA and ammonia. However, these preliminary results indicate that the uptake of ammonia could significantly impact the concentration of particles in certain, localized areas, depending on the uptake coefficient. The next step of this project is to determine precise uptake coefficients for ammonia onto each type of SOA in order to obtain more accurate predictions for air quality in the South Coast Air Basin of California.

CHAPTER 6

SUMMARY

The goal of this dissertation was to understand the how SOA particles change as they are exposed to a wide range of atmospheric conditions, specifically to solar radiation, humidity, and gaseous ammonia. With laboratory-generated SOA used as proxies for ambient particulate matter, the experiments described in this dissertation have improved fundamental understanding of aerosol processes and properties and provided useful input to air quality models. In the long run, results of this work will help us better understand the influence SOA will have on Earth's current atmosphere and future climate.

In Chapter 2, the effect of temperature and relative humidity on the photodegradation kinetics of 2,4-DNP in α -pinene SOM and limonene SOM was investigated. Similar experiments with brown limonene SOM were also carried out. In all cases, as the viscosity of the SOM was increased by either cooling the material or exposing it to dry air, the reaction rate decreased. Additionally, in Chapter 3, the viscosity of toluene/limonene SOM was adjusted by changing the precursor mixture ratio. Again, as the viscosity of the SOM was increased, by using higher proportions of toluene in the precursor mixture, the rate of photodegradation decreased. The results of these two studies suggest that photolabile pollutants that become trapped in SOA will have longer lifetimes in colder, drier parts of the atmosphere.

Next, the effect of RH on the mass loading and composition of toluene SOA were studied in Chapter 4. When toluene photooxidation was performed under drier conditions the mass concentration of particles was lower than under humid conditions. However, this effect was not observed under high NO_x conditions. In addition, the SOA formed with high humidity contained more oligomers than the dry SOA. The reduction of dimers and trimers in the high

RH samples suggests that low volatility oligomers are not forming in low NO_x toluene SOA, which means particle growth is suppressed and yield is reduced. These results suggest that if NO_x in urban areas is significantly reduced, the total amount of toluene SOA would be similarly suppressed under normal atmospheric conditions (~50% RH), even if toluene emissions stay the same. There are also many locations that become dry under certain meteorological conditions. When the humidity in these locations drops, under low NO_x conditions there would be a “burst” of toluene SOA, changing the overall concentration of SOA in the area.

Finally, the interaction of ammonia with SOA was studied in Chapter 5. It was demonstrated that SOA can reactively take up ammonia from the surrounding atmosphere. Ammonia reacts with carbonyls in the SOA particles to form imines, releasing water from the aerosol particle. Our results showed that the uptake of ammonia onto limonene/ O_3 SOA is stronger than onto the other types of SOA suggesting that different types of SOA have different reactivity towards ammonia. These interactions between ammonia and SOA have the potential to significantly impact the concentration of particles in certain, localized areas by reducing the formation of inorganic aerosols. This also means that there will be less ammonia available to neutralize atmospheric acids, such as nitric acid and sulfuric acid. This chemistry will become even more relevant in the future as ammonia emissions are expected to increase.

APPENDIX

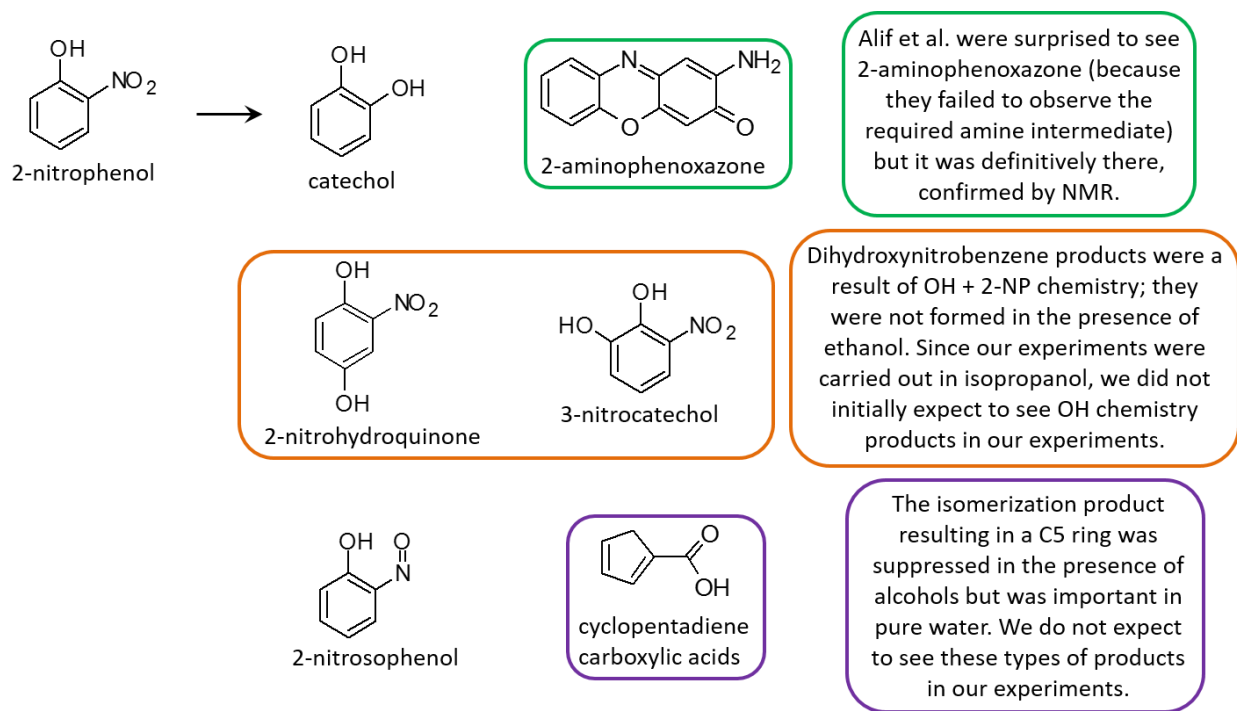


Figure A.1. Summary of known photolysis products of 2-nitrophenol (2-NP) reported by Alif *et al.* (1991)

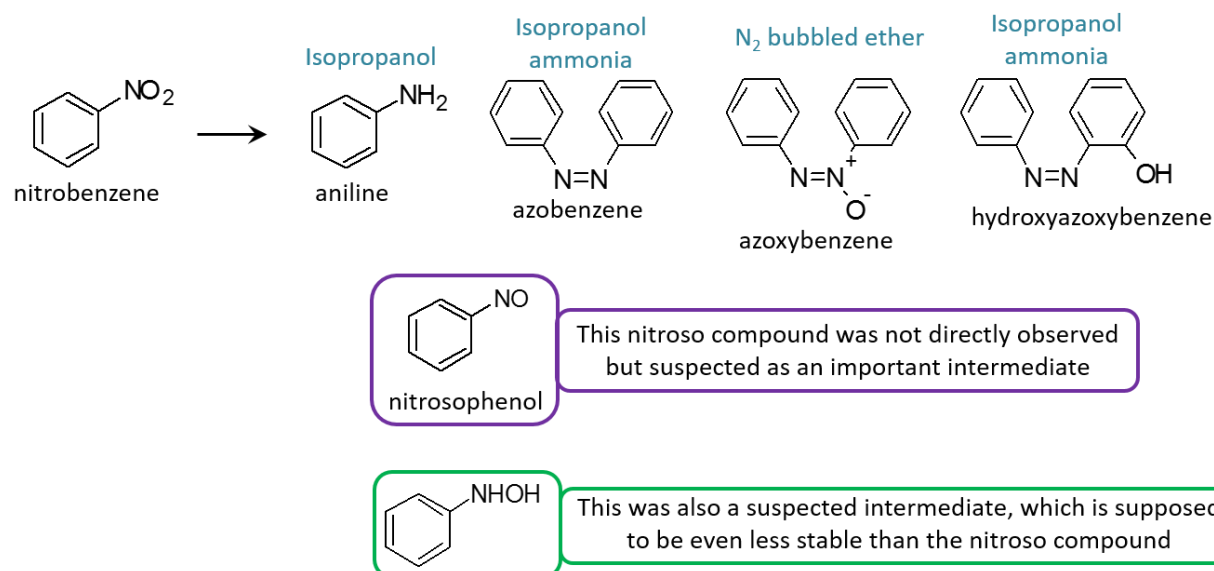


Figure A.2. Summary of known photolysis products of nitrobenzene (NB) by Barltrop *et al.* (1967, 1968) Solvents serving as good H-atom donors (isopropanol) promoted reduction of $-NO_2$ all the way to $-NH_2$.

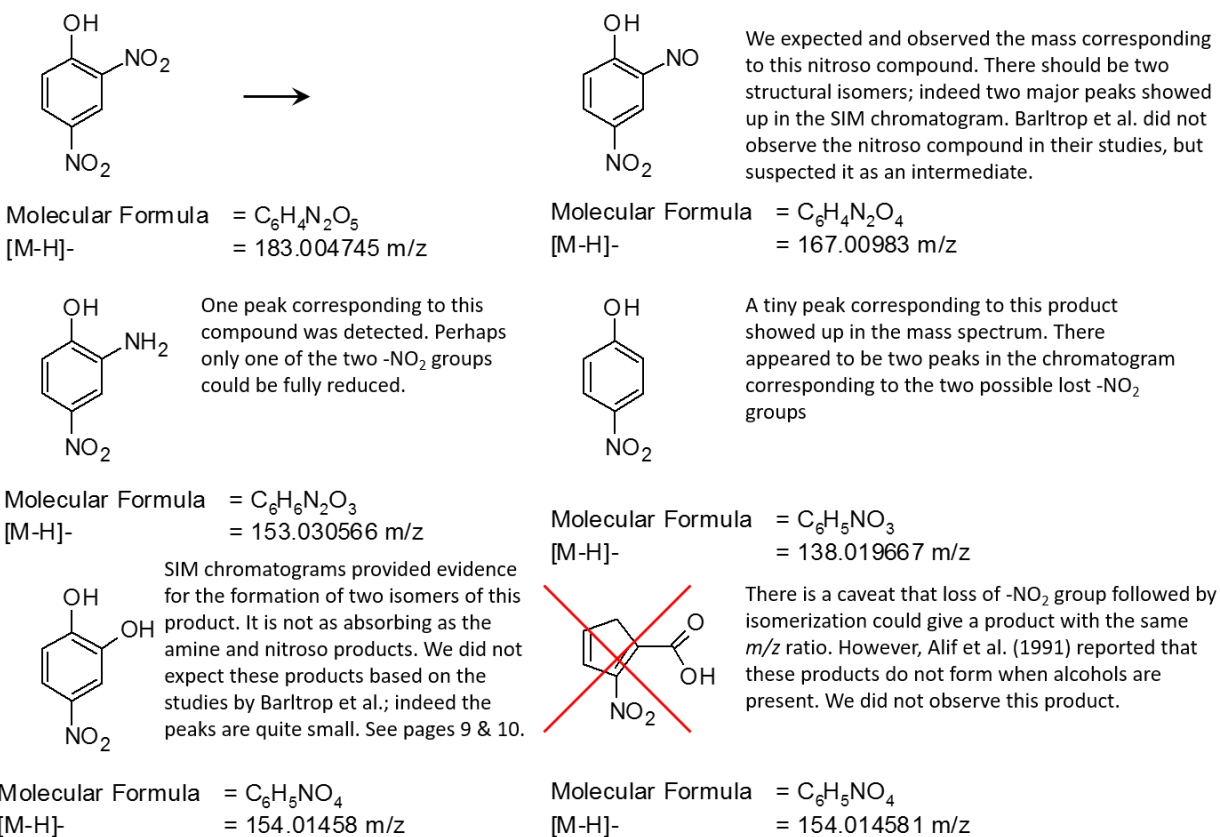
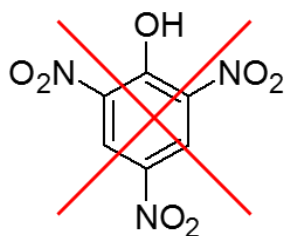


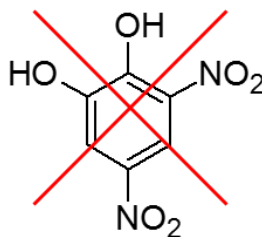
Figure A.3. Summary of expected and possibly observed monomeric products of photolysis of 2,4-DNP. These products could be expected in the photolysis of 2,4-DNP. Species with the expected m/z values appeared in the LC-MS spectra, which suggest (but does not prove) that they were present.

This would have resulted
from nitration of 2,4-DNP



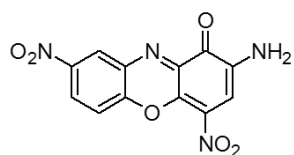
Molecular Formula = C₆H₃N₃O₇
[M-H]⁻ = 227.989823 Da

This would have resulted
from OH addition to 2,4-DNP

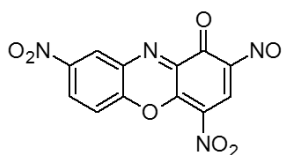


Molecular Formula = C₆H₄N₂O₆
[M-H]⁻ = 198.999659 Da

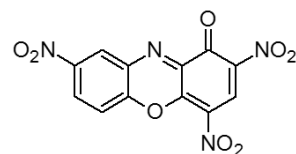
Figure A.4. Summary of expected and possibly observed monomeric products of photolysis of 2,4-DNP. These products could also be expected in photolysis of 2,4-DNP but we saw no evidence of these products in the mass spectrum.



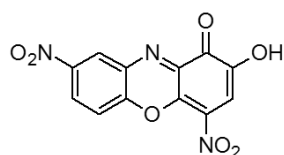
Molecular Formula = $C_{12}H_6N_4O_6$
 [M-H]⁻ = 301.021457 Da



Molecular Formula = $C_{12}H_4N_4O_7$
 [M-H]⁻ = 315.000722 Da



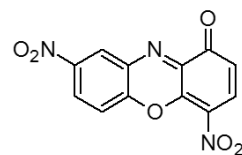
Molecular Formula = $C_{12}H_4N_4O_8$
 [M-H]⁻ = 330.995637 Da



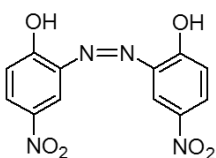
Molecular Formula = $C_{12}H_5N_3O_7$
 [M-H]⁻ = 302.005473 Da



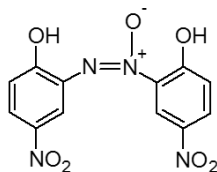
Molecular Formula = $C_{12}H_6N_2O_6$
 [M-H]⁻ = 273.015309 Da



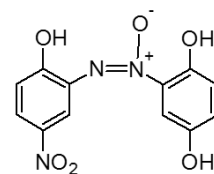
Molecular Formula = $C_{12}H_5N_3O_6$
 [M-H]⁻ = 286.010558 Da



Molecular Formula = $C_{12}H_8N_4O_6$
 [M-H]⁻ = 303.037108 Da



Molecular Formula = $C_{12}H_8N_4O_7$
 [M-H]⁻ = 319.032022 Da



Molecular Formula = $C_{12}H_9N_3O_6$
 [M-H]⁻ = 290.041859 Da

Figure A.5. Summary of expected and Possibly observed dimeric products of photolysis of 2,4-DNP. These dimeric products could also be expected in photolysis of 2,4-DNP. However, only the structure boxed in red is a possible match to the observed m/z of the eluting ions.

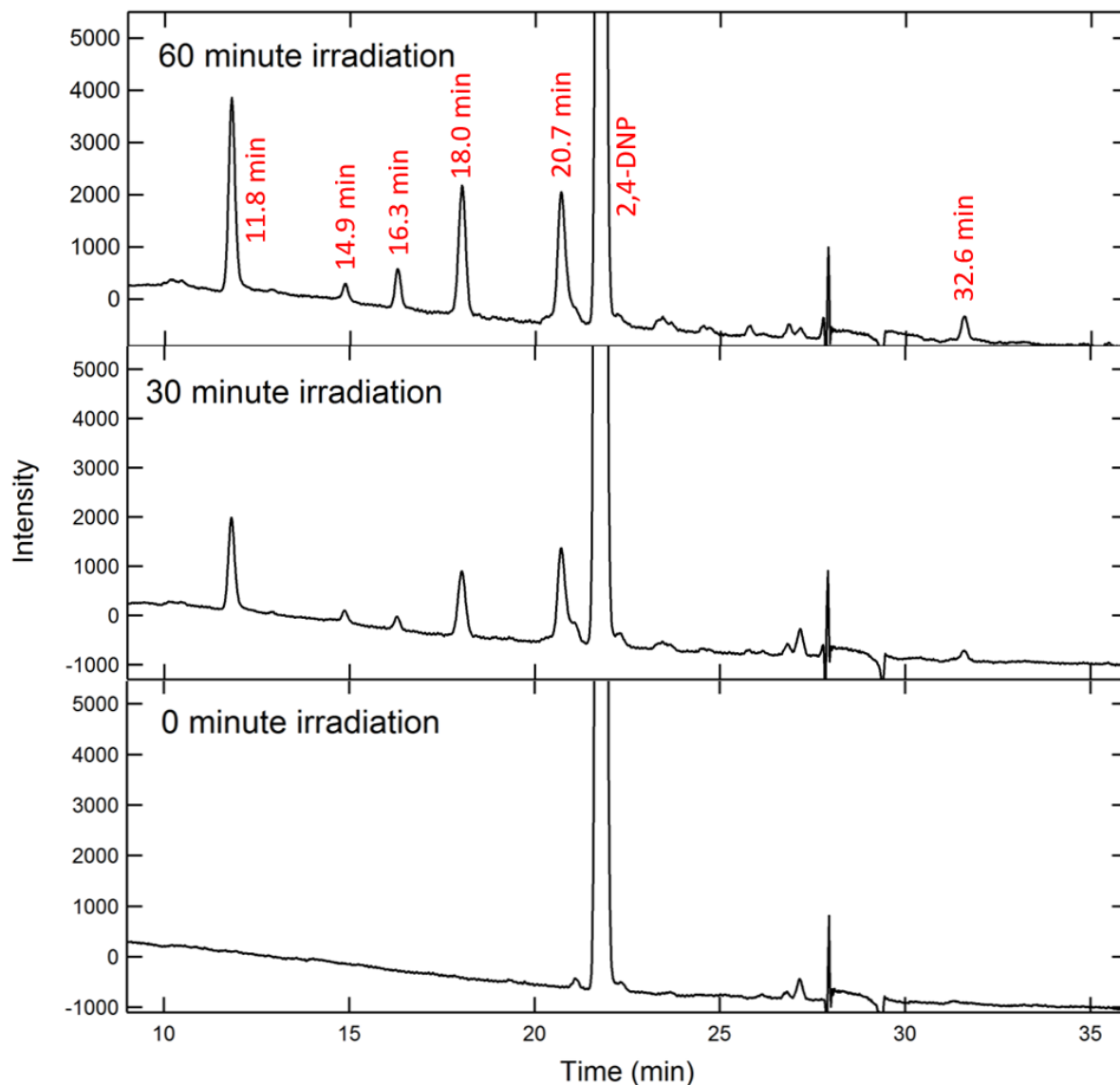


Figure A.6. PDA chromatogram of the observed photolysis products. This is a sample chromatogram corresponding to 350-500 nm integrated PDA absorbance. There are clear peaks growing at 11.8, 14.9, 16.3, 18.0, 20.7 and 32.6 min in the chromatogram during photolysis. The 11.8, 18.0 and 20.7 min peaks have the correct absorption spectrum characteristics (the corresponding spectra given below) for the expected products, which absorb to the red of 2,4-DNP. The 16.3 min peak is very weak.

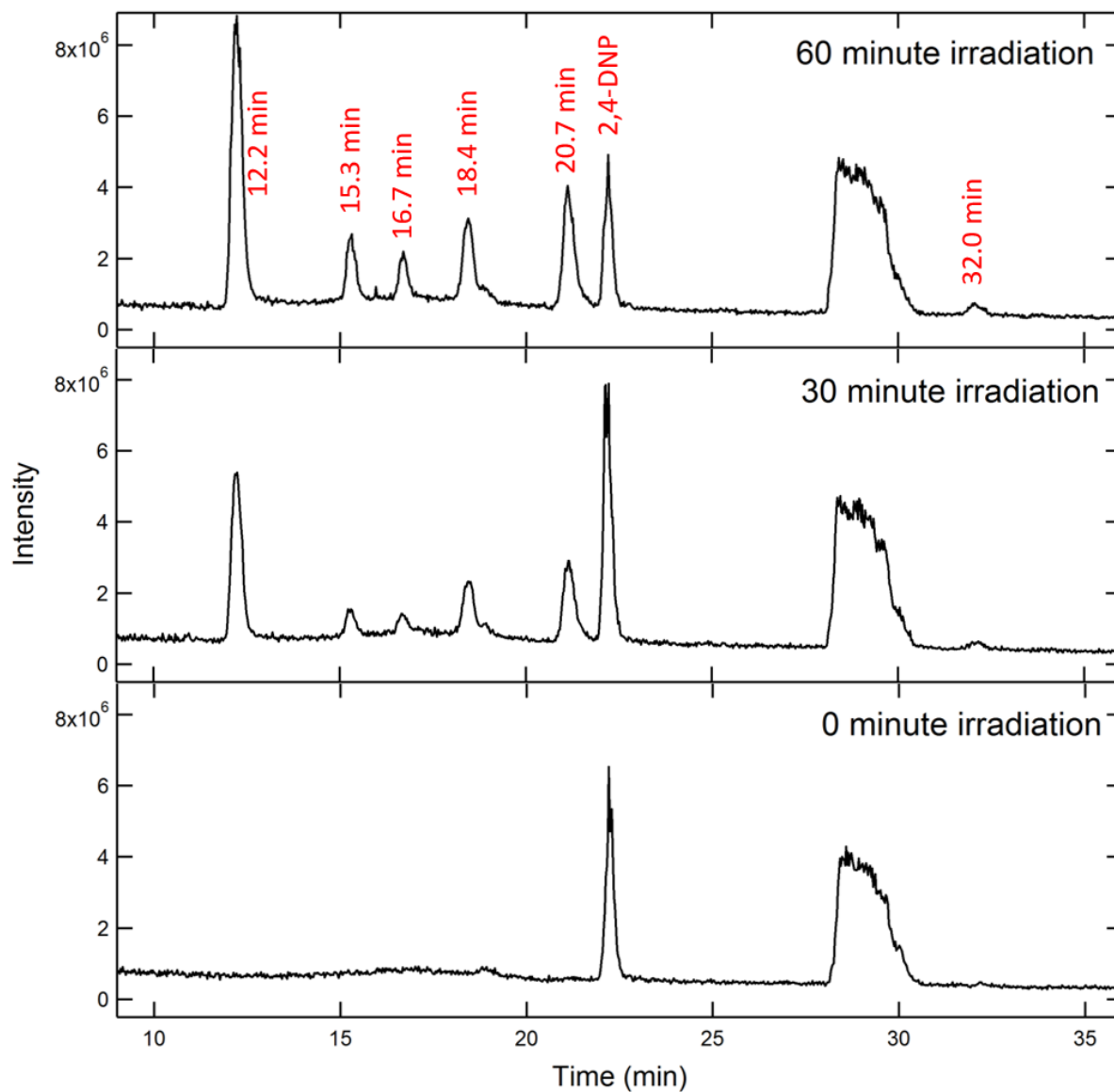


Figure A.7. MS chromatograms at different photolysis times. In the MS chromatograms integrated over the 150-170 m/z range, where the majority of products are expected, there is a clear growth of several peaks during photolysis.

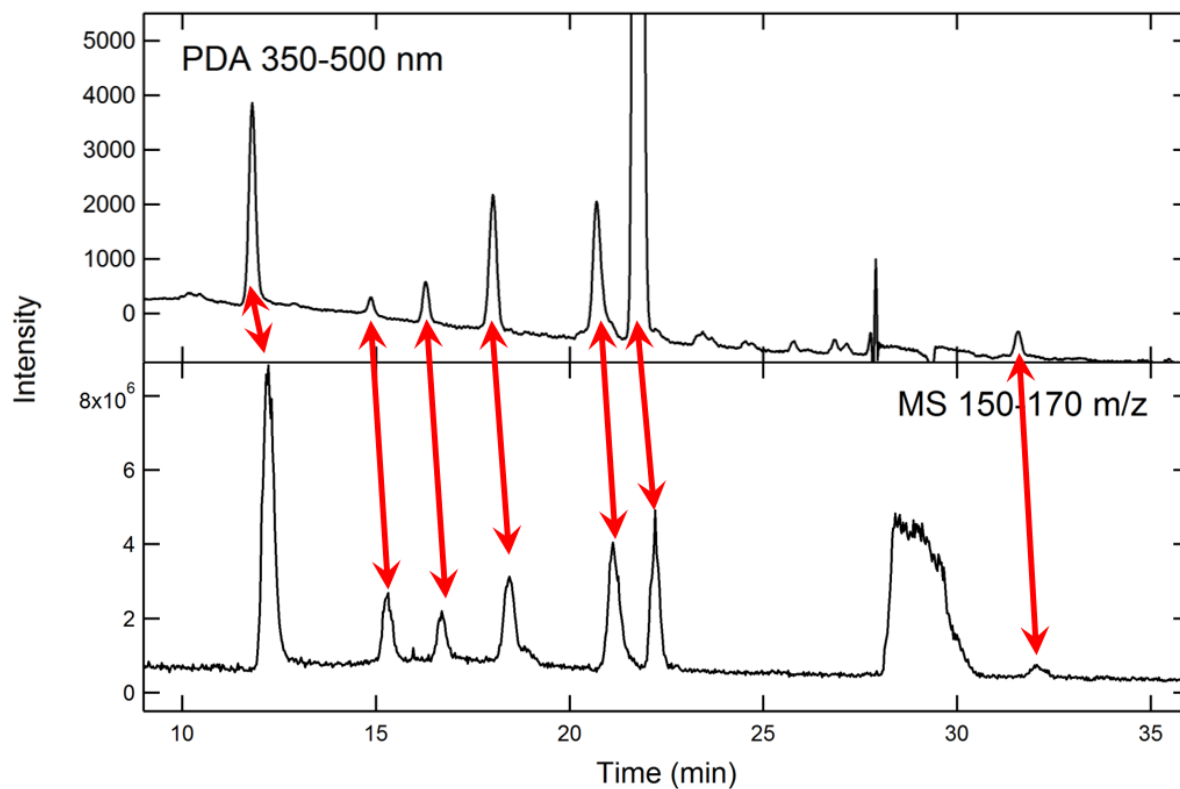
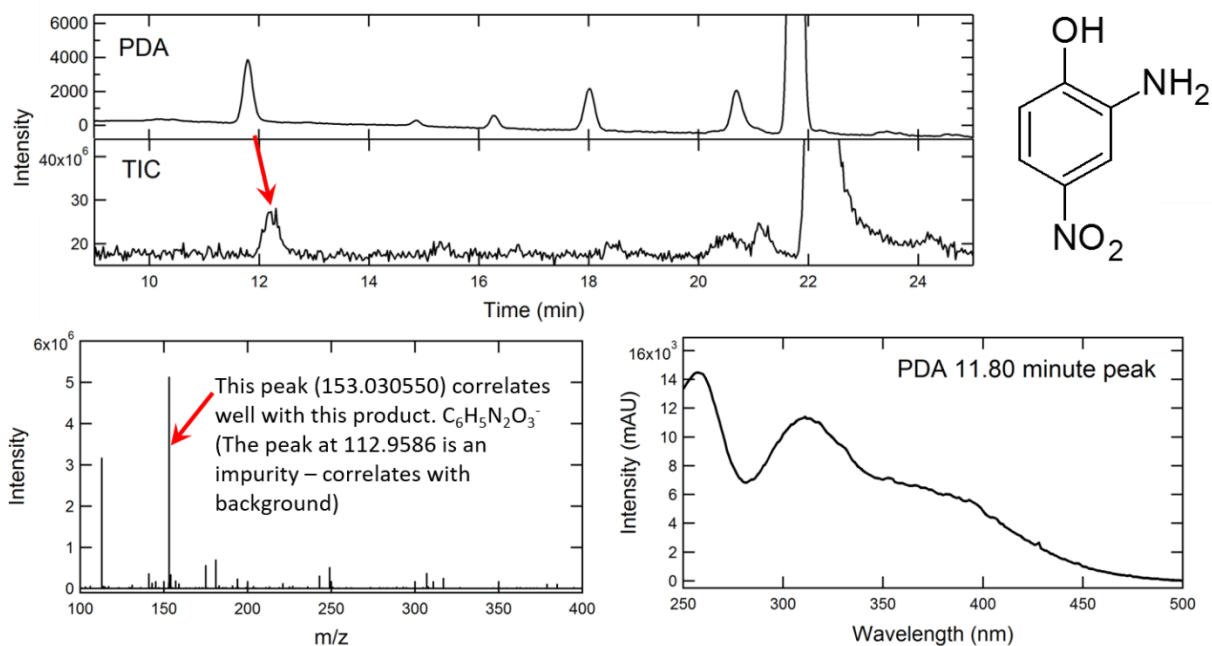
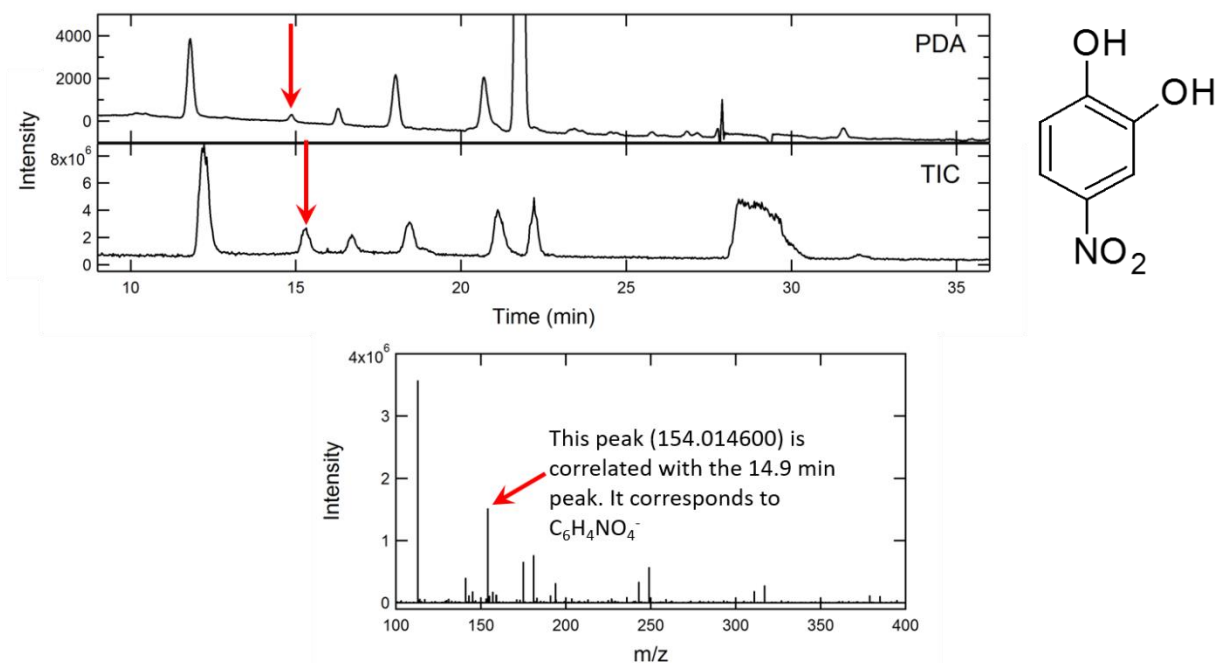


Figure A.8. PDA vs. MS Chromatogram for the 60 min photolyzed sample. The correlation between the MS and PDA chromatograms are shown by the red arrows. The MS chromatogram corresponds to an integration over the 150-170 m/z range. These peaks are also discernible in the TIC spectrum but they are easier to observe in this integration range. The peaks in the MS chromatogram are delayed relative to the corresponding peaks in the PDA chromatogram by about 0.4 min (the time needed for the slow to migrate from the PDA cell into the ESI source).



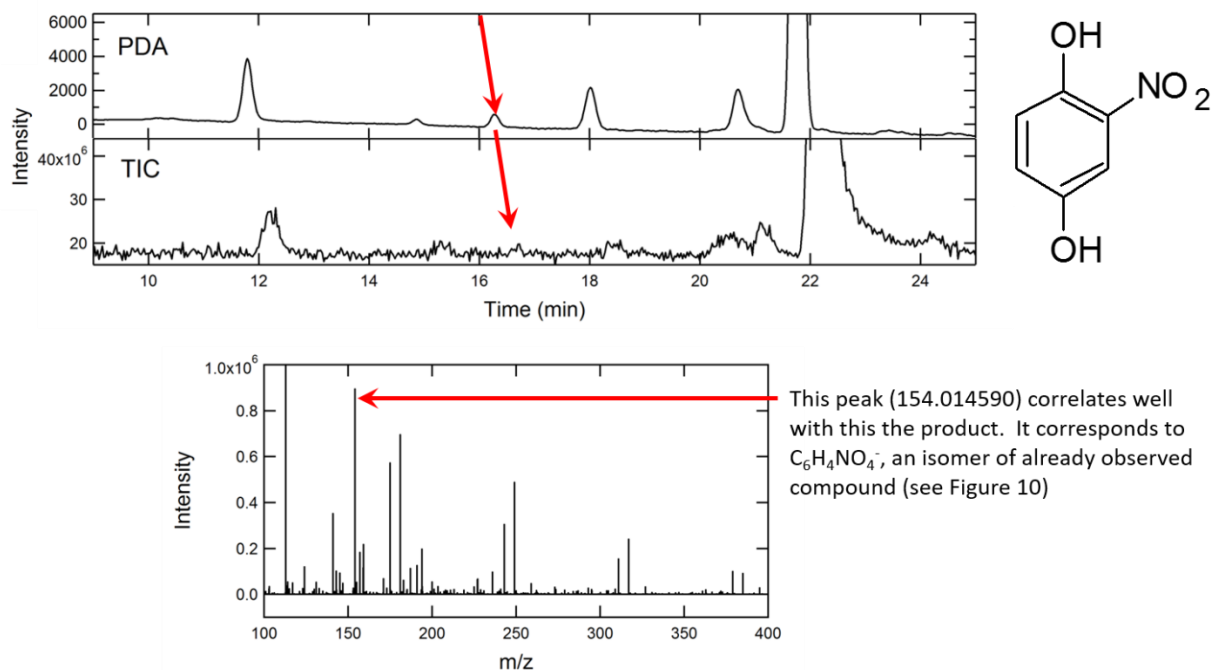
Peak Report for $m/z = 153.030550 \pm 2.0$ ppm
 C6 H5 N2 O3 $m/z = 153.030566 - 0.1$ ppm DBE = 6.0

Figure A.9. Chromatograms, mass spectrum, and absorption spectrum for the 11.8 min peak. The 11.8 min peak in the PDA chromatogram correlates with the 12.3 min peak in the MS chromatogram.



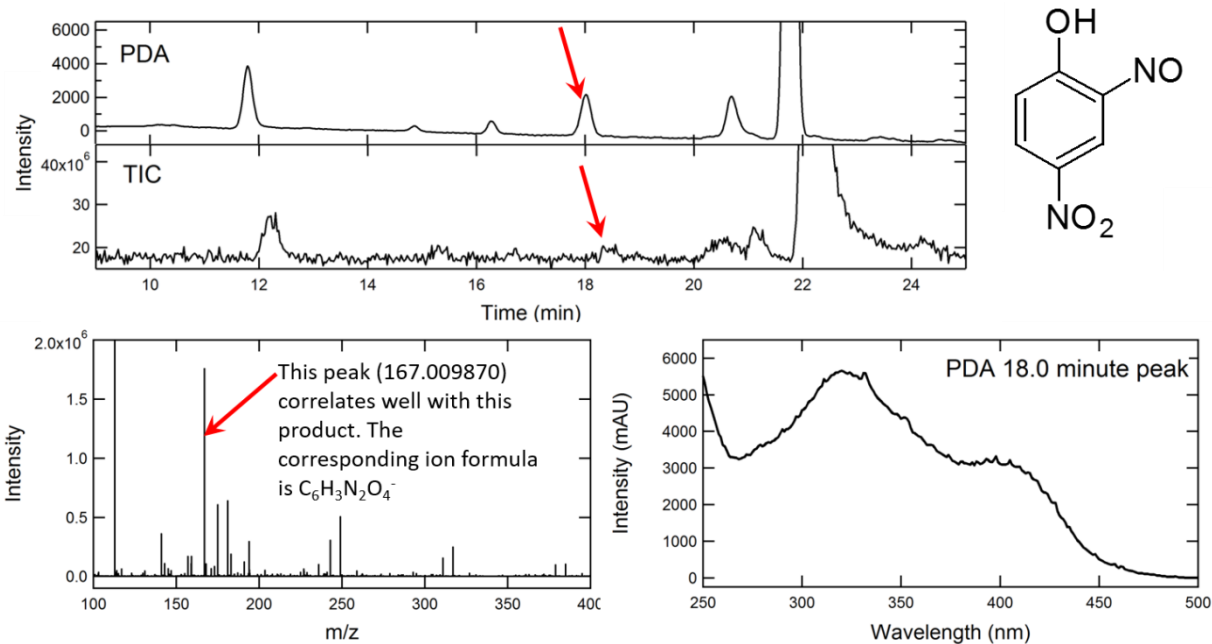
Peak Report for $m/z = 154.014600 \pm 2.0$ ppm
 C6 H4 N1 O4 $m/z = 154.014581 \pm 0.1$ ppm DBE = 6.0

Figure A.10. Chromatograms, mass spectrum, and absorption spectrum for the 14.9 min peak. The 14.9 min peak in the PDA chromatogram correlates with the 15.3 min peak in the MS chromatogram.



Peak Report for m/z = 154.014590 +/-3.0 ppm
 C6 H4 N1 O4 m/z = 154.014581 +0.1 ppm DBE = 6.0

Figure A.11. Chromatograms, mass spectrum, and absorption spectrum for the 16.3 min peak. The 16.3 min peak in the PDA chromatogram correlates with the 16.7 min peak in the MS chromatogram.



Peak Report for $m/z = 167.009870 \pm 2.0$ ppm
 C6 H3 N2 O4 $m/z = 167.009830 \pm 0.2$ ppm DBE = 7.0

Figure A.12. Chromatograms, mass spectrum, and absorption spectrum for the 18.0 min peak. The 18.0 min peak in the PDA chromatogram correlates with the 18.4 min peak in the MS chromatogram.

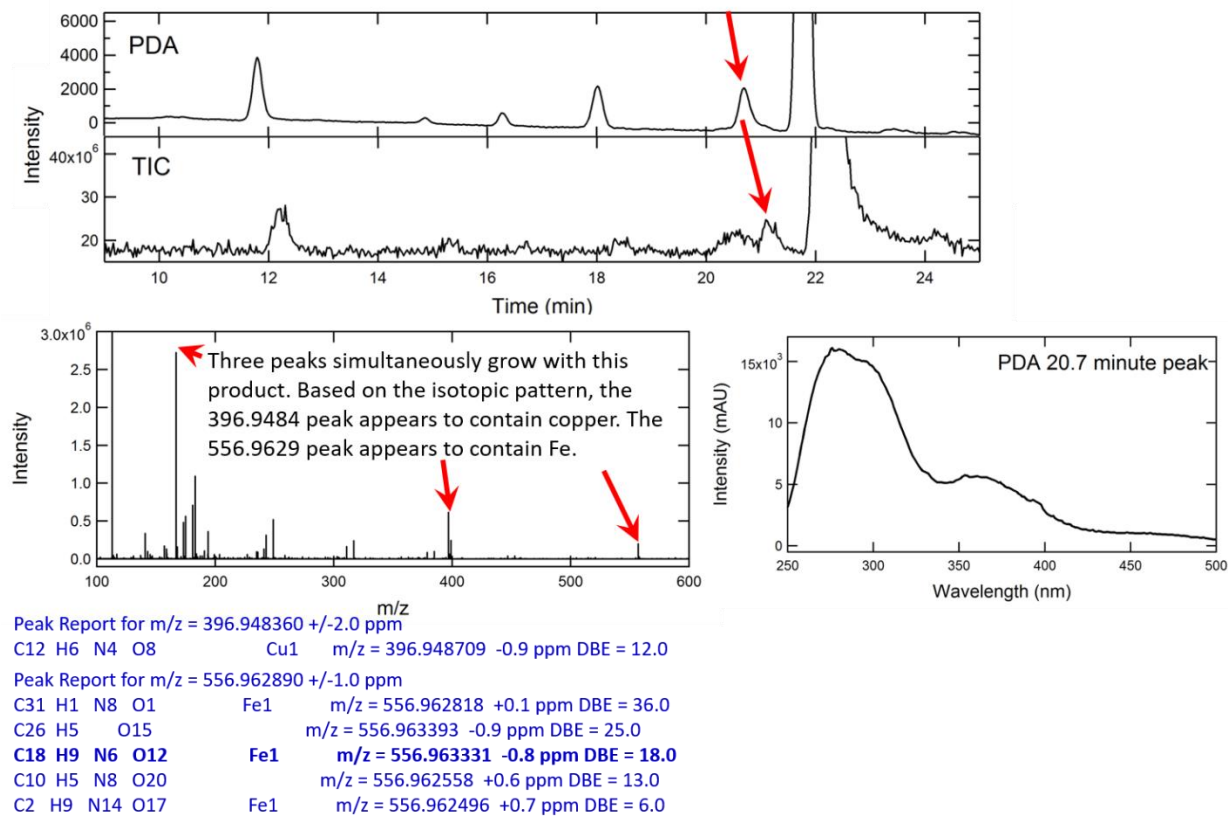
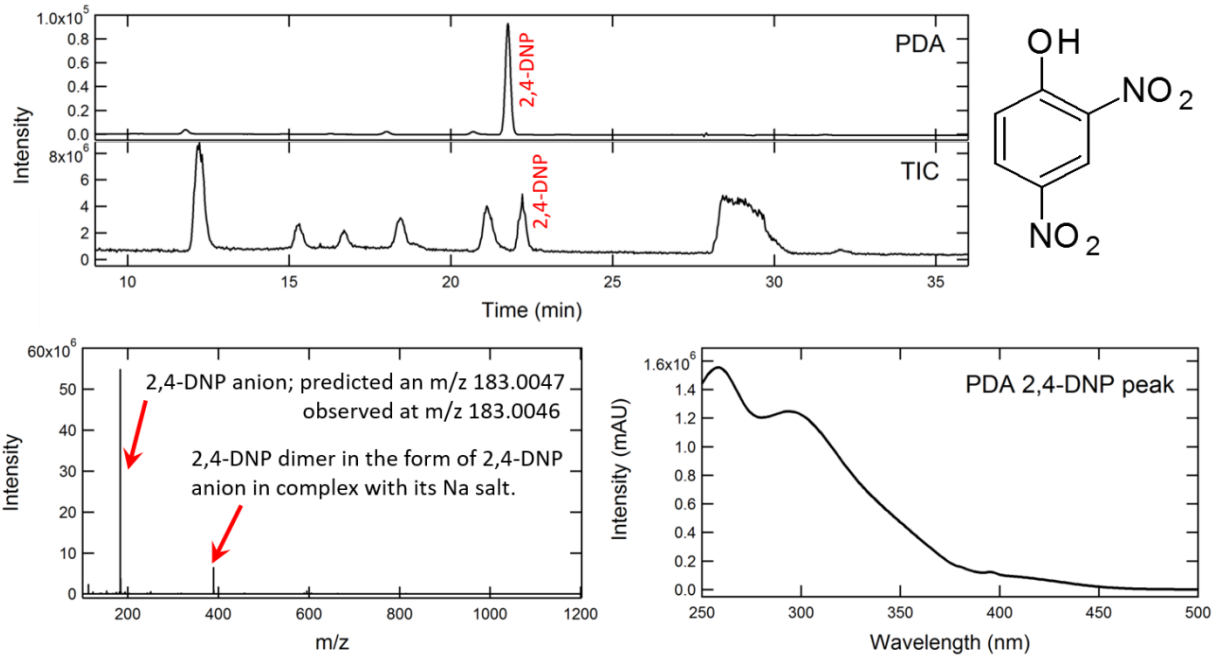


Figure A.13. Chromatograms, mass spectrum, and absorption spectrum for the 20.7 min peak. The 20.7 min peak in the PDA chromatogram correlates with the 21.2 min peak in the MS chromatogram.



Peak Report for m/z = 183.004600 +/-2.0 ppm
 C6 H3 N2 O5 m/z = 183.004745 -0.8 ppm DBE = 7.0

Peak Report for m/z = 388.998300 +/-2.0 ppm
 C12 H6 N4 O10 Na1 m/z = 388.998710 -1.1 ppm DBE = 12.0
 C10 H1 N10 O8 m/z = 388.998431 -0.3 ppm DBE = 16.0

Figure A.14. Chromatograms, mass spectrum, and absorption spectrum for 2,4-DNP.

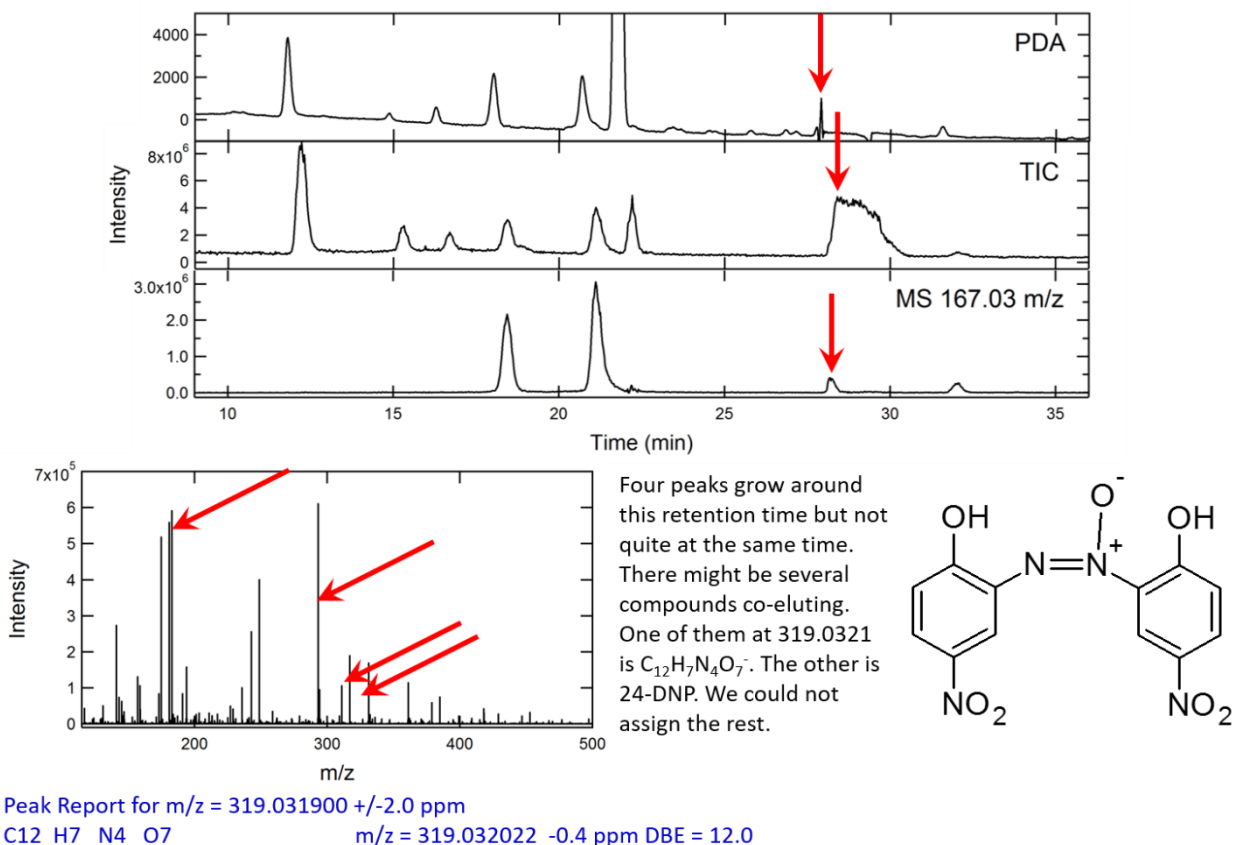
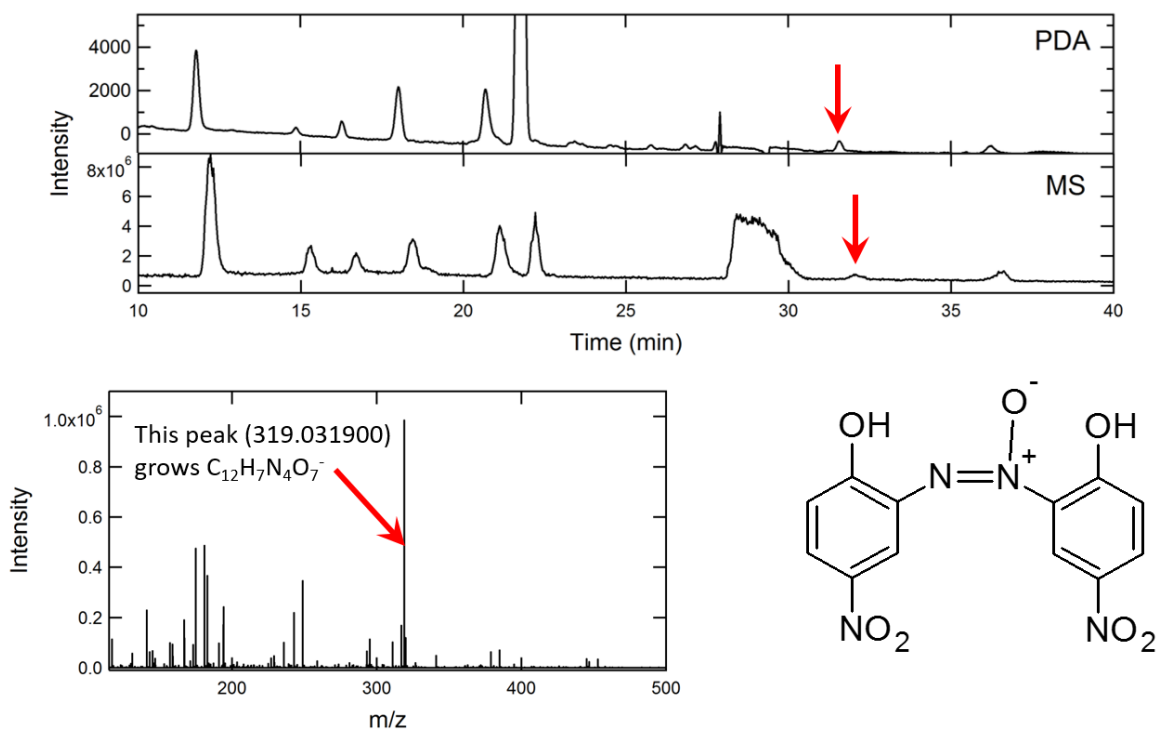


Figure A.15. Chromatograms, mass spectrum, and absorption spectrum for the 27.9 min peak. The 27.9 min peak in the PDA chromatogram correlates to the 28.2 min peak in the MS chromatogram.



Peak Report for m/z = 319.031900 +/-2.0 ppm

C12 H7 N4 O7

m/z = 319.032022 -0.4 ppm DBE = 12.0

Figure A.16. Chromatograms, mass spectrum, and absorption spectrum for the 31.6 min peak. The 31.6 min peak in the PDA chromatogram correlates to the 32.1 min peak in the MS chromatogram.

Table A.1. Summary of the compounds detected in LC-PDA-MS experiments.

Retention time (min) in PDA	Retention time (min) in MS	Description of absorption spectrum observed by PDA	Major m/z values (negative ions) correlating with the eluted peak	Formula (neutral compound unless indicated)	Assignment comments
-	7.8	-	138.0197	C ₆ H ₅ O ₃ N	Loss of -NO ₂ very small peak
11.8	12.2	280-460 nm broad spectrum	153.03055	C ₆ H ₆ O ₃ N ₂	Conversion of -NO ₂ to -NH ₂
14.9	15.3	320 nm broad spectrum	154.0146	C ₆ H ₅ O ₄ N	Conversion of -NO ₂ to -OH
16.3	16.7	270 nm peak	154.01459	C ₆ H ₅ O ₄ N	Conversion of -NO ₂ to -OH
18	18.4	260-440 nm broad spectrum	167.00987	C ₆ H ₄ O ₄ N ₂	Conversion of -NO ₂ to -NO
-	19.0	-	138.0197	C ₆ H ₅ O ₃ N	Loss of -NO ₂ very small peak
20.7	21.2	260-440 nm broad spectrum	167.00987 183.0047 396.94836 556.96289	C ₆ H ₄ O ₄ N ₂ C ₆ H ₄ O ₅ N ₂ <i>Ion</i> C ₁₂ H ₆ N ₄ O ₈ Cu ⁻ <i>Ion</i> C ₁₈ H ₉ N ₆ O ₁₂ Fe ⁻	The first two peaks are from a nitroso compound and from DNP. The other two have metals in them, likely impurities in ESI .
21.8	22.2	2,4-DNP; absorbing where it should	183.0046 388.9989	C ₆ H ₄ O ₅ N ₂ <i>Ion</i> C ₁₂ H ₆ O ₁₀ N ₄ Na ⁻	2,4-DNP [Na salt of 2,4-DNP] complexed to 2,4-DNP
27.9	28.2	An impurity absorbing at 280 nm	Several masses; one of them is 319.0319		
32.6	32.1	-	319.0319	C ₁₂ H ₈ N ₄ O ₇	This is not a weakly-bound dimer; it is a proper ion

REFERENCES

1. Charlson, R. J.; Schwartz, S. E.; Hales, J. M.; Cess, R. D.; Coakley, J. A.; Hansen, J. E.; Hofmann, D. J., Climate Forcing by Anthropogenic Aerosols. *Science* **1992**, 255 (5043), 423-430.
2. Ghan, S. J.; Schwartz, S. E., Aerosol Properties and Processes: A Path from Field and Laboratory Measurements to Global Climate Models. *Bulletin of the American Meteorological Society* **2007**, 88 (7), 1059-1083.
3. Haywood, J.; Boucher, O., Estimates of the direct and indirect radiative forcing due to tropospheric aerosols: A review. *Reviews of Geophysics* **2000**, 38 (4), 513-543.
4. Andreae, M. O.; Gelencsér, A., Black carbon or brown carbon? The nature of light-absorbing carbonaceous aerosols. *Atmos. Chem. Phys.* **2006**, 6 (10), 3131-3148.
5. Bond, T. C.; Sun, H., Can Reducing Black Carbon Emissions Counteract Global Warming? *Environmental Science & Technology* **2005**, 39 (16), 5921-5926.
6. Ramanathan, V.; Ramana, M. V.; Roberts, G.; Kim, D.; Corrigan, C.; Chung, C.; Winker, D., Warming trends in Asia amplified by brown cloud solar absorption. *Nature* **2007**, 448 (7153), 575-578.
7. Brook, R. D.; Rajagopalan, S.; Pope, C. A.; Brook, J. R.; Bhatnagar, A.; Diez-Roux, A. V.; Holguin, F.; Hong, Y.; Luepker, R. V.; Mittleman, M. A.; Peters, A.; Siscovick, D.; Smith, S. C.; Whitsel, L.; Kaufman, J. D., Particulate Matter Air Pollution and Cardiovascular Disease. *An Update to the Scientific Statement From the American Heart Association* **2010**, 121 (21), 2331-2378.
8. Pope, I. C.; Burnett, R. T.; Thun, M. J.; et al., Lung cancer, cardiopulmonary mortality, and long-term exposure to fine particulate air pollution. *JAMA* **2002**, 287 (9), 1132-1141.
9. Pope, C. A. I.; Ezzati, M.; Dockery, D. W., Fine-Particulate Air Pollution and Life Expectancy in the United States. *New England Journal of Medicine* **2009**, 360 (4), 376-386.
10. Zimmermann, R., Ambient aerosols and human health: working towards a combined analytical and toxicological approach. *Analytical and Bioanalytical Chemistry* **2011**, 401 (10), 3041-3044.
11. Nel, A., Air Pollution-Related Illness: Effects of Particles. *Science* **2005**, 308 (5723), 804-806.
12. Shiraiwa, M.; Selzle, K.; Pöschl, U., Hazardous components and health effects of atmospheric aerosol particles: reactive oxygen species, soot, polycyclic aromatic compounds and allergenic proteins. *Free Radical Research* **2012**, 46 (8), 927-939.

13. Dockery , D. W.; Pope , C. A.; Xu , X.; Spengler , J. D.; Ware , J. H.; Fay , M. E.; Ferris , B. G. J.; Speizer , F. E., An Association between Air Pollution and Mortality in Six U.S. Cities. *New England Journal of Medicine* **1993**, 329 (24), 1753-1759.
14. Huang, R.-J.; Zhang, Y.; Bozzetti, C.; Ho, K.-F.; Cao, J.-J.; Han, Y.; Daellenbach, K. R.; Slowik, J. G.; Platt, S. M.; Canonaco, F.; Zotter, P.; Wolf, R.; Pieber, S. M.; Brun, E. A.; Crippa, M.; Ciarelli, G.; Piazzalunga, A.; Schwikowski, M.; Abbaszade, G.; Schnelle-Kreis, J.; Zimmermann, R.; An, Z.; Szidat, S.; Baltensperger, U.; Haddad, I. E.; Prevot, A. S. H., High secondary aerosol contribution to particulate pollution during haze events in China. *Nature* **2014**, 514 (7521), 218-222.
15. Sisler, J. F.; Malm, W. C., The relative importance of soluble aerosols to spatial and seasonal trends of impaired visibility in the United States. *Atmospheric Environment* **1994**, 28 (5), 851-862.
16. Finlayson-Pitts, B. J.; Pitts Jr, J. N., Chapter 2 - The Atmospheric System. In *Chemistry of the Upper and Lower Atmosphere*, Academic Press: San Diego, 2000; pp 15-42.
17. Kanakidou, M.; Seinfeld, J. H.; Pandis, S. N.; Barnes, I.; Dentener, F. J.; Facchini, M. C.; Van Dingenen, R.; Ervens, B.; Nenes, A.; Nielsen, C. J.; Swietlicki, E.; Putaud, J. P.; Balkanski, Y.; Fuzzi, S.; Horth, J.; Moortgat, G. K.; Winterhalter, R.; Myhre, C. E. L.; Tsigaridis, K.; Vignati, E.; Stephanou, E. G.; Wilson, J., Organic aerosol and global climate modelling: a review. *Atmos. Chem. Phys.* **2005**, 5 (4), 1053-1123.
18. Putaud, J. P.; Van Dingenen, R.; Alastuey, A.; Bauer, H.; Birmili, W.; Cyrys, J.; Flentje, H.; Fuzzi, S.; Gehrig, R.; Hansson, H. C.; Harrison, R. M.; Herrmann, H.; Hitzenberger, R.; Hüglin, C.; Jones, A. M.; Kasper-Giebl, A.; Kiss, G.; Kousa, A.; Kuhlbusch, T. A. J.; Lössch, G.; Maenhaut, W.; Molnar, A.; Moreno, T.; Pekkanen, J.; Perrino, C.; Pitz, M.; Puxbaum, H.; Querol, X.; Rodriguez, S.; Salma, I.; Schwarz, J.; Smolik, J.; Schneider, J.; Spindler, G.; ten Brink, H.; Tursic, J.; Viana, M.; Wiedensohler, A.; Raes, F., A European aerosol phenomenology – 3: Physical and chemical characteristics of particulate matter from 60 rural, urban, and kerbside sites across Europe. *Atmospheric Environment* **2010**, 44 (10), 1308-1320.
19. Minguillón, M. C.; Querol, X.; Baltensperger, U.; Prévôt, A. S. H., Fine and coarse PM composition and sources in rural and urban sites in Switzerland: Local or regional pollution? *Science of The Total Environment* **2012**, 427–428, 191-202.
20. Robinson, A. L.; Donahue, N. M.; Shrivastava, M. K.; Weitkamp, E. A.; Sage, A. M.; Grieshop, A. P.; Lane, T. E.; Pierce, J. R.; Pandis, S. N., Rethinking Organic Aerosols: Semivolatile Emissions and Photochemical Aging. *Science* **2007**, 315 (5816), 1259-1262.
21. Pankow, J. F., An absorption model of gas/particle partitioning of organic compounds in the atmosphere. *Atmospheric Environment* **1994**, 28 (2), 185-188.
22. Odum, J. R.; Hoffmann, T.; Bowman, F.; Collins, D.; Flagan, R. C.; Seinfeld, J. H., Gas/Particle Partitioning and Secondary Organic Aerosol Yields. *Environmental Science & Technology* **1996**, 30 (8), 2580-2585.

23. Went, F., Organic matter in the atmosphere, and its possible relation to petroleum formation. *Proceedings of the National Academy of Sciences* **1960**, *46* (2), 212-221.
24. Herrmann, H.; Schaefer, T.; Tilgner, A.; Styler, S. A.; Weller, C.; Teich, M.; Otto, T., Tropospheric Aqueous-Phase Chemistry: Kinetics, Mechanisms, and Its Coupling to a Changing Gas Phase. *Chemical Reviews* **2015**, *115* (10), 4259-4334.
25. Pöschl, U.; Shiraiwa, M., Multiphase Chemistry at the Atmosphere–Biosphere Interface Influencing Climate and Public Health in the Anthropocene. *Chemical Reviews* **2015**, *115* (10), 4440-4475.
26. Guenther, A.; Karl, T.; Harley, P.; Wiedinmyer, C.; Palmer, P. I.; Geron, C., Estimates of global terrestrial isoprene emissions using MEGAN (Model of Emissions of Gases and Aerosols from Nature). *Atmos. Chem. Phys.* **2006**, *6* (11), 3181-3210.
27. Sindelarova, K.; Granier, C.; Bouarar, I.; Guenther, A.; Tilmes, S.; Stavrou, T.; Müller, J. F.; Kuhn, U.; Stefani, P.; Knorr, W., Global data set of biogenic VOC emissions calculated by the MEGAN model over the last 30 years. *Atmos. Chem. Phys.* **2014**, *14* (17), 9317-9341.
28. Geron, C.; Rasmussen, R.; R. Arnts, R.; Guenther, A., A review and synthesis of monoterpene speciation from forests in the United States. *Atmospheric Environment* **2000**, *34* (11), 1761-1781.
29. Pandis, S. N.; Paulson, S. E.; Seinfeld, J. H.; Flagan, R. C., Aerosol formation in the photooxidation of isoprene and β -pinene. *Atmospheric Environment. Part A. General Topics* **1991**, *25* (5), 997-1008.
30. Carlton, A. G.; Wiedinmyer, C.; Kroll, J. H., A review of Secondary Organic Aerosol (SOA) formation from isoprene. *Atmos. Chem. Phys.* **2009**, *9* (14), 4987-5005.
31. Pandis, S. N.; Harley, R. A.; Cass, G. R.; Seinfeld, J. H., Secondary organic aerosol formation and transport. *Atmospheric Environment. Part A. General Topics* **1992**, *26* (13), 2269-2282.
32. Hoffmann, T.; Odum, J. R.; Bowman, F.; Collins, D.; Klockow, D.; Flagan, R. C.; Seinfeld, J. H., Formation of Organic Aerosols from the Oxidation of Biogenic Hydrocarbons. *Journal of Atmospheric Chemistry* **1997**, *26* (2), 189-222.
33. Griffin, R. J.; Cocker, D. R.; Flagan, R. C.; Seinfeld, J. H., Organic aerosol formation from the oxidation of biogenic hydrocarbons. *Journal of Geophysical Research: Atmospheres* **1999**, *104* (D3), 3555-3567.
34. Finlayson-Pitts, B. J.; Pitts Jr, J. N., Chapter 9 - Particles in the Troposphere. In *Chemistry of the Upper and Lower Atmosphere*, Academic Press: San Diego, 2000; pp 349-435.
35. Street, R. A.; Owen, S.; Duckham, S. C.; Boissard, C.; Hewitt, C. N., Effect of habitat and age on variations in volatile organic compound (VOC) emissions from *Quercus ilex* and *Pinus pinea*. *Atmospheric Environment* **1997**, *31*, 89-100.

36. Guenther, A.; Zimmerman, P.; Wildermuth, M., Natural volatile organic compound emission rate estimates for U.S. woodland landscapes. *Atmospheric Environment* **1994**, *28* (6), 1197-1210.
37. Piccot, S. D.; Watson, J. J.; Jones, J. W., A global inventory of volatile organic compound emissions from anthropogenic sources. *Journal of Geophysical Research: Atmospheres* **1992**, *97* (D9), 9897-9912.
38. Izumi, K.; Fukuyama, T., Photochemical aerosol formation from aromatic hydrocarbons in the presence of NO_x. *Atmospheric Environment. Part A. General Topics* **1990**, *24* (6), 1433-1441.
39. Romonosky, D. E.; Laskin, A.; Laskin, J.; Nizkorodov, S. A., High-Resolution Mass Spectrometry and Molecular Characterization of Aqueous Photochemistry Products of Common Types of Secondary Organic Aerosols. *The Journal of Physical Chemistry A* **2015**, *119* (11), 2594-2606.
40. Kourtchev, I.; Fuller, S. J.; Giorio, C.; Healy, R. M.; Wilson, E.; O'Connor, I.; Wenger, J. C.; McLeod, M.; Aalto, J.; Ruuskanen, T. M.; Maenhaut, W.; Jones, R.; Venables, D. S.; Sodeau, J. R.; Kulmala, M.; Kalberer, M., Molecular composition of biogenic secondary organic aerosols using ultrahigh-resolution mass spectrometry: comparing laboratory and field studies. *Atmos. Chem. Phys.* **2014**, *14* (4), 2155-2167.
41. Schmitt-Kopplin, P.; Gelencsér, A.; Dabek-Zlotorzynska, E.; Kiss, G.; Hertkorn, N.; Harir, M.; Hong, Y.; Gebefügi, I., Analysis of the Unresolved Organic Fraction in Atmospheric Aerosols with Ultrahigh-Resolution Mass Spectrometry and Nuclear Magnetic Resonance Spectroscopy: Organosulfates As Photochemical Smog Constituents. *Analytical Chemistry* **2010**, *82* (19), 8017-8026.
42. Putman, A. L.; Offenberg, J. H.; Fisseha, R.; Kundu, S.; Rahn, T. A.; Mazzoleni, L. R., Ultrahigh-resolution FT-ICR mass spectrometry characterization of α -pinene ozonolysis SOA. *Atmospheric Environment* **2012**, *46*, 164-172.
43. Rudich, Y.; Donahue, N. M.; Mentel, T. F., Aging of Organic Aerosol: Bridging the Gap Between Laboratory and Field Studies. *Annual Review of Physical Chemistry* **2007**, *58* (1), 321-352.
44. George, C.; Ammann, M.; D'Anna, B.; Donaldson, D. J.; Nizkorodov, S. A., Heterogeneous Photochemistry in the Atmosphere. *Chemical Reviews* **2015**, *115* (10), 4218-4258.
45. Kroll, J. H.; Seinfeld, J. H., Chemistry of secondary organic aerosol: Formation and evolution of low-volatility organics in the atmosphere. *Atmospheric Environment* **2008**, *42* (16), 3593-3624.
46. Hinks, M. L.; Brady, M. V.; Lignell, H.; Song, M.; Grayson, J. W.; Bertram, A. K.; Lin, P.; Laskin, A.; Laskin, J.; Nizkorodov, S. A., Effect of viscosity on photodegradation rates in complex secondary organic aerosol materials. *Physical Chemistry Chemical Physics* **2016**, *18* (13), 8785-8793.

47. Romonosky, D. E.; Ali, N. N.; Saiduddin, M. N.; Wu, M.; Lee, H. J.; Aiona, P. K.; Nizkorodov, S. A., Effective absorption cross sections and photolysis rates of anthropogenic and biogenic secondary organic aerosols. *Atmospheric Environment* **2016**, *130*, 172-179.
48. Lee, H. J.; Aiona, P. K.; Laskin, A.; Laskin, J.; Nizkorodov, S. A., Effect of Solar Radiation on the Optical Properties and Molecular Composition of Laboratory Proxies of Atmospheric Brown Carbon. *Environmental Science & Technology* **2014**, *48* (17), 10217-10226.
49. Zhao, R.; Lee, A. K. Y.; Huang, L.; Li, X.; Yang, F.; Abbatt, J. P. D., Photochemical processing of aqueous atmospheric brown carbon. *Atmos. Chem. Phys. Discuss.* **2015**, *15* (2), 2957-2996.
50. Epstein, S. A.; Blair, S. L.; Nizkorodov, S. A., Direct Photolysis of α -Pinene Ozonolysis Secondary Organic Aerosol: Effect on Particle Mass and Peroxide Content. *Environmental Science & Technology* **2014**, *48* (19), 11251-11258.
51. Kroll, J. H.; Ng, N. L.; Murphy, S. M.; Flagan, R. C.; Seinfeld, J. H., Secondary Organic Aerosol Formation from Isoprene Photooxidation. *Environmental Science & Technology* **2006**, *40* (6), 1869-1877.
52. Romonosky, D. E.; Nguyen, L. Q.; Shemesh, D.; Nguyen, T. B.; Epstein, S. A.; Martin, D. B. C.; Vanderwal, C. D.; Gerber, R. B.; Nizkorodov, S. A., Absorption spectra and aqueous photochemistry of β -hydroxyalkyl nitrates of atmospheric interest. *Molecular Physics* **2015**, *113* (15-16), 2179-2190.
53. Malecha, K. T.; Nizkorodov, S. A., Photodegradation of Secondary Organic Aerosol Particles as a Source of Small, Oxygenated Volatile Organic Compounds. *Environmental Science & Technology* **2016**, *50* (18), 9990-9997.
54. Romonosky, D. E.; Li, Y.; Shiraiwa, M.; Laskin, A.; Laskin, J.; Nizkorodov, S. A., Aqueous Photochemistry of Secondary Organic Aerosol of α -Pinene and α -Humulene Oxidized with Ozone, Hydroxyl Radical, and Nitrate Radical. *The Journal of Physical Chemistry A* **2017**, 1298-1309.
55. Walser, M. L.; Park, J.; Gomez, A. L.; Russell, A. R.; Nizkorodov, S. A., Photochemical Aging of Secondary Organic Aerosol Particles Generated from the Oxidation of d-Limonene. *The Journal of Physical Chemistry A* **2007**, *111* (10), 1907-1913.
56. Surratt, J. D.; Murphy, S. M.; Kroll, J. H.; Ng, N. L.; Hildebrandt, L.; Sorooshian, A.; Szmigielski, R.; Vermeylen, R.; Maenhaut, W.; Claeys, M.; Flagan, R. C.; Seinfeld, J. H., Chemical Composition of Secondary Organic Aerosol Formed from the Photooxidation of Isoprene. *The Journal of Physical Chemistry A* **2006**, *110* (31), 9665-9690.
57. Rothfuss, N. E.; Petters, M. D., Characterization of the temperature and humidity-dependent phase diagram of amorphous nanoscale organic aerosols. *Physical Chemistry Chemical Physics* **2017**, *19* (9), 6532-6545.

58. Kidd, C.; Perraud, V.; Wingen, L. M.; Finlayson-Pitts, B. J., Integrating phase and composition of secondary organic aerosol from the ozonolysis of α -pinene. *Proceedings of the National Academy of Sciences* **2014**, *111* (21), 7552-7557.
59. Koop, T.; Bookhold, J.; Shiraiwa, M.; Poeschl, U., Glass transition and phase state of organic compounds: dependency on molecular properties and implications for secondary organic aerosols in the atmosphere. *Phys. Chem. Chem. Phys.* **2011**, *13* (43), 19238-19255.
60. Renbaum-Wolff, L.; Grayson, J. W.; Bateman, A. P.; Kuwata, M.; Sellier, M.; Murray, B. J.; Shilling, J. E.; Martin, S. T.; Bertram, A. K., Viscosity of α -pinene secondary organic material and implications for particle growth and reactivity. *Proc. Natl. Acad. Sci. U. S. A.* **2013**, *110* (20), 8014-8019.
61. Virtanen, A.; Joutsensaari, J.; Koop, T.; Kannosto, J.; Yli-Pirila, P.; Leskinen, J.; Makela, J. M.; Holopainen, J. K.; Poeschl, U.; Kulmala, M.; Worsnop, D. R.; Laaksonen, A., An amorphous solid state of biogenic secondary organic aerosol particles. *Nature* **2010**, *467* (7317), 824-827.
62. Bateman, A. P.; Bertram, A. K.; Martin, S. T., Hygroscopic Influence on the Semisolid-to-Liquid Transition of Secondary Organic Materials. *The Journal of Physical Chemistry A* **2015**, *119* (19), 4386-4395.
63. Perraud, V.; Bruns, E. A.; Ezell, M. J.; Johnson, S. N.; Yu, Y.; Alexander, M. L.; Zelenyuk, A.; Imre, D.; Chang, W. L.; Dabdub, D.; Pankow, J. F.; Finlayson-Pitts, B. J., Nonequilibrium atmospheric secondary organic aerosol formation and growth. *Proceedings of the National Academy of Sciences* **2012**, 2836-2841.
64. Bones, D. L.; Reid, J. P.; Lienhard, D. M.; Krieger, U. K., Comparing the mechanism of water condensation and evaporation in glassy aerosol. *Proceedings of the National Academy of Sciences* **2012**, *109* (29), 11613-11618.
65. Power, R. M.; Simpson, S. H.; Reid, J. P.; Hudson, A. J., The transition from liquid to solid-like behaviour in ultrahigh viscosity aerosol particles. *Chemical Science* **2013**, *4* (6), 2597-2604.
66. Price, H. C.; Murray, B. J.; Mattsson, J.; O'Sullivan, D.; Wilson, T. W.; Baustian, K. J.; Benning, L. G., Quantifying water diffusion in high-viscosity and glassy aqueous solutions using a Raman isotope tracer method. *Atmos. Chem. Phys.* **2014**, *14* (8), 3817-3830.
67. Song, M.; Liu, P.; Hanna, S.; Martin, S.; Bertram, A., Relative humidity-dependent viscosities of isoprene-derived secondary organic material and atmospheric implications for isoprene-dominant forests. *Atmospheric Chemistry and Physics Discussions* **2015**, *15* (1), 1131-1169.
68. Wang, B.; O'Brien, R. E.; Kelly, S. T.; Shilling, J. E.; Moffet, R. C.; Gilles, M. K.; Laskin, A., Reactivity of Liquid and Semisolid Secondary Organic Carbon with Chloride and Nitrate in Atmospheric Aerosols. *The Journal of Physical Chemistry A* **2015**, *119* (19), 4498-4508.

69. Bateman, A. P.; Belassein, H.; Martin, S. T., Impactor Apparatus for the Study of Particle Rebound: Relative Humidity and Capillary Forces. *Aerosol Science and Technology* **2013**, *48* (1), 42-52.
70. Song, M.; Liu, P. F.; Hanna, S. J.; Zaveri, R. A.; Potter, K.; You, Y.; Martin, S. T.; Bertram, A. K., Relative humidity-dependent viscosity of secondary organic material from toluene photo-oxidation and possible implications for organic particulate matter over megacities. *Atmos. Chem. Phys.* **2016**, *16* (14), 8817-8830.
71. Grayson, J. W.; Zhang, Y.; Mutzel, A.; Renbaum-Wolff, L.; Böge, O.; Kamal, S.; Herrmann, H.; Martin, S. T.; Bertram, A. K., Effect of varying experimental conditions on the viscosity of α -pinene derived secondary organic material. *Atmos. Chem. Phys.* **2016**, *16* (10), 6027-6040.
72. Pajunoja, A.; Hu, W.; Leong, Y. J.; Taylor, N. F.; Miettinen, P.; Palm, B. B.; Mikkonen, S.; Collins, D. R.; Jimenez, J. L.; Virtanen, A., Phase state of ambient aerosol linked with water uptake and chemical aging in the southeastern US. *Atmos. Chem. Phys.* **2016**, *16* (17), 11163-11176.
73. Zaveri, R. A.; Easter, R. C.; Shilling, J. E.; Seinfeld, J. H., Modeling kinetic partitioning of secondary organic aerosol and size distribution dynamics: representing effects of volatility, phase state, and particle-phase reaction. *Atmos. Chem. Phys. Discuss.* **2013**, *13* (11), 28631-28694.
74. Vaden, T. D.; Imre, D.; Beránek, J.; Shrivastava, M.; Zelenyuk, A., Evaporation kinetics and phase of laboratory and ambient secondary organic aerosol. *Proceedings of the National Academy of Sciences* **2011**, *108* (6), 2190-2195.
75. Shiraiwa, M.; Zuend, A.; Bertram, A. K.; Seinfeld, J. H., Gas-particle partitioning of atmospheric aerosols: interplay of physical state, non-ideal mixing and morphology. *Physical Chemistry Chemical Physics* **2013**, *15* (27), 11441-11453.
76. Riipinen, I.; Pierce, J. R.; Yli-Juuti, T.; Nieminen, T.; Häkkinen, S.; Ehn, M.; Junninen, H.; Lehtipalo, K.; Petäjä, T.; Slowik, J.; Chang, R.; Shantz, N. C.; Abbatt, J.; Leitch, W. R.; Kerminen, V. M.; Worsnop, D. R.; Pandis, S. N.; Donahue, N. M.; Kulmala, M., Organic condensation: a vital link connecting aerosol formation to cloud condensation nuclei (CCN) concentrations. *Atmos. Chem. Phys.* **2011**, *11* (8), 3865-3878.
77. Shiraiwa, M.; Ammann, M.; Koop, T.; Pöschl, U., Gas uptake and chemical aging of semisolid organic aerosol particles. *Proceedings of the National Academy of Sciences* **2011**, *108* (27), 11003-11008.
78. Price, H. C.; Mattsson, J.; Zhang, Y.; Bertram, A. K.; Davies, J. F.; Grayson, J. W.; Martin, S. T.; O'Sullivan, D.; Reid, J. P.; Rickards, A. M. J.; Murray, B. J., Water diffusion in atmospherically relevant α -pinene secondary organic material. *Chemical Science* **2015**, *6* (8), 4876-4883.

79. Zelenyuk, A.; Imre, D.; Beránek, J.; Abramson, E.; Wilson, J.; Shrivastava, M., Synergy between Secondary Organic Aerosols and Long-Range Transport of Polycyclic Aromatic Hydrocarbons. *Environmental Science & Technology* **2012**, *46* (22), 12459-12466.
80. Hearn, J. D.; Smith, G. D., Measuring rates of reaction in supercooled organic particles with implications for atmospheric aerosol. *Phys. Chem. Chem. Phys.* **2005**, *7* (13), 2549-2551.
81. Knopf, D. A.; Anthony, L. M.; Bertram, A. K., Reactive Uptake of O₃ by Multicomponent and Multiphase Mixtures Containing Oleic Acid. *The Journal of Physical Chemistry A* **2005**, *109* (25), 5579-5589.
82. Kuwata, M.; Martin, S. T., Phase of atmospheric secondary organic material affects its reactivity. *Proceedings of the National Academy of Sciences* **2012**, *109* (43), 17354-17359.
83. Zhou, S.; Shiraiwa, M.; McWhinney, R. D.; Poschl, U.; Abbatt, J. P. D., Kinetic limitations in gas-particle reactions arising from slow diffusion in secondary organic aerosol. *Faraday Discussions* **2013**, *165* (0), 391-406.
84. Fairhurst, M. C.; Ezell, M. J.; Kidd, C.; Lakey, P. S. J.; Shiraiwa, M.; Finlayson-Pitts, B. J., Kinetics, mechanisms and ionic liquids in the uptake of n-butylamine onto low molecular weight dicarboxylic acids. *Physical Chemistry Chemical Physics* **2017**, *19* (6), 4827-4839.
85. Ye, Q.; Robinson, E. S.; Ding, X.; Ye, P.; Sullivan, R. C.; Donahue, N. M., Mixing of secondary organic aerosols versus relative humidity. *Proceedings of the National Academy of Sciences* **2016**, *113* (45), 12649-12654.
86. Lignell, H.; Hinks, M. L.; Nizkorodov, S. A., Exploring matrix effects on photochemistry of organic aerosols. *Proceedings of the National Academy of Sciences* **2014**, 13780–13785.
87. Angell, C. A., Formation of Glasses from Liquids and Biopolymers. *Science* **1995**, *267* (5206), 1924-1935.
88. Rothfuss, N. E.; Petters, M. D., Influence of Functional Groups on the Viscosity of Organic Aerosol. *Environmental Science & Technology* **2017**, *51* (1), 271-279.
89. Song, M.; Liu, P. F.; Hanna, S. J.; Zaveri, R. A.; Potter, K.; You, Y.; Martin, S. T.; Bertram, A. K., Relative humidity-dependent viscosity of secondary organic material from toluene photo-oxidation and possible implications for organic particulate matter over megacities. *Atmospheric Chemistry and Physics* **2016**, *16* (14), 8817-8830.
90. Finlayson-Pitts, B. J.; Pitts Jr, J. N., Chapter 6 - Rates and Mechanisms of Gas-Phase Reactions in Irradiated Organic –NO_x–Air Mixtures. In *Chemistry of the Upper and Lower Atmosphere*, Academic Press: San Diego, 2000; pp 179-263.
91. Ervens, B.; Turpin, B. J.; Weber, R. J., Secondary organic aerosol formation in cloud droplets and aqueous particles (aqSOA): a review of laboratory, field and model studies. *Atmos. Chem. Phys.* **2011**, *11* (21), 11069-11102.

92. Jang, M.; Czoschke, N. M.; Lee, S.; Kamens, R. M., Heterogeneous Atmospheric Aerosol Production by Acid-Catalyzed Particle-Phase Reactions. *Science* **2002**, 298 (5594), 814-817.
93. Bateman, A. P.; Nizkorodov, S. A.; Laskin, J.; Laskin, A., Photolytic processing of secondary organic aerosols dissolved in cloud droplets. *Physical Chemistry Chemical Physics* **2011**, 13 (26), 12199-12212.
94. Nguyen, T. B.; Laskin, A.; Laskin, J.; Nizkorodov, S. A., Direct aqueous photochemistry of isoprene high-NO_x secondary organic aerosol. *Physical Chemistry Chemical Physics* **2012**, 14 (27), 9702-9714.
95. Schlesinger, W. H.; Hartley, A. E., A global budget for atmospheric NH₃. *Biogeochemistry* **1992**, 15 (3), 191-211.
96. Dentener, F. J.; Crutzen, P. J., A three-dimensional model of the global ammonia cycle. *Journal of Atmospheric Chemistry* **1994**, 19 (4), 331-369.
97. Bouwman, A. F.; Lee, D. S.; Asman, W. A. H.; Dentener, F. J.; Van Der Hoek, K. W.; Olivier, J. G. J., A global high-resolution emission inventory for ammonia. *Global Biogeochemical Cycles* **1997**, 11 (4), 561-587.
98. Nowak, J. B.; Neuman, J. A.; Bahreini, R.; Middlebrook, A. M.; Holloway, J. S.; McKeen, S. A.; Parrish, D. D.; Ryerson, T. B.; Trainer, M., Ammonia sources in the California South Coast Air Basin and their impact on ammonium nitrate formation. *Geophysical Research Letters* **2012**, 39 (7), L07804.
99. Kim, E.; Turkiewicz, K.; Zulawnick, S. A.; Magliano, K. L., Sources of fine particles in the South Coast area, California. *Atmospheric Environment* **2010**, 44 (26), 3095-3100.
100. Chow, J. C.; Watson, J. G.; Fujita, E. M.; Lu, Z.; Lawson, D. R.; Ashbaugh, L. L., Temporal and spatial variations of PM_{2.5} and PM₁₀ aerosol in the Southern California air quality study. *Atmospheric Environment* **1994**, 28 (12), 2061-2080.
101. Bones, D. L.; Henricksen, D. K.; Mang, S. A.; Gonsior, M.; Bateman, A. P.; Nguyen, T. B.; Cooper, W. J.; Nizkorodov, S. A., Appearance of strong absorbers and fluorophores in limonene-O₃ secondary organic aerosol due to NH₄⁺-mediated chemical aging over long time scales. *Journal of Geophysical Research: Atmospheres* **2010**, 115 (D5), D05203.
102. Laskin, J.; Laskin, A.; Roach, P. J.; Slysz, G. W.; Anderson, G. A.; Nizkorodov, S. A.; Bones, D. L.; Nguyen, L. Q., High-Resolution Desorption Electrospray Ionization Mass Spectrometry for Chemical Characterization of Organic Aerosols. *Analytical Chemistry* **2010**, 82 (5), 2048-2058.
103. Nguyen, T. B.; Lee, P. B.; Updyke, K. M.; Bones, D. L.; Laskin, J.; Laskin, A.; Nizkorodov, S. A., Formation of nitrogen- and sulfur-containing light-absorbing compounds accelerated by evaporation of water from secondary organic aerosols. *Journal of Geophysical Research: Atmospheres* **2012**, 117 (D1), D01207.

104. Updyke, K. M.; Nguyen, T. B.; Nizkorodov, S. A., Formation of brown carbon via reactions of ammonia with secondary organic aerosols from biogenic and anthropogenic precursors. *Atmospheric Environment* **2012**, *63* (0), 22-31.
105. Laskin, J.; Laskin, A.; Nizkorodov, S. A.; Roach, P.; Eckert, P.; Gilles, M. K.; Wang, B.; Lee, H. J.; Hu, Q., Molecular Selectivity of Brown Carbon Chromophores. *Environmental Science & Technology* **2014**, *48* (20), 12047-12055.
106. Laskin, A.; Laskin, J.; Nizkorodov, S. A., Chemistry of Atmospheric Brown Carbon. *Chemical Reviews* **2015**, *115* (10), 4335–4382.
107. Liu, Y.; Liggió, J.; Staebler, R.; Li, S. M., Reactive uptake of ammonia to secondary organic aerosols: kinetics of organonitrogen formation. *Atmos. Chem. Phys.* **2015**, *15* (23), 13569-13584.
108. Liu, T.; Wang, X.; Deng, W.; Zhang, Y.; Chu, B.; Ding, X.; Hu, Q.; He, H.; Hao, J., Role of ammonia in forming secondary aerosols from gasoline vehicle exhaust. *Science China Chemistry* **2015**, *58* (9), 1377-1384.
109. Bruinsma, J., *World Agriculture: Towards 2015/2030 : an FAO Perspective*. Earthscan: 2003.
110. Zhang, G.; Strøm, J. S.; Li, B.; Rom, H. B.; Morsing, S.; Dahl, P.; Wang, C., Emission of Ammonia and Other Contaminant Gases from Naturally Ventilated Dairy Cattle Buildings. *Biosystems Engineering* **2005**, *92* (3), 355-364.
111. Bleizgys, R.; Bagdonienė, I.; Baležentienė, L., Reduction of the Livestock Ammonia Emission under the Changing Temperature during the Initial Manure Nitrogen Biomineralization. *The Scientific World Journal* **2013**, *2013*, 825437.
112. Pereira, J.; Misselbrook, T. H.; Chadwick, D. R.; Coutinho, J.; Trindade, H., Effects of temperature and dairy cattle excreta characteristics on potential ammonia and greenhouse gas emissions from housing: A laboratory study. *Biosystems Engineering* **2012**, *112* (2), 138-150.
113. Skjøth, C. A.; Geels, C., The effect of climate and climate change on ammonia emissions in Europe. *Atmos. Chem. Phys.* **2013**, *13* (1), 117-128.
114. Constable, J. V. H.; Guenther, A. B.; Schimel, D. S.; Monson, R. K., Modelling changes in VOC emission in response to climate change in the continental United States. *Global Change Biology* **1999**, *5* (7), 791-806.
115. Pathak, R. K.; Presto, A. A.; Lane, T. E.; Stanier, C. O.; Donahue, N. M.; Pandis, S. N., Ozonolysis of α -pinene: parameterization of secondary organic aerosol mass fraction. *Atmos. Chem. Phys.* **2007**, *7* (14), 3811-3821.
116. Wainman, T.; Zhang, J.; Weschler, C. J.; Liroy, P. J., Ozone and limonene in indoor air: a source of submicron particle exposure. *Environ Health Perspect* **2000**, *108* (12), 1139-1145.

117. Shea, P. J.; Weber, J. B.; Overcash, M. R., Biological activities of 2,4-dinitrophenol in plant-soil systems. In *Residue Reviews*, Gunther, F.; Gunther, J., Eds. Springer New York: 1983; Vol. 87, pp 1-41.
118. Sanagi, M. M.; Miskam, M.; Wan Ibrahim, W. A.; Hermawan, D.; Aboul-Enein, H. Y., Determination of partition coefficient and analysis of nitrophenols by three-phase liquid-phase microextraction coupled with capillary electrophoresis. *Journal of Separation Science* **2010**, *33* (14), 2131-2139.
119. Albinet, A.; Minero, C.; Vione, D., Phototransformation processes of 2,4-dinitrophenol, relevant to atmospheric water droplets. *Chemosphere* **2010**, *80* (7), 753-758.
120. Harrison, M. A. J.; Barra, S.; Borghesi, D.; Vione, D.; Arsene, C.; Iulian Olariu, R., Nitrated phenols in the atmosphere: a review. *Atmospheric Environment* **2005**, *39* (2), 231-248.
121. Takezaki, M.; Hirota, N.; Terazima, M., Nonradiative Relaxation Processes and Electronically Excited States of Nitrobenzene Studied by Picosecond Time-Resolved Transient Grating Method. *The Journal of Physical Chemistry A* **1997**, *101* (19), 3443-3448.
122. Nguyen, T. B.; Laskin, A.; Laskin, J.; Nizkorodov, S. A., Brown carbon formation from ketoaldehydes of biogenic monoterpenes. *Faraday Discuss.* **2013**, *165*, 473-494.
123. Grayson, J. W.; Song, M.; Sellier, M.; Bertram, A. K., Validation of the poke-flow technique combined with simulations of fluid flow for determining viscosities in samples with small volumes and high viscosities. *Atmos. Meas. Tech. Discuss.* **2015**, *8* (1), 877-903.
124. Schnell, E., Slippage of Water over Nonwetable Surfaces. *Journal of Applied Physics* **1956**, *27* (10), 1149-1152.
125. Churaev, N. V.; Sobolev, V. D.; Somov, A. N., Slippage of liquids over lyophobic solid surfaces. *Journal of Colloid and Interface Science* **1984**, *97* (2), 574-581.
126. Watanabe, K.; Udagawa, H., Drag reduction of non-newtonian fluids in a circular pipe with a highly water-repellent wall. *AIChE Journal* **2001**, *47* (2), 256-262.
127. Baudry, J.; Charlaix, E.; Tonck, A.; Mazuyer, D., Experimental Evidence for a Large Slip Effect at a Nonwetting Fluid–Solid Interface. *Langmuir* **2001**, *17* (17), 5232-5236.
128. Craig, V. S. J.; Neto, C.; Williams, D. R. M., Shear-Dependent Boundary Slip in an Aqueous Newtonian Liquid. *Physical Review Letters* **2001**, *87* (5), 054504.
129. Tretheway, D. C.; Meinhart, C. D., Apparent fluid slip at hydrophobic microchannel walls. *Physics of Fluids (1994-present)* **2002**, *14* (3), L9-L12.
130. Cheng, J. T.; Giordano, N., Fluid flow through nanometer-scale channels. *Physical Review E* **2002**, *65* (3), 031206.

131. Jin, S.; Huang, P.; Park, J.; Yoo, J. Y.; Breuer, K. S., Near-surface velocimetry using evanescent wave illumination. *Exp Fluids* **2004**, *37* (6), 825-833.
132. Joseph, P.; Tabeling, P., Direct measurement of the apparent slip length. *Physical Review E* **2005**, *71* (3), 035303.
133. Chiara, N.; Drew, R. E.; Elmar, B.; Hans-Jürgen, B.; Vincent, S. J. C., Boundary slip in Newtonian liquids: a review of experimental studies. *Reports on Progress in Physics* **2005**, *68* (12), 2859.
134. Choi, C.-H.; Kim, C.-J., Large Slip of Aqueous Liquid Flow over a Nanoengineered Superhydrophobic Surface. *Physical Review Letters* **2006**, *96* (6), 066001.
135. Joly, L.; Ybert, C.; Bocquet, L., Probing the Nanohydrodynamics at Liquid-Solid Interfaces Using Thermal Motion. *Physical Review Letters* **2006**, *96* (4), 046101.
136. Zhu, L.; Neto, C.; Attard, P., Reliable Measurements of Interfacial Slip by Colloid Probe Atomic Force Microscopy. III. Shear-Rate-Dependent Slip. *Langmuir* **2012**, *28* (7), 3465-3473.
137. Li, L.; Mo, J.; Li, Z., Flow and slip transition in nanochannels. *Physical Review E* **2014**, *90* (3), 033003.
138. Tuckermann, R.; Cammenga, H. K., The surface tension of aqueous solutions of some atmospheric water-soluble organic compounds. *Atmos. Environ.* **2004**, *38* (36), 6135-6138.
139. Engelhart, G. J.; Asa-Awuku, A.; Nenes, A.; Pandis, S. N., CCN activity and droplet growth kinetics of fresh and aged monoterpene secondary organic aerosol. *Atmos. Chem. Phys.* **2008**, *8* (14), 3937-3949.
140. Chen, X.; Hopke, P. K., Secondary organic aerosol from α -pinene ozonolysis in dynamic chamber system. *Indoor Air* **2009**, *19* (4), 335-345.
141. Kostenidou, E.; Pathak, R. K.; Pandis, S. N., An Algorithm for the Calculation of Secondary Organic Aerosol Density Combining AMS and SMPS Data. *Aerosol Sci. Technol.* **2007**, *41* (11), 1002-1010.
142. Forrister, H.; Liu, J.; Scheuer, E.; Dibb, J.; Ziemba, L.; Thornhill, K. L.; Anderson, B.; Diskin, G.; Perring, A. E.; Schwarz, J. P.; Campuzano-Jost, P.; Day, D. A.; Palm, B. B.; Jimenez, J. L.; Nenes, A.; Weber, R. J., Evolution of brown carbon in wildfire plumes. *Geophysical Research Letters* **2015**, *42* (11), 4623-4630.
143. Pankow, J. F., Gas/particle partitioning of neutral and ionizing compounds to single and multi-phase aerosol particles. 1. Unified modeling framework. *Atmospheric Environment* **2003**, *37* (24), 3323-3333.
144. Petters, M. D.; Kreidenweis, S. M.; Snider, J. R.; Koehler, K. A.; Wang, Q.; Prenni, A. J.; Demott, P. J., Cloud droplet activation of polymerized organic aerosol. *Tellus B* **2006**, *58* (3), 196-205.

145. Liu, S.; Shilling, J. E.; Song, C.; Hiranuma, N.; Zaveri, R. A.; Russell, L. M., Hydrolysis of Organonitrate Functional Groups in Aerosol Particles. *Aerosol Science and Technology* **2012**, *46* (12), 1359-1369.
146. Tong, H. J.; Reid, J. P.; Bones, D. L.; Luo, B. P.; Krieger, U. K., Measurements of the timescales for the mass transfer of water in glassy aerosol at low relative humidity and ambient temperature. *Atmos. Chem. Phys.* **2011**, *11* (10), 4739-4754.
147. Burnett, D. J.; Thielmann, F.; Booth, J., Determining the critical relative humidity for moisture-induced phase transitions. *International Journal of Pharmaceutics* **2004**, *287* (1–2), 123-133.
148. Zobrist, B.; Soonsin, V.; Luo, B. P.; Krieger, U. K.; Marcolli, C.; Peter, T.; Koop, T., Ultra-slow water diffusion in aqueous sucrose glasses. *Phys. Chem. Chem. Phys.* **2011**, *13* (8), 3514-3526.
149. Garcia-Garibay, M. A.; Campos, L. M., Photochemical decarbonylation of ketones: recent advances and reactions in crystalline solids. *ChemInform* **2004**, *35* (19).
150. Lambe, A. T.; Chhabra, P. S.; Onasch, T. B.; Brune, W. H.; Hunter, J. F.; Kroll, J. H.; Cummings, M. J.; Brogan, J. F.; Parmar, Y.; Worsnop, D. R.; Kolb, C. E.; Davidovits, P., Effect of oxidant concentration, exposure time, and seed particles on secondary organic aerosol chemical composition and yield. *Atmos. Chem. Phys.* **2015**, *15* (6), 3063-3075.
151. Lambe, A. T.; Ahern, A. T.; Williams, L. R.; Slowik, J. G.; Wong, J. P. S.; Abbatt, J. P. D.; Brune, W. H.; Ng, N. L.; Wright, J. P.; Croasdale, D. R.; Worsnop, D. R.; Davidovits, P.; Onasch, T. B., Characterization of aerosol photooxidation flow reactors: heterogeneous oxidation, secondary organic aerosol formation and cloud condensation nuclei activity measurements. *Atmos. Meas. Tech.* **2011**, *4* (3), 445-461.
152. Ng, N. L.; Canagaratna, M. R.; Zhang, Q.; Jimenez, J. L.; Tian, J.; Ulbrich, I. M.; Kroll, J. H.; Docherty, K. S.; Chhabra, P. S.; Bahreini, R.; Murphy, S. M.; Seinfeld, J. H.; Hildebrandt, L.; Donahue, N. M.; DeCarlo, P. F.; Lanz, V. A.; Prévôt, A. S. H.; Dinar, E.; Rudich, Y.; Worsnop, D. R., Organic aerosol components observed in Northern Hemispheric datasets from Aerosol Mass Spectrometry. *Atmos. Chem. Phys.* **2010**, *10* (10), 4625-4641.
153. Ng, N. L.; Canagaratna, M. R.; Jimenez, J. L.; Chhabra, P. S.; Seinfeld, J. H.; Worsnop, D. R., Changes in organic aerosol composition with aging inferred from aerosol mass spectra. *Atmos. Chem. Phys.* **2011**, *11* (13), 6465-6474.
154. Lambe, A. T.; Onasch, T. B.; Croasdale, D. R.; Wright, J. P.; Martin, A. T.; Franklin, J. P.; Massoli, P.; Kroll, J. H.; Canagaratna, M. R.; Brune, W. H.; Worsnop, D. R.; Davidovits, P., Transitions from Functionalization to Fragmentation Reactions of Laboratory Secondary Organic Aerosol (SOA) Generated from the OH Oxidation of Alkane Precursors. *Environmental Science & Technology* **2012**, *46* (10), 5430-5437.

155. Chao, W.; Hsieh, J.-T.; Chang, C.-H.; Lin, J. J.-M., Direct kinetic measurement of the reaction of the simplest Criegee intermediate with water vapor. *Science* **2015**, *347* (6223), 751-754.
156. Shiraiwa, M.; Seinfeld, J. H., Equilibration timescale of atmospheric secondary organic aerosol partitioning. *Geophysical Research Letters* **2012**, *39* (24), L24801.
157. Yu, K.-P.; Lin, C.-C.; Yang, S.-C.; Zhao, P., Enhancement effect of relative humidity on the formation and regional respiratory deposition of secondary organic aerosol. *Journal of Hazardous Materials* **2011**, *191* (1–3), 94-102.
158. Saathoff, H.; Naumann, K. H.; Möhler, O.; Jonsson, Å. M.; Hallquist, M.; Kiendler-Scharr, A.; Mentel, T. F.; Tillmann, R.; Schurath, U., Temperature dependence of yields of secondary organic aerosols from the ozonolysis of α -pinene and limonene. *Atmos. Chem. Phys.* **2009**, *9* (5), 1551-1577.
159. Jonsson, Å. M.; Hallquist, M.; Ljungström, E., Impact of Humidity on the Ozone Initiated Oxidation of Limonene, Δ^3 -Carene, and α -Pinene. *Environmental Science & Technology* **2006**, *40* (1), 188-194.
160. Jonsson, Å. M.; Hallquist, M.; Ljungström, E., Influence of OH Scavenger on the Water Effect on Secondary Organic Aerosol Formation from Ozonolysis of Limonene, Δ^3 -Carene, and α -Pinene. *Environmental Science & Technology* **2008**, *42* (16), 5938-5944.
161. Czoschke, N. M.; Jang, M., Acidity effects on the formation of α -pinene ozone SOA in the presence of inorganic seed. *Atmospheric Environment* **2006**, *40* (23), 4370-4380.
162. Czoschke, N. M.; Jang, M.; Kamens, R. M., Effect of acidic seed on biogenic secondary organic aerosol growth. *Atmospheric Environment* **2003**, *37* (30), 4287-4299.
163. Chu, B.; Liu, Y.; Li, J.; Takekawa, H.; Liggió, J.; Li, S.-M.; Jiang, J.; Hao, J.; He, H., Decreasing effect and mechanism of FeSO₄ seed particles on secondary organic aerosol in α -pinene photooxidation. *Environmental Pollution* **2014**, *193*, 88-93.
164. Cocker III, D. R.; Clegg, S. L.; Flagan, R. C.; Seinfeld, J. H., The effect of water on gas-particle partitioning of secondary organic aerosol. Part I: α -pinene/ozone system. *Atmospheric Environment* **2001**, *35* (35), 6049-6072.
165. Kristensen, K.; Cui, T.; Zhang, H.; Gold, A.; Glasius, M.; Surratt, J. D., Dimers in α -pinene secondary organic aerosol: effect of hydroxyl radical, ozone, relative humidity and aerosol acidity. *Atmos. Chem. Phys.* **2014**, *14* (8), 4201-4218.
166. Bonn, B.; Schuster, G.; Moortgat, G. K., Influence of Water Vapor on the Process of New Particle Formation during Monoterpene Ozonolysis. *The Journal of Physical Chemistry A* **2002**, *106* (12), 2869-2881.
167. Emanuelsson, E. U.; Watne, Å. K.; Lutz, A.; Ljungström, E.; Hallquist, M., Influence of Humidity, Temperature, and Radicals on the Formation and Thermal Properties of Secondary

Organic Aerosol (SOA) from Ozonolysis of β -Pinene. *The Journal of Physical Chemistry A* **2013**, *117* (40), 10346-10358.

168. Fry, J. L.; Kiendler-Scharr, A.; Rollins, A. W.; Wooldridge, P. J.; Brown, S. S.; Fuchs, H.; Dubé, W.; Mensah, A.; dal Maso, M.; Tillmann, R.; Dorn, H. P.; Brauers, T.; Cohen, R. C., Organic nitrate and secondary organic aerosol yield from NO₃ oxidation of β -pinene evaluated using a gas-phase kinetics/aerosol partitioning model. *Atmos. Chem. Phys.* **2009**, *9* (4), 1431-1449.

169. Boyd, C. M.; Sanchez, J.; Xu, L.; Eugene, A. J.; Nah, T.; Tuet, W. Y.; Guzman, M. I.; Ng, N. L., Secondary organic aerosol formation from the β -pinene+NO₃ system: effect of humidity and peroxy radical fate. *Atmos. Chem. Phys.* **2015**, *15* (13), 7497-7522.

170. Riva, M.; Budisulistiorini, S. H.; Chen, Y.; Zhang, Z.; D'Ambro, E. L.; Zhang, X.; Gold, A.; Turpin, B. J.; Thornton, J. A.; Canagaratna, M. R.; Surratt, J. D., Chemical Characterization of Secondary Organic Aerosol from Oxidation of Isoprene Hydroxyhydroperoxides. *Environmental Science & Technology* **2016**, 9889–9899.

171. Zhang, H.; Surratt, J. D.; Lin, Y. H.; Bapat, J.; Kamens, R. M., Effect of relative humidity on SOA formation from isoprene/NO photooxidation: enhancement of 2-methylglyceric acid and its corresponding oligoesters under dry conditions. *Atmos. Chem. Phys.* **2011**, *11* (13), 6411-6424.

172. Dommen, J.; Metzger, A.; Duplissy, J.; Kalberer, M.; Alfarra, M. R.; Gascho, A.; Weingartner, E.; Prevot, A. S. H.; Verheggen, B.; Baltensperger, U., Laboratory observation of oligomers in the aerosol from isoprene/NO_x photooxidation. *Geophysical Research Letters* **2006**, *33* (13), L13805.

173. Nguyen, T. B.; Roach, P. J.; Laskin, J.; Laskin, A.; Nizkorodov, S. A., Effect of humidity on the composition of isoprene photooxidation secondary organic aerosol. *Atmos. Chem. Phys.* **2011**, *11* (14), 6931-6944.

174. Lewandowski, M.; Jaoui, M.; Offenberg, J. H.; Krug, J. D.; Kleindienst, T. E., Atmospheric oxidation of isoprene and 1,3-butadiene: influence of aerosol acidity and relative humidity on secondary organic aerosol. *Atmos. Chem. Phys.* **2015**, *15* (7), 3773-3783.

175. Harvey, R. M.; Bateman, A. P.; Jain, S.; Li, Y. J.; Martin, S.; Petrucci, G. A., Optical Properties of Secondary Organic Aerosol from cis-3-Hexenol and cis-3-Hexenyl Acetate: Effect of Chemical Composition, Humidity, and Phase. *Environmental Science & Technology* **2016**, *50* (10), 4997-5006.

176. Kamens, R. M.; Zhang, H.; Chen, E. H.; Zhou, Y.; Parikh, H. M.; Wilson, R. L.; Galloway, K. E.; Rosen, E. P., Secondary organic aerosol formation from toluene in an atmospheric hydrocarbon mixture: Water and particle seed effects. *Atmospheric Environment* **2011**, *45* (13), 2324-2334.

177. Cao, G.; Jang, M., An SOA Model for Toluene Oxidation in the Presence of Inorganic Aerosols. *Environmental Science & Technology* **2010**, *44* (2), 727-733.

178. Zhou, Y.; Zhang, H.; Parikh, H. M.; Chen, E. H.; Rattanavaraha, W.; Rosen, E. P.; Wang, W.; Kamens, R. M., Secondary organic aerosol formation from xylenes and mixtures of toluene and xylenes in an atmospheric urban hydrocarbon mixture: Water and particle seed effects (II). *Atmospheric Environment* **2011**, *45* (23), 3882-3890.
179. Cocker Iii, D. R.; Mader, B. T.; Kalberer, M.; Flagan, R. C.; Seinfeld, J. H., The effect of water on gas-particle partitioning of secondary organic aerosol: II. m-xylene and 1,3,5-trimethylbenzene photooxidation systems. *Atmospheric Environment* **2001**, *35* (35), 6073-6085.
180. Roach, P. J.; Laskin, J.; Laskin, A., Molecular Characterization of Organic Aerosols Using Nanospray-Desorption/Electrospray Ionization-Mass Spectrometry. *Analytical Chemistry* **2010**, *82* (19), 7979-7986.
181. Roach, P. J.; Laskin, J.; Laskin, A., Nanospray desorption electrospray ionization: an ambient method for liquid-extraction surface sampling in mass spectrometry. *Analyst* **2010**, *135* (9), 2233-2236.
182. Kind, T.; Fiehn, O., Seven Golden Rules for heuristic filtering of molecular formulas obtained by accurate mass spectrometry. *BMC Bioinformatics* **2007**, *8*, 105-105.
183. Sato, K.; Hatakeyama, S.; Imamura, T., Secondary Organic Aerosol Formation during the Photooxidation of Toluene: NO_x Dependence of Chemical Composition. *The Journal of Physical Chemistry A* **2007**, *111* (39), 9796-9808.
184. Varutbangkul, V.; Brechtel, F. J.; Bahreini, R.; Ng, N. L.; Keywood, M. D.; Kroll, J. H.; Flagan, R. C.; Seinfeld, J. H.; Lee, A.; Goldstein, A. H., Hygroscopicity of secondary organic aerosols formed by oxidation of cycloalkenes, monoterpenes, sesquiterpenes, and related compounds. *Atmos. Chem. Phys.* **2006**, *6* (9), 2367-2388.
185. Krechmer, J. E.; Pagonis, D.; Ziemann, P. J.; Jimenez, J. L., Quantification of Gas-Wall Partitioning in Teflon Environmental Chambers Using Rapid Bursts of Low-Volatility Oxidized Species Generated in Situ. *Environmental Science & Technology* **2016**, *50* (11), 5757-5765.
186. Matsunaga, A.; Ziemann ‡, P. J., Gas-Wall Partitioning of Organic Compounds in a Teflon Film Chamber and Potential Effects on Reaction Product and Aerosol Yield Measurements. *Aerosol Science and Technology* **2010**, *44* (10), 881-892.
187. Zhang, X.; Cappa, C. D.; Jathar, S. H.; McVay, R. C.; Ensberg, J. J.; Kleeman, M. J.; Seinfeld, J. H., Influence of vapor wall loss in laboratory chambers on yields of secondary organic aerosol. *Proceedings of the National Academy of Sciences* **2014**, *111* (16), 5802-5807.
188. Walser, M. L.; Desyaterik, Y.; Laskin, J.; Laskin, A.; Nizkorodov, S. A., High-resolution mass spectrometric analysis of secondary organic aerosol produced by ozonation of limonene. *Physical Chemistry Chemical Physics* **2008**, *10* (7), 1009-1022.
189. Lin, P.; Liu, J.; Shilling, J. E.; Kathmann, S.; Laskin, J.; Laskin, A., Molecular Characterization of Brown Carbon (BrC) Chromophores in Secondary Organic Aerosol Generated From Photo-Oxidation of Toluene. *Physical Chemistry Chemical Physics* **2015**, 23312-23325

190. Li, Y.; Pöschl, U.; Shiraiwa, M., Molecular corridors and parameterizations of volatility in the chemical evolution of organic aerosols. *Atmos. Chem. Phys.* **2016**, *16* (5), 3327-3344.
191. Shiraiwa, M.; Berkemeier, T.; Schilling-Fahnestock, K. A.; Seinfeld, J. H.; Pöschl, U., Molecular corridors and kinetic regimes in the multiphase chemical evolution of secondary organic aerosol. *Atmos. Chem. Phys.* **2014**, *14* (16), 8323-8341.
192. Lin, P.; Aiona, P. K.; Li, Y.; Shiraiwa, M.; Laskin, J.; Nizkorodov, S. A.; Laskin, A., Molecular Characterization of Brown Carbon in Biomass Burning Aerosol Particles. *Environmental Science & Technology* **2016**, *50* (21), 11815-11824.
193. Pankow, J. F., An absorption model of the gas/aerosol partitioning involved in the formation of secondary organic aerosol. *Atmospheric Environment* **1994**, *28* (2), 189-193.
194. Donahue, N. M.; Robinson, A. L.; Stanier, C. O.; Pandis, S. N., Coupled Partitioning, Dilution, and Chemical Aging of Semivolatile Organics. *Environmental Science & Technology* **2006**, *40* (8), 2635-2643.
195. Shiraiwa, M.; Yee, L. D.; Schilling, K. A.; Loza, C. L.; Craven, J. S.; Zuend, A.; Ziemann, P. J.; Seinfeld, J. H., Size distribution dynamics reveal particle-phase chemistry in organic aerosol formation. *Proceedings of the National Academy of Sciences* **2013**, *110* (29), 11746-11750.
196. Chan, M. N.; Nah, T.; Wilson, K. R., Real time in situ chemical characterization of sub-micron organic aerosols using Direct Analysis in Real Time mass spectrometry (DART-MS): the effect of aerosol size and volatility. *Analyst* **2013**, *138* (13), 3749-3757.
197. Kundu, S.; Fisseha, R.; Putman, A. L.; Rahn, T. A.; Mazzoleni, L. R., High molecular weight SOA formation during limonene ozonolysis: insights from ultrahigh-resolution FT-ICR mass spectrometry characterization. *Atmos. Chem. Phys.* **2012**, *12* (12), 5523-5536.